ABSTRACT

Title of Document: IMPACTS OF WINDS AND RIVER FLOW ON ESTUARINE DYNAMICS AND HYPOXIA IN CHESAPEAKE BAY

Yun Li, Doctor of Philosophy, 2012

Directed By: Professor Ming Li
Horn Point Laboratory, UMCES
Marine Estuarine Environmental Science

In the stratified rotating estuary of Chesapeake Bay, the driving mechanisms of wind-induced lateral circulation are examined using a three-dimensional hydrodynamic model (ROMS). A new approach based on the streamwise vorticity dynamics is developed, and the analysis reveals a balance among three terms: the conversion of the planetary vorticity by along-channel current shear, baroclinicity due to cross-channel density gradient, and turbulent diffusion. It is found that the lateral flow in the Bay is mainly driven by the Ekman forcing, but the lateral baroclinicity creates asymmetry in the streamwise vorticity between down- and up-estuary winds.

The traditional view of wind-driven circulation in estuaries ignores the lateral circulation, but wind-induced lateral flows can affect subtidal estuarine circulation and stratification. Coriolis acceleration associated with the lateral flows is of first-order importance in the along-channel momentum balance, with the sign opposite to the stress divergence in the surface layer and the pressure gradient in the bottom layer,

thereby reducing the shear in the along-channel current. Moreover, the lateral straining of the density field by lateral circulation offsets the along-channel straining to control the overall stratification. Regime diagrams are constructed using the dimensionless Wedderburn (W) and Kelvin (Ke) numbers to clarify the net wind effects.

A coupled hydrodynamic-biogeochemical model is developed to simulate the seasonal cycle of dissolved oxygen in Chesapeake Bay and investigate key processes which regulate summer hypoxia in the estuary. Diagnostic analysis of the oxygen budget for the bottom water reveals a balance between physical transport and biological consumption. In addition to the vertical diffusive flux, the along-channel and cross-channel advective fluxes are found to be important contributors in supplying oxygen to the bottom water. While the vertical diffusive oxygen flux varies over the spring-neap tidal cycle and is enhanced during wind events, the advective oxygen fluxes show long-term averages due to the gravitational estuarine circulation but display strong oscillations due to wind-driven circulations. It is found that water column respiration comprises about 74% of the total consumption and sediment oxygen demand contributes 26%. Sensitivity-analysis model runs are conducted to further quantify the effects of river flow, winds, water column respiration and sediment oxygen demand on the hypoxic volume in the estuary.

IMPACTS OF WINDS AND RIVER FLOW ON ESTUARINE DYNAMICS AND HYPOXIA IN CHESAPEAKE BAY

By

Yun Li

Dissertation submitted to the Faculty of the Graduate School of the
University of Maryland, College Park, in partial fulfillment
of the requirements for the degree of
Doctor of Philosophy
2012

Advisory Committee:
Professor Ming Li, Chair
Professor William C. Boicourt
Professor W. Rockwell Geyer
Professor W. Michael Kemp
Professor Michael R. Roman
Professor Kayo Ide, Dean's Representative

Dedication

To my husband Xinfeng Liang

and

my parents Zaitian Li and Yanxia Nie

Acknowledgements

I would like to thank my advisor Dr. Ming Li for his high expectation and demands during my graduate study. He does not only give me freedom for scientific pursuits, but also sharpens my ideas and keeps me on track. Meanwhile, he grants me various opportunities to prepare myself for future career, including giving presentations in conferences, collaborating with colleagues and working on peer-reviewed publications. In addition, he provides financial support and computational resources which are essential to the graduate research. I also would like to thank the excellent thesis committee, Drs. William Boicourt, Rocky Geyer, Michael Kemp and Mike Roman for their insightful guidance that leads me to the right way, for their encouragement through the challenging years, and their invaluable supports during my application to the postdoc position. I also like to thank Dr. Kayo Ide for her willingness to serve as Dean's representative during my defense.

I thank the HPLers for their hospitality. This work could never have been accomplished without assistance from a large number of people. I gained pleasure of interaction with many brilliant scientists and students. I would like to thank Larry Sanford, Elizabeth North, Liejun Zhong, Shih-Nan Chen, Jeremy Testa, Peng Cheng, Peng Jia and Younjoo Lee, who are always generous with their knowledge and time when I trapped them for questions.

I am sincerely thankful to the NOAA CHRP Project (Coastal Hypoxia Research Program). A major research project like this is never the work of anyone

alone. It provides an invaluable opportunity to collaborate with a group of people from different background. I indeed appreciate their thought-provoking discussions that broaden the width of my knowledge. All the inputs were beneficial to the study presented in Chapter 4. Also, a lot of difficulty emerged since I started to couple the ROMS-RCA model. PIs Michael Kemp, Ming Li and Dom DiTorio provided invaluable trust and patience that led me to the final solution. I thank Jeremy Testa, Younjoo Lee, Jim Fitzpatrick and Damian Brady for their help on mining the data and diagnosing technique problems.

I would like to extend my special thanks to Drs. Rocky Geyer and Parker MacCready for organizing the Coastal and Estuarine Fluid Dynamics course at Friday Harbor Labs, University of Washington. I was about to start the thesis when I joined the class in 2009. During the rich and vibrant academic activities, I learned a ton about the estuarine theories and field work. The analyses of estuarine lateral circulation in Chapter 2 and 3 are inspired by the lectures. The course was also a joyful experience as important as the scientific training. I enjoyed the good humor and friendship of all members.

Finally, I am forever indebted to my husband and my parents for their unwavering love, support and understanding for years when I pursued my ambitions and enthusiasm for science. I dedicated this volume to them.

Table of Contents

List of Tables

List of Figures

Chapter 1: Introduction

1. Typology of hypoxia

Oxygen depletion due to nutrient enrichment is a widespread phenomenon that is growing globally [e.g. *Andersen and Rydberg*, 1988; *Diaz*, 2001; *Justic et al.*, 2003; *Kemp et al.*, 2005; *Wei et al.*, 2007; *Conley et al.*, 2007; *Wilson et al.*, 2008]. Hypoxia is usually defined as dissolved oxygen (DO) concentrations falling below approximately 2 mgL^{-1} that interrupts normal metabolism of marine organisms. Two principal factors that lead to the development of hypoxia are water-column stratification, which isolates the bottom DO exchange from oxygen-rich surface water, and decomposition of organic matter in the bottom water, which reduces oxygen levels [*Diaz*, 2001].

The imbalance between the biological sinks and physical sources varies in time and space, thus producing permanent, seasonal, episodic and diel hypoxia in different estuarine and coastal regions [*Diaz and Rosenberg*, 2008; *Kemp et al.*, 2009]. Following the description of categories by *Kemp et al.* [2009], permanent hypoxia occurs in systems prone to strong persistent stratification that suppresses vertical diffusive processes: for example, large dead zones are found in Baltic Sea [*Conley et al.*, 2009] as well as in many fjords. Seasonal hypoxia is the most common form of eutrophication-induced hypoxia in stratified estuarine and shelf regions. After spring river discharge strengthens stratification, warming temperature stimulates respiration

of sinking organic matter that has been accumulated from spring blooms. Many U.S. coastal and estuarine areas suffer from the seasonal hypoxia, including Chesapeake Bay [*Officer et al.*, 1984; *Malone*, 1991; *Smith and Kemp*, 1995; *Kemp et al.*, 2005] and West Long Island Sound [*Welsh and Eller*, 1991; *Parker and O'Reilly*, 1991; *Wilson et al.*, 2008; *O'Donnell et al.*, 2008]. Episodic hypoxia tends to occur at irregular intervals associated with meteorological forcing. It can be driven by wind-induced upwelling of nutrient-rich and oxygen-poor water onto productive continental shelves [*Chan et al.*, 2008] or produced by major storm events that deliver large pulses of organic loading [*Peierls et al.*, 2003]. Diel hypoxia is usually confined to shallow productive systems in which primary production in daylight hours produces oxygen supersaturation whereas heterotrophic respiration at night leads to temporary hypoxia [*Verity et al*., 2006; *Shen et al.*, 2008; *Tyler et al.*, 2009].

2. Impact of climatic variability on hypoxia

Historically, the hypoxia research has focused on eutrophication effects [e.g. *Rosenburg*, 1990; *Johannessen and Dahl*, 1996; *Justic et al.*, 2002; *Kemp et al.*, 2005]. It is widely believed that anthropogenic nutrient enrichment fuels algal production and causes oxygen depletion from bottom waters. Despite major public commitments to reduce nutrient loading, however, many estuaries and coastal oceans continue to experience hypoxia and deteriorating water quality. A major impediment to developing successful restoration strategy is the complicating effect of climate variability. Large inter-annual fluctuations in river flow result in highly variable

nutrient loading and estuarine circulation. In addition, episodic wind events and longer-term changes in wind regimes exert more subtle and poorly-understood controls on key biogeochemical processes.

The climate can influence hypoxia through many mechanisms, including changes in river flow and nutrient delivery, vertical stratification, particle sinking, turbidity, water residence time, gas solubility and respiration [e.g., *Cloern et al.*, 1983; *Harding et al.*, 1986; *Townsend and Cammen*, 1988; *Lehman*, 1992; *Keller et al.*, 1999; *Howarth et al.*, 2000; *Borsuk et al.*, 2004]. In a stimulating and provocative paper, *Scully* [2010a] suggested that the increase of hypoxic volume in Chesapeake Bay over the past few decades is caused by the climatic shift of summer prevailing wind conditions from the southerly to westerly. In the western Long Island Sound, *Wilson et al.* [2008] found that the directionality of summertime wind controls the ventilation of bottom waters and could explain the difference between the hypoxic and normoxic years. In coastal waters around Denmark, unfavorable meteorological conditions drove severe hypoxia in recent years even though the nutrient loads had significantly decreased [*Conley et al.*, 2007].

3. Estuarine physical processes affecting hypoxia

In order to predict how climatic variability affects estuarine hypoxia, knowledge on how climate variability affects estuarine physical processes is needed. Recent research suggests that summer winds and interannual variability of river discharge are

two important factors which influence the summer hypoxia, and the efforts are focused on investigation of these two topics on estuarine physics.

Much of the recent advance in estuarine physics has come from new understanding of estuarine dynamics at tidal scale times, such as the flood-ebb and spring-neap cycles of mixing and stratification [*Simpson et al.*, 1990; *Geyer et al.*, 2000, *MacCready and Geyer*, 2010]. Relatively little is understood of the estuarine-circulation variability at interannual and decadal time scales. To provide a theoretical framework for the discussion of climate impacts on estuaries, predictions based on the classic steady-state theory of *Hansen and Rattray* [1965] and *Chatwin* [1976] are useful. Building on these studies and assume constant vertical mixing rate, *Hetland and Geyer* [2004] showed that the estuarine residual velocity and the salinity stratification can be scaled to river flow Q as

$$u_E \propto Q^{1/3} \tag{1}$$

$$\frac{\partial S}{\partial z} \propto Q^{2/3} \tag{2}$$

We expect climate variability to bring changes in river flow and therefore to fundamentally alter estuarine physical characteristics. The theory suggests that the both estuarine flow and salinity stratification increase with increasing river runoff. It also suggests that estuarine flow and salt fields respond very differently. While the estuarine circulation shows a stiffening response to river flow, the stratification is

relatively sensitive. Apart from this simple scaling theory and limited observational evidence for the power dependence on river discharge [*Ralston et al.*, 2008; *Lerzack et al.*, 2009], we have very little knowledge of the effects of climate variability/change on estuarine circulation and salinity distributions.

Similarly, little attention has been paid to the role of wind in forcing estuarine circulation and mixing, despite longstanding predictions of first-order effects [*Rattray and Hansen*, 1962] and observational evidence of strong wind-driven circulations [e.g. *Wang*, 1979a, b; *Wong and Valle-Levinson*, 2002]. In several studies, winds have been shown to be a dominant mixing agency in estuaries [*Goodrich et al.*, 1987; *Li et al.*, 2007]. Recent research has suggested that winds can asymmetrically modify estuarine stratification and salt fluxes. *Scully et al.* [2005] proposed a wind straining mechanism: down-estuary wind strains the along-channel density gradient to increase stratification whereas up-estuary wind reduces the vertical shear and stratification. *Chen and Sanford* [2009] examined the competition between wind mixing and wind straining in an idealized numerical model and constructed a regime diagram to classify the wind's role in affecting estuarine stratification.

However, these studies ignore important lateral circulations that can be generated by winds. A simple scaling suggests that wider estuaries are expected to have a stronger lateral response to the along-channel wind forcing because of rotation. Several studies have shown that along-channel winds can drive strong lateral Ekman flows and isopycnal movements, generating upwelling/downwelling at shallow shoals

[*Malone et al.*, 1986; *Sanford et al.*, 1990; *Wilson et al.*, 2008; *Scully*, 2010b]. These lateral motions are fundamental to estuarine dynamics because they transport momentum [*Lerczak and Geyer*, 2004; *Scully et al.*, 2009], alter stratification [*Lacy et al.*, 2003; *Li and Li*, 2011] and transport sediment [*Geyer et al.*, 2001; *Chen et al.*, 2009]. Furthermore, the lateral circulations provide an exchange pathway for biologically important materials such as nutrients and oxygen, especially through lateral upwelling and downwelling [*Malone et al.*, 1986; *Sanford et al.*, 1990; *Reynolds-Fleming and Luettich*, 2004]. A recent study suggests that, in Chesapeake Bay, the wind-driven lateral exchange of oxygen between shoal regions and deeper hypoxic areas is more important than direct turbulent mixing through the pycnocline [*Scully*, 2010b].

There have been a series of interesting studies on the dynamics of lateral circulations in tidally driven estuaries, while the dynamics of wind-driven lateral circulations in stratified estuaries of varying width are still not satisfactorily understood. Several mechanisms have been proposed, including differential advection [*Nunes and Simpson*, 1985; *Lerczak and Geyer*, 2004], bottom Ekman layer [*Scully et al.*, 2009], diffusive boundary layer on a slope [*Chen et al.*, 2009], channel curvature [*Chant*, 2002] and lateral salinity gradient resulting from the presence of stratification [*Lerczak and Geyer*, 2004; *Scully et al.*, 2009; *Cheng et al.*, 2009].

The interaction between one mechanism and another can cause asymmetric response of lateral circulation based on wind directions. For example, in a stratified

rotating estuary, due to the Coriolis force, isopycnals are tilted downwards on the left side of the estuarine channel in the absence of winds (looking into estuary). During down-/up-estuary winds events, the Ekman transport drives a counterclockwise/clockwise lateral circulation and steepens/flattens the isopycnals in the cross-channel sections. In analogy to the flood-ebb asymmetry found by *Lerczak and Geyer* [2004] and *Scully et al*. [2009], the existence of lateral salinity gradient can interrupt Ekman dynamics to generate asymmetry in the strength of the lateral circulations between down- and up-estuary winds.

The wind-induced lateral circulation can affect the stratification and along-channel momentum balance, however, neither effect has been adequately quantified. The lateral circulations acting on the lateral density gradient yield lateral straining, so that the net effect of wind on the estuarine stratification depends on both lateral and longitudinal straining processes. In addition, Coriolis force or nonlinear advection associated with the wind-induced lateral circulation provides an additional driving term for along-channel exchange flow [e.g. *Lerczak and Geyer*, 2004; *Winant*, 2004]. In narrow estuaries, *Lerczak and Geyer* [2004] and *Scully et al.* [2009] demonstrated that the nonlinear advection by lateral flows amplifies estuarine residual circulation, but it is unclear for wide estuaries because nonlinear advection is expected to be weaker.

4. Hypoxia in Chesapeake Bay

Chesapeake Bay is about 300 km long and 5~20 km wide, with a relatively deep and narrow central channel continuous over much of its length and flanked by broad shallow shoals (Chapter 4, Fig. 1). It receives more than half of fresh water from the Susquehanna River at the northern end and all salt input from the shelf through the southern entrance. The competition between salt and fresh water builds up a partially-mixed pattern which features a pycnocline and a two-layer circulation in the estuary. Deep water in the middle part of Chesapeake Bay becomes hypoxic every summer.

River flow is shown to contribute to seasonal hypoxia in the Bay via direct physical effects and indirect biological effects. Annual river flow usually peaks in spring-winter time. On the one hand, it delivers annual buoyancy to set up stratification, which isolates deep channel waters by suppressing vertical exchange, and drives a lower-layer circulation that acts to exchange particulate and dissolved materials [*Pritchard*, 1954; *Boicourt*, 1992]. On the other hand, it delivers major annual nutrients that fuel spring phytoplankton bloom growth and sinking, and the accumulation of organic matter provides substrate for oxygen consumption in bottom waters [*Taft et al. 1980; Kemp et al. 1992*].

In comparison to the river's control, we know less about wind's role on seasonal hypoxia in the Bay. Strong wind mixing contributes to periodic de-stratification [*Goodrich et al.*, 1987], especially in the middle reaches where tidal currents are modest [*Boicourt*, 1992]. Winds are also shown as a strong driver to along-channel exchange flow at synoptic time scales [*Wang*, 1979b; *Garvine*, 1985; *Chuang and*

Boicourt, 1989, *Li et al.*, 2005]. In addition, because the internal Rossby radius (about 5 km) is less than the channel width in most places; wind-induced lateral motions are significant in the Bay. It results in the lateral advection of hypoxic water from below the pycnocline onto the flanks of the Bay [*Malone et al.*, 1986; *Sanford et al.*, 1990; *Scully et al.*, 2010b].

Chesapeake Bay provides an excellent example to investigate the effects of climate variability and nutrient enrichment on hypoxia. As shown in Figure 1, the nutrient loading increased 3-4 fold between 1950s and 1980s, which was accompanied by a similar increase of hypoxic volume during the same period. However, the hypoxic volume continues to rise in recent years even though the nutrient loading has stabilized since mid-1990s. Moreover, despite significant seasonal cycle, there have been large interannual variations of the hypoxic volume over the past couple of decades: with severe hypoxia found during wet years and mild hypoxia found during dry years [*Hagy et al*., 2004]. A lengthy time-series from aircraft remote sensing (1989 –present) also found similar patterns in phytoplankton bloom, linking interannual variability of *chl-a* in the spring bloom and primary productivity to regional climate forcing [*Miller et al.*, 2006; *Miller and Harding*, 2007].

A range of multivariable statistical models have improved our understanding of controls on hypoxia. *Hagy et al.* [2004] attributed the long-term trend of hypoxia in the Bay to riverine nutrient loading, but could not explain hypoxia variability in

recent years. More recently, *Scully* [2010a] demonstrated that some of the internannual variations unaccounted for by nitrogen loads are positively correlated with the duration of westerly winds, while *Lee et al.* [submitted] found that summer hypoxia is significantly correlated with the late winter-spring (February-April) northeast-southwest (NE-SW) wind. Although retrospective analysis of data has led to stimulating new hypotheses on the role of climatic factors in the Bay, the mechanistic links between physical-biogeochemical controls and the variations of summer hypoxia are not fully understood. A complete understanding of the physical processes, especially the effects of winds and river flow, remains an obstacle to quantifying the climatic versus eutrophication effects.

5. Dissertation outline

The objective of this dissertation is to explore the effects of river flow and winds on estuarine circulation, stratification and hypoxia in Chesapeake Bay. Three-dimensional numerical models are used to carry out process-oriented experiments. The dissertation is organized as follows. Chapter 2 addresses the mechanism that drives wind-induced lateral circulation and its effects on along-channel momentum. Chapter 3 investigates how the lateral circulation affects stratification in a partially-mixed, rotating estuary. In chapter 4, an oxygen model is coupled to three-dimensional hydrodynamic model to explore the seasonal oxygen dynamics in Chesapeake Bay. The variations in river flow and wind forcing are quantitatively examined in terms of the changes in estuarine circulation, stratification and mixing,

and their influences on hypoxia volume are discussed. Finally, a brief summary is given in Chapter 6.

References

Andersson, L., and L. Rydberg (1988), Trends in nutrient and oxygen conditions within the Kattegat - Effects of local nutrient supply, *Estuarine Coastal Shelf Sci.*, *26*(5), 559-579, doi: 10.1016/0272-7714(88)90006-6.

Boicourt, W. C. (1992), Influences of circulation processes on dissolved oxygen in the Chesapeake Bay.

Borsuk, M. E., C. A. Stow, and K. H. Reckhow (2004), Confounding effect of flow on estuarine response to nitrogen loading, *J. Environ. Eng.*, *130*, 605, doi: 10.1061/(ASCE)0733-9372(2004)130:6(605).

Chan, F., J. Barth, J. Lubchenco, A. Kirincich, H. Weeks, W. Peterson, and B. Menge (2008), Emergence of anoxia in the California Current large marine ecosystem, *Science*, *319*(5865), 920-920, doi: 10.1126/science.1149016.

Chant, R. J. (2002), Secondary circulation in a region of flow curvature: Relationship with tidal forcing and river discharge, *J Geophys Res-Oceans*, *107*(3131), 207-223, doi: 10.1029/2001JC001082

Chatwin, P. (1976), Some remarks on the maintenance of the salinity distribution in estuaries, *Estuarine Coastal Mar. Sci.*, *4*(5), 555-566, doi: 10.1016/0302-3524(76)90030-X.

Chen, S.-N., and L. P. Sanford (2009a), Axial wind effects on stratification and longitudinal salt transport in an idealized, partially mixed estuary, *J. Phys. Oceanogr.*, *39*(8), 1905-1920, doi: 10.1175/2009JPO4016.1.

Chen, S.-N., L. P. Sanford, and D. K. Ralston (2009), Lateral circulation and sediment transport driven by axial winds in an idealized, partially mixed estuary, *J Geophys Res-Oceans*, *114*, C12006, doi: 10.1029/2008JC005014.

Cheng, P., R. E. Wilson, R. J. Chant, D. C. Fugate, and R. D. Flood (2009), Modeling influence of stratification on lateral circulation in a stratified estuary, *J. Phys. Oceanogr.*, *39*(9), 2324-2337, doi: 10.1175/2009JPO4157.1.

Chuang, W. S., and W. C. Boicourt (1989), Resonant Seiche Motion in the Chesapeake Bay, *J Geophys Res-Oceans*, *94*(C2), 2105-2110.

Cloern, J. E., A. E. Alpine, B. E. Cole, R. L. J. Wong, J. F. Arthur, and M. D. Ball (1983), River discharge controls phytoplankton dynamics in the northern San Francisco Bay estuary, *Estuar. Coast. Shelf Sci*, *16*(4), 415-426, doi: 10.1016/0272-7714(83)90103-8.

Conley, D. J., J. Carstensen, R. Vaquer-Sunyer, and C. M. Duarte (2009), Ecosystem thresholds with hypoxia, *Hydrobiologia*, *629*(1), 21-29, doi: 10.1007/s10750-009-9764-2.

Conley, D. J., J. Carstensen, G. Aertebjerg, P. B. Christensen, T. Dalsgaard, J. L. S. Hansen, and A. B. Josefson (2007), Long-term changes and impacts of hypoxia in Danish coastal waters, *Ecol. Appl.*, *17*(5), S165-S184, doi: 10.1890/05-0766.1.

Diaz, R. J. (2001), Overview of hypoxia around the world, *J. Environ. Qual.*, *30*(2), 275-281, doi: 10.2134/jeq2001.302275x.

Diaz, R. J., and R. Rosenberg (2008), Spreading dead zones and consequences for marine ecosystems, *Science*, *321*(5891), 926-929, doi: DOI: 10.1126/science.1156401.

Garvine, R. W. (1985), A simple-model of estuarine subtidal fluctuations forced by local and remote wind stress, *J. Geophys. Res.*, *90*(C6), 1945-1948, doi: 10.1029/JC090iC06p11945.

Geyer, W. R., J. H. Trowbridge, and M. M. Bowen (2000), The dynamics of a partially mixed estuary, *J. Phys. Oceanogr.*, *30*(8), 2035-2048, doi: 10.1175/1520-0485(2000)030<2035:TDOAPM>2.0.CO;2.

Geyer, W. R., J. D. Woodruff, and P. Traykovski (2001), Sediment transport and trapping in the Hudson River estuary, *Estuaries Coasts*, *24*(5), 670-679, doi: 10.2307/1352875.

Goodrich, D. M., W. C. Boicourt, P. Hamilton, and D. W. Pritchard (1987), Wind-induced destratification in Chesapeake Bay, *J. Phys. Oceanogr.*, *17*(12), 2232-2240, doi: 10.1175/1520-0485(1987)017<2232:WIDICB>2.0.CO;2.

Hansen, D. V., and J. M. Rattray (1965), Gravitational circulation in straits and estuaries, *J. Mar. Res.*, *23*(2), 104-122.

Harding, L. W., B. W. Meeson, and T. R. Fisher (1986), Phytoplankton production in two east coast estuaries: photosynthesis-light functions and patterns of carbon assimilation in Chesapeake and Delaware Bays, *Estuar. Coast. Shelf Sci*, *23*(6), 773-806, doi: 10.1016/0272-7714(86)90074-0.

Hetland, R. D., and W. R. Geyer (2004), An idealized study of the structure of long, partially mixed estuaries, *J. Phys. Oceanogr.*, *34*(12), 2677-2691, doi: 10.1175/JPO2646.1.

Howarth, R. W., D. P. Swaney, T. J. Butler, and R. Marino (2000), Rapid communication: Climatic control on eutrophication of the Hudson River Estuary, *Ecosystems*, *3*(2), 210-215, doi: 10.1007/s100210000020.

Johannessen, T., and E. Dahl (1996), Declines in oxygen concentrations along the Norwegian Skagerrak coast, 1927-1993: A signal of ecosystem changes due to eutrophication?, *Limnol. Oceanogr.*, 766-778.

Justić, D., R. E. Turner, and N. N. Rabalais (2003), Climatic influences on riverine nitrate flux: Implications for coastal marine eutrophication and hypoxia, *Estuaries*, *26*(1), 1-11, doi: 10.1007/BF02691688.

Justić, D., N. N. Rabalais, and R. E. Turner (2002), Modeling the impacts of decadal changes in riverine nutrient fluxes on coastal eutrophication near the Mississippi River Delta, *Ecol. Model.*, *152*(1), 33-46, doi: 10.1016/S0304-3800(01)00472-0.

Keller, A. A., C. A. Oviatt, H. A. Walker, and J. D. Hawk (1999), Predicted impacts of elevated temperature on the magnitude of the winter-spring phytoplankton bloom in temperate coastal waters: A mescosm study, *Limnol. Oceanogr.*, 344-356, doi: 10.4319/lo.1999.44.2.0344.

Kemp, W. M., P. A. Sampou, J. Garber, J. Tuttle, and W. R. Boynton (1992), Seasonal depletion of oxygen from bottom waters of Chesapeake Bay - Roles of benthic and planktonic respiration and physical exchange processes, *Mar. Ecol. Prog. Ser.*, *85*(1-2), 137-152.

Kemp, W. M., J. M. Testa, D. J. Conley, D. Gilbert, and J. D. Hagy (2009), Temporal responses of coastal hypoxia to nutrient loading and physical controls, *Biogeosciences*, *6*(12), 2985-3008, doi: 10.5194/bg-6-2985-2009.

Kemp, W. M., et al. (2005), Eutrophication of Chesapeake Bay: historical trends and ecological interactions, *Mar. Ecol. Prog. Ser.*, *303*, 1-29, doi: 10.3354/meps303001.

Lacy, J. R., M. T. Stacey, J. R. Burau, and S. G. Monismith (2003), Interaction of lateral baroclinic forcing and turbulence in an estuary, *J Geophys Res-Oceans*, *108*(C3), 3089, doi: 10.1029/2002JC001392.

Lee, Y. J., B. R. Walter, M. Li and Y. Li (submitted), The role of winter-spring wind and other factors controlling summer hypoxia in Chesapeake Bay, *Estuaries Coasts*.

Lehman, P. W. (1992), Environmental factors associated with long-term changes in chlorophyll concentration in the Sacramento-San Joaquin Delta and Suisun Bay, California, *Estuaries Coasts*, *15*(3), 335-348, doi: 10.2307/135278.

Lerczak, J. A., and W. R. Geyer (2004), Modeling the lateral circulation in straight, stratified estuaries, *J. Phys. Oceanogr.*, *34*(6), 1410-1428, doi: 10.1175/1520-0485(2004)034<1410:MTLCIS>2.0.CO;2.

Lerczak, J. A., W. R. Geyer, and D. K. Ralston (2009), The temporal response of the length of a partially stratified estuary to changes in river flow and tidal amplitude, *J. Phys. Oceanogr.*, *39*(4), 915-933, doi: 10.1175/2008JPO3933.1.

Li, Y., and M. Li (2011), Effects of winds on stratification and circulation in a partially mixed estuary, *J. Geophys. Res.*, *116*, C12012, doi: 10.1029/2010JC006893.

Li, M., L. J. Zhong, and W. C. Boicourt (2005), Simulations of Chesapeake Bay estuary: Sensitivity to turbulence mixing parameterizations and comparison with observations, *J. Geophys. Res.*, *110*(C12), -, doi 10.1029/2004jc002585.

Li, M., L. Zhong, W. C. Boicourt, S. L. Zhang, and D. L. Zhang (2007), Hurricane-induced destratification and restratification in a partially-mixed estuary, *J. Mar. Res.*, *65*(2), 169-192.

MacCready, P., and W. R. Geyer (2010), Advances in estuarine physics, *Ann. Rev. Mar. Sci.*, *2*, 35-58, doi: 10.1146/annurev-marine-120308-081015.

Malone, T. C. (1991), River flow, phytoplankton production and oxygen depletion in Chesapeake Bay, *Geological Society, London, Special Publications*, *58*(1), 83-93, doi: 10.1144/GSL.SP.1991.058.01.06.

Malone, T. C., W. M. Kemp, H. W. Ducklow, W. R. Boynton, J. H. Tuttle, and R. B. Jonas (1986), Lateral variation in the production and fate of phytoplankton in a partially stratified estuary, *Mar. Ecol. Prog. Ser.*, *32*(2-3), 149-160, doi: 10.3354/meps032149.

Miller, W. D., and L. Harding (2007), Climate forcing of the spring bloom in Chesapeake Bay, *Mar. Ecol. Prog. Ser.*, *331*, 11-22, doi: 10.3354/meps331011.

Miller, W. D., L. W. Harding, and J. E. Adolf (2006), Hurricane Isabel generated an unusual fall bloom in Chesapeake Bay, *Geophys. Res. Lett.*, *33*(6), doi: 10.1029/2005GL025658.

Nunes, R., and J. Simpson (1985), Axial convergence in a well-mixed estuary, *Estuarine Coastal Shelf Sci.*, *20*(5), 637-649, doi: 10.1016/0272-7714(85)90112-X.

O'Donnell, J., H. G. Dam, W. F. Bohlen, W. Fitzgerald, P. S. Gay, A. E. Houk, D. C. Cohen, and M. M. Howard-Strobel (2008), Intermittent ventilation in the hypoxic zone of western Long Island Sound during the summer of 2004, *J. Geophys. Res.*, *113*, C09025, doi: 10.1029/2007JC004716.

Officer, C., R. Biggs, J. Taft, L. Cronin, M. Tyler, and W. Boynton (1984), Chesapeake Bay anoxia: origin, development, and significance, *Science*, *223*(4631), 22, doi: 10.1126/science.223.4631.22.

Parker, C. A., and J. E. O'Reilly (1991), Oxygen depletion in Long Island Sound: a historical perspective, *Estuaries Coasts*, *14*(3), 248-264, doi: 10.2307/1351660.

Peierls, B. L., R. R. Christian, and H. W. Paerl (2003), Water quality and phytoplankton as indicators of hurricane impacts on a large estuarine ecosystem, *Estuaries*, *26*(5), 1329-1343, doi: 10.1007/BF02803635.

Pritchard, D. W. (1954), A study of the salt balance in a coastal plain estuary, *J. Mar. Res.*, *13*(1), 133-144.

Ralston, D. K., W. R. Geyer, and J. A. Lerczak (2008), Subtidal salinity and velocity in the Hudson River estuary: Observations and modeling, *J. Phys. Oceanogr.*, *38*(4), 753-770, doi: 10.1175/2007JPO3808.1.

Rattray, M., and D. V. Hansen (1962), A similarity solution for circulation in an estuary, *J. Mar. Res.*, *20*(2), 121-133.

Reyes-Hernández, C., and A. Valle-Levinson (2010), Wind modificiations to density-driven flows in semienclosed, rotating basins, *J. Phys. Oceanogr.*, *40*, 1473-1487, doi: 10.1175/2010JPO4230.1

Rosenberg, R. (1990), Negative oxygen trends in Swedish coastal bottom waters, *Marine Pollution Bulletin*, *21*(7), 335-339, doi: 10.1016/0025-326X(90)90794-9.

Sanford, L. P., and W. C. Boicourt (1990), Wind-forced salt intrusion into a tributary estuary, *J. Geophys. Res.*, *95*(C8), 13357-13371, doi: 10.1029/JC095iC08p13357.

Scully, M. E. (2010a), The importance of climate variability to wind-driven modulation of hypoxia in Chesapeake Bay, *J. Phys. Oceanogr.*, *40*(6), 1435-1440, doi: 10.1175/2010JPO4321.1.

Scully, M. E. (2010b), Wind modulation of dissolved oxygen in Chesapeake Bay, *Estuaries Coasts*, *33*(5), 1164-1175, doi: 10.1007/s12237-010-9319-9.

Scully, M. E., C. Friedrichs, and J. Brubaker (2005), Control of estuarine stratification and mixing by wind-induced straining of the estuarine density field, *Estuaries*, *28*(3), 321-326, doi: 10.1007/BF02693915.

Scully, M. E., W. R. Geyer, and J. A. Lerczak (2009), The influence of lateral advection on the residual estuarine circulation: A numerical modeling study of the Hudson River Estuary, *J. Phys. Oceanogr.*, *39*(1), 107-124, doi:10.1175/2008jpo3952.1.

Shen, J., T. Wang, J. Herman, P. Mason, and G. L. Arnold (2008), Hypoxia in a coastal embayment of the Chesapeake Bay: A model diagnostic study of oxygen dynamics, *Estuaries Coasts*, *31*(4), 652-663, doi: 10.1007/s12237-008-9066-3.

Simpson, J. H., J. Brown, J. Matthews, and G. Allen (1990), Tidal straining, density currents, and stirring in the control of estuarine stratification, *Estuaries*, *13*(2), 125-132, doi: 10.2307/1351581.

Smith, E., and W. Kemp (1995), Seasonal and regional variations in plankton community production and respiration for Chesapeake Bay, *Mar. Ecol. Prog. Ser.*, *116*(1), 217-231.

Taft, J. L., W. R. Taylor, E. O. Hartwig, and R. Loftus (1980), Seasonal oxygen depletion in Chesapeake Bay, *Estuaries Coasts*, *3*(4), 242-247, doi: 10.2307/1352079.

Townsend, D. W., and L. M. Cammen (1988), Potential importance of the timing of spring plankton blooms to benthic-pelagic coupling and recruitment of juvenile demersal fishes, *Biol. Oceanogr*, *5*(3), 215-228.

Tyler, R. M., D. C. Brady, and T. E. Targett (2009), Temporal and spatial dynamics of diel-cycling hypoxia in estuarine tributaries, *Estuaries Coasts*, *32*(1), 123-145, doi: 10.1007/s12237-008-9108-x.

Verity, P. G., M. Alber, and S. B. Bricker (2006), Development of hypoxia in well-mixed subtropical estuaries in the southeastern USA, *Estuaries Coasts*, *29*(4), 665-673, doi: 10.1007/BF02784291.

Wang, D. P. (1979a), Subtidal sea-level variations in the Chesapeake Bay and relations to atmospheric forcing, *J. Phys. Oceanogr.*, *9*(2), 413-421, doi: 10.1175/1520-0485(1979)009<0413:SSLVIT>2.0.CO;2.

Wang, D. P. (1979b), Wind-driven circulation in the Chesapeake Bay, winter 1975, *J. Phys. Oceanogr.*, *9*(3), 564-572, doi: 10.1175/1520-0485(1979)009<0564:WDCITC>2.0.CO;2.

Wei, H., Y. C. He, Q. J. Li, Z. Y. Liu, and H. T. Wang (2007), Summer hypoxia adjacent to the Changjiang Estuary, *J. Marine Syst.*, *67*(3-4), 292-303, doi: 10.1016/j.jmarsys.2006.04.014.

Welsh, B. L., and F. C. Eller (1991), Mechanisms controlling summertime oxygen depletion in western Long Island Sound, *Estuaries Coasts*, *14*(3), 265-278, doi: 10.2307/1351661.

Wilson, R. E., R. L. Swanson, and H. A. Crowley (2008), Perspectives on long-term variations in hypoxic conditions in western Long Island Sound, *J. Geophys. Res.*, *113*, C12011, doi: 10.1029/2007JC004693.

Winant, C. (2004), Three-dimensional wind-driven flow in an elongated, rotating basin, *J. Phys. Oceanogr.*, *34*(2), 462-476, doi: 10.1175/1520-0485(2004)034<0462:TWFIAE>2.0.CO;2.

Wong, K. C., and A. Valle-Levinson (2002), On the relative importance of the remote and local wind effects on the subtidal exchange at the entrance to the Chesapeake Bay, *J. Mar. Res.*, *60*(3), 477-498.

Figures

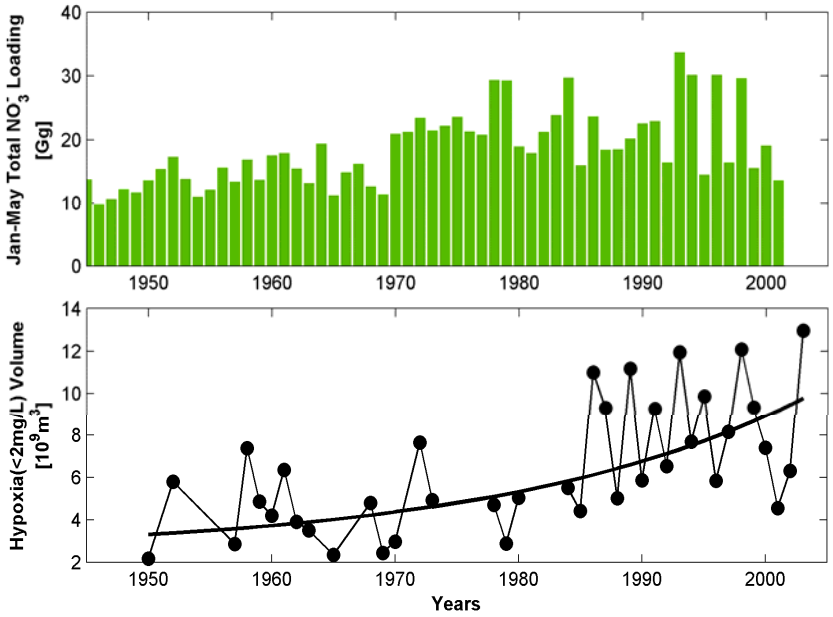

Figure 1.1 The spring NO_3^- loads and summer hypoxia volume from 1950 to 2004 in Chesapeake Bay (data from Hagy and Boynton).

Chapter 2: Wind-Driven Lateral Circulation in a Stratified Estuary and its Effects on the Along-Channel Flow[1]

Abstract

In the stratified rotating estuary of Chesapeake Bay, the Ekman transport drives a counterclockwise lateral circulation under down-estuary winds and a clockwise lateral circulation under up-estuary winds (looking into estuary). The clockwise circulation is about twice as strong as the counterclockwise circulation. Analysis of the streamwise vorticity equation reveals a balance among three terms: the conversion of the planetary vorticity by vertical shear in the along-channel current, baroclinic forcing due to sloping isopycnals at cross-channel sections, and turbulent diffusion. The baroclinic forcing is highly asymmetric between the down- and up-estuary winds. While the counter-clockwise lateral circulation tilts isopycnals vertically and creates lateral barolinic pressure gradient to oppose the Ekman transport under the down-estuary wind, the clockwise circulation initially flattens the isopycnals and the baroclinic forcing reinforces the Ekman transport under the up-estuary wind. The Coriolis acceleration associated with the lateral flows is of the first-order importance in the along-channel momentum balance. It has a sign opposite to the stress divergence in the surface layer and the pressure gradient in the bottom layer, thereby reducing the shear in the along-channel current. Compared with the non-rotating system, the shear reduction is about 30-40%. Two summary diagrams are constructed to show how the averaged streamwise vorticity and along-channel current shear vary with the Wedderburn (W) and Kelvin (Ke) numbers.

[1] Li, Y., and M. Li (2012), Wind-Driven Lateral Circulation in a Stratified Estuary and its Effects on the Along-Channel Flow, *J. Geophys. Res.* doi:10.1029/2011JC007829

1. Introduction

The wind-driven circulation in an estuary has previously been interpreted in terms of the competition between the wind stress and barotropic pressure gradient due to sea-level setup in the along channel direction [*Weisberg and Sturges*, 1976; *Wang*, 1979; *Garvine*, 1985; *Janzen and Wong*, 2002]. In a rectangular estuary or a stratified estuary where the buoyancy flux is strong, the along-channel flow consists of a vertically sheared two-layer circulation: downwind currents in the surface layer and upwind currents in the bottom layer [e.g. *Chen and Sanford*, 2009; *Reyes-Hernandez and Valle-Levinson*, 2010]. In estuaries with lateral variations of bathymetry, the depth-dependence in the longitudinal momentum balance leads to laterally sheared three-layer circulation: downwind currents on the shallow shoals and upwind flows in the center deep channel [e.g. *Wong*, 1994; *Friedrichs and Hamrick*, 1996]. However, this picture of wind-driven circulation in a stratified rotating estuary is incomplete.

Several studies have shown that along-channel winds can drive strong lateral Ekman flows and isopycnal movements, generating upwelling/downwelling at shallow shoals [*Malone et al.*, 1986; *Sanford et al.*, 1990; *Wilson et al.*, 2008; *Scully*, 2010]. These lateral motions are fundamental to estuarine dynamics because they transport momentum [*Lerczak and Geyer*, 2004; *Scully et al.*, 2009], alter stratification [*Lacy et al.*, 2003; *Li and Li*, 2011] and transport sediment [*Geyer et al.*, 2001; *Chen et al.*, 2009]. For example, *Li and Li* [2011] showed that the wind-driven lateral circulation causes lateral straining of the density field which offsets the effects

of longitudinal straining. Furthermore, the lateral circulations provide an exchange pathway for biologically important materials such as nutrients and oxygen, especially through lateral upwelling and downwelling [*Malone et al.*, 1986; *Sanford et al.*, 1990; *Reynolds-Fleming and Luettich*, 2004]. A recent study suggests that, in Chesapeake Bay, the wind-driven lateral exchange of oxygen between shoal regions and deeper hypoxic areas is more important than direct turbulent mixing through the pycnocline [*Scully*, 2010]. Despite these interesting studies, the dynamics of wind-driven lateral circulations in stratified estuaries of varying width are still poorly understood. A simple scaling suggests that the redistribution of momentum by lateral flows is expected to play a larger role in narrow estuaries where lateral gradients in the along-channel momentum are bigger. However, wider estuaries are expected to have a stronger lateral response to the along-channel wind forcing because of rotation.

There have been a series of interesting studies on the dynamics of lateral circulations in tidally driven estuaries. Several mechanisms have been proposed, including differential advection [*Nunes and Simpson*, 1985; *Lerczak and Geyer*, 2004], bottom Ekman layer [*Scully et al.*, 2009], diffusive boundary layer on a slope [*Chen et al.*, 2009], channel curvature [*Chant*, 2002] and lateral salinity gradient resulting from the presence of stratification [*Lerczak and Geyer*, 2004; *Scully et al.*, 2009; *Cheng et al.*, 2009]. Using a numerical model of an idealized estuarine channel, *Lerczak and Geyer* [2004] demonstrated that the lateral flows are driven primarily by differential advection and cross-channel density gradients, and exhibit strong flood-ebb and spring-neap variability. In a subsequent study of Hudson River estuary, *Scully*

et al. [2009] showed that nonlinear tidal advection by lateral Ekman transport generates one-cell lateral circulation over flood-ebb tidal cycle, as found in an analytic model of *Huijts et al.* [2009]. Most of these previous studies focused on the analysis of the along-channel and cross-channel momentum balance. Since the leading-order momentum balance in the cross-channel direction is the thermal-wind balance, *Scully et al*. [2009] discussed the ageostrophic term and provided insightful discussions on the interactions between the lateral Ekman flows and lateral baroclinic pressure gradient. In this chapter we develop a new approach to investigate the dynamics of lateral circulations. We will investigate the streamwise (along-channel) vorticity which provides a scalar representation of the lateral circulation, and conduct diagnostic analysis of the streamwise vorticity equation to identify the generation and dissipation mechanisms.

A major motivation for studying the lateral circulation in estuaries is the need to understand its effects on the along-channel estuarine exchange flows. In tidally driven estuaries, recent modeling investigations have demonstrated that the lateral advection is of the first-order importance in the along-channel momentum balance [*Lerczak and Geyer*, 2004; *Scully et al.*, 2009; *Cheng et al.*, 2009]. *Burchard et al.* [2011] and *Burchard and Schuttelaars* [2012] decomposed the estuarine residual circulation into contributions from processes such as tidal straining circulation, gravitational circulation, advectively driven circulation, and horizontal mixing circulation. They found that the lateral advection can be a major driving force for the estuarine circulation in some estuaries. This motives us to examine the effects of the lateral

flows on the wind-driven flows in the along-channel direction. It will be shown that the Coriolis acceleration associated with the lateral circulation is of the first-order importance in the along-channel momentum balance. Unlike the nonlinear advection term which augments the along-channel flows, however, the Coriolis acceleration reduces the shear in the along-channel current.

Using Chesapeake Bay as an example of a partially mixed/stratified estuary, *Li and Li* [2011] investigated how the wind-driven lateral circulation causes the lateral straining of density field and how this lateral straining offsets the effects of longitudinal straining to reduce the stratification-reduction asymmetry between the down- and up-estuary winds. This is a companion paper where we examine the vorticity dynamics of the wind-driven lateral circulation and its effects on the along-channel flows. The plan for this chapter is as follows. In Section 2 we describe the model configuration and introduce the analysis approach. Section 3 is devoted to the analysis of the streamwise vorticity equation while Section 4 is devoted to the analysis of the along-channel momentum balance. In Section 5, we summarize the model results in a non-dimensional parameter space consisting of the Wedderburn (W) and Kelvin (Ke) numbers.

2. Model configuration and analysis approach

To study wind-driven lateral flows, we use a 3D hydrodynamic model of Chesapeake Bay based on ROMS (Regional Ocean Modeling System) [*Li et al.*, 2005, 2007; *Zhong and Li*, 2006; *Zhong et al.*, 2008; *Li and Zhong*, 2009]. The model

domain covers 8 major tributaries and a part of the coastal ocean to allow free exchange across the bay mouth (Fig. 1). The total number of grid points is 120 × 80. The model has 20 layers in the vertical direction. A quadratic stress is exerted at the bed, assuming that the bottom boundary layer is logarithmic over a roughness height of 0.5 mm. The vertical eddy viscosity and diffusivity are computed using the *k-kl* turbulence closure scheme [*Warner et al.*, 2005] with the background diffusivity and viscosity set at 10^{-5} m^2 s^{-1}. The horizontal eddy viscosity and diffusivity are set to 1 m^2 s^{-1}. The model is forced by tides at the offshore boundary, by freshwater inflows at river heads, and by winds across the water surface. The open-ocean boundary condition consists of Chapman's condition for surface elevation, Flather's condition for barotropic velocity, Orlanski-type radiation condition for baroclinic velocity, and a combination of radiation condition and nudging (with a relaxation time scale of 1 day) for scalars [*Marchesiello et al.*, 2001].

In this chapter we conduct process-oriented idealized modeling studies. At the open-ocean boundary, the model is forced by M_2 tides only and salinity is fixed at 30 psu. The total river discharge into the Bay is kept at the long-term average of 1500 m^3 s^{-1} and is distributed to 8 major tributaries according to observations: Susquehanna (51%), Patapsco (3.67%), Patuxent (3.67%), Potomac (18%), Rappahannock (4%), York (2%), James (14%), and Choptank (3.67%) [c.f., *Guo and Valle-Levison*, 2008]. We first run the model without wind forcing for 5 years so that the circulation and stratification in the Bay reaches a steady-state. We then force the model with the along-channel (southward or northward) winds of varying amplitudes and directions.

Cross-channel (eastward or westward) winds are not considered here because of fetch limitation. The wind stress is spatially uniform and is given by

$$\tau_W = \begin{cases} \tau_p \sin[\omega(t-25)] & 25 \le t \le 27.5 \\ 0 & \textit{other times} \end{cases} \tag{1}$$

where τ_W is the along-channel wind stress, t the time (days), $\omega = \frac{2\pi}{5day}$ the frequency of the wind forcing, and τ_p the peak wind stress. Positive τ_W corresponds to up-estuary (northward) winds whereas negative τ_W corresponds to down-estuary (southward) winds. The maximum wind-stress magnitude τ_p ranges from 0.005 to 0.25 Pa, with the corresponding range of 2.35 to 12.27 m s^{-1} for the wind speed (Table 1).

Previous investigations of lateral circulations in estuaries have mainly focused on the analysis of the cross-channel momentum equation [e.g. *Lerczak and Geyer*, 2004; *Scully et al.*, 2009]

$$\underbrace{\frac{\partial v}{\partial t}}_{\text{acceleration}} = \underbrace{-fu}_{\substack{\text{Coriolis} \\ \text{acceleration}}} \underbrace{-\frac{1}{\rho}\frac{\partial P}{\partial y}}_{\text{pressure gradient}} \underbrace{-\left(u\frac{\partial v}{\partial x} + v\frac{\partial v}{\partial y} + w\frac{\partial v}{\partial z}\right)}_{\text{nonlinear advection}} + \underbrace{\frac{\partial}{\partial z}\left(K_V \frac{\partial v}{\partial z}\right)}_{\text{stress divergence}} \tag{2}$$

where (u, v, w) are the velocity components in the along-channel (x-), cross-channel (y-) and vertical (z-) directions. Consistent with the previous definition of the Wedderburn number [*Chen and Sanford*, 2009; *Li and Li*, 2011], the positive x-axis is

pointed northward, the positive y-axis is pointed westward, and the positive z-axis is pointed upward. The lateral pressure gradient consists of two terms: lateral sea-level slope and lateral density gradient.

Here we adopt a new approach by analyzing the equation of the streamwise (along-channel) vorticity defined as $\omega_x = \frac{\partial w}{\partial y} - \frac{\partial v}{\partial z}$. If one looks into estuary in the northern hemisphere, a clockwise/counterclockwise lateral circulation corresponds to positive/negative ω_x. The strength of lateral circulation is represented by the absolute value of ω_x. The equation for ω_x is given by

$$\begin{aligned}\frac{d\omega_x}{dt} &= f\frac{\partial u}{\partial z} + (\omega_x \frac{\partial u}{\partial x} + \omega_y \frac{\partial u}{\partial y} + \omega_z \frac{\partial u}{\partial z}) \\ &+ \left[\frac{\partial}{\partial y}(-\frac{1}{\rho}\frac{\partial P}{\partial z}) - \frac{\partial}{\partial z}(-\frac{1}{\rho}\frac{\partial P}{\partial y})\right] \\ &+ \frac{\partial}{\partial x}\left[\frac{\partial}{\partial y}(K_H \frac{\partial w}{\partial x}) - \frac{\partial}{\partial z}(K_H \frac{\partial v}{\partial x})\right] \\ &+ \frac{\partial}{\partial y}\left[\frac{\partial}{\partial y}(K_H \frac{\partial w}{\partial y}) - \frac{\partial}{\partial z}(K_H \frac{\partial v}{\partial y})\right] \\ &+ \frac{\partial}{\partial z}\left[\frac{\partial}{\partial y}(K_V \frac{\partial w}{\partial z}) - \frac{\partial}{\partial z}(K_V \frac{\partial v}{\partial z})\right]\end{aligned} \tag{3}$$

where (ω_y, ω_z) are the vorticity components in the cross-channel and vertical directions, ρ the density, P the pressure, and K_H and K_V are eddy viscosity in the vertical and horizontal directions [c.f., *Kundu and Cohen*, 2004]. Equation (3) shows that the streamwise vorticity ω_x can be generated by the conversion of the planetary

vorticity f [2] due to the vertical shear in the along-channel current, by vortex stretching/tilting, by baroclinicity in the cross-channel section (misalignment of pressure and density surfaces), and is diffused by subgrid-scale turbulent flows.

Making the Boussinesq approximation for the horizontal momentum equations and the hydrostatic assumption for the vertical momentum equation, and assuming that the variation in the along-channel direction is weak (i.e. $\partial/\partial x$=0), we obtain the following simplifications:

$$\omega_x = -\frac{\partial v}{\partial z}, \quad \omega_y = \frac{\partial u}{\partial z}, \quad \omega_z = -\frac{\partial u}{\partial y}, \tag{4}$$

$$P = p_a + g\rho_0\eta + g\int_z^0 \rho'(z')dz', \tag{5}$$

$$\frac{\partial}{\partial y}\left(-\frac{1}{\rho}\frac{\partial P}{\partial z}\right) = \frac{\partial g}{\partial y} = 0, \tag{6}$$

$$-\frac{\partial}{\partial z}\left(-\frac{1}{\rho}\frac{\partial P}{\partial y}\right) \approx -\frac{\partial}{\partial z}\left(-g\frac{\partial \eta}{\partial y} + \frac{g}{\rho_0}\int_0^z \frac{\partial \rho'}{\partial y}dz'\right) = -\frac{g}{\rho_0}\frac{\partial \rho'}{\partial y} \approx -g\beta\frac{\partial S}{\partial y} \tag{7}$$

in which p_a is the atmospheric pressure, g the gravitational constant, η the sea surface height, ρ' the density perturbations, and β the saline contraction coefficient. The last step in Eq. (7) is derived by using the linear equation of state and assuming

[2] *Li and Li* [2012] called this term as 'tilting of the planetary vorticity *f*', more specifically, it represents the tilting of vortex tube generated by the planetary vorticity *f*. However, *f* is defined by the earth's rotation and always points normal to the earth surface. In order to avoid confusion, we reworded the name as 'conversion of the planetary vorticity *f*' in this dissertation.

uniform temperature in the estuary. Substituting Eqs. (4)-(7) into Eq. (3) leads to

$$\frac{d\omega_x}{dt} = \underbrace{f\frac{\partial u}{\partial z}}_{\substack{\text{conversion of}\\ \text{planetary vorticity}}} \underbrace{-g\beta\frac{\partial S}{\partial y}}_{\text{baroclinicity}} + \underbrace{\frac{\partial^2}{\partial z^2}\left(K_V\omega_x\right)}_{\substack{\text{vertical}\\ \text{diffusion}}} + \underbrace{\frac{\partial^2}{\partial y^2}\left(K_H\omega_x\right)}_{\substack{\text{horizontal}\\ \text{diffusion}}} \tag{8}$$

in which the horizontal eddy viscosity K_H is assumed to be a constant. In Eq. (8), the conversion of planetary vorticity by shear in the along-channel flow and the baroclinicity due to the sloping isopycnals in the cross-channel sections are two terms generating the streamwise vorticity whereas the vertical and horizontal diffusion act to reduce it. The vorticity generation due to the stretching and tilting of relative vorticity is zero since $\partial/\partial x$=0. Equation (8) can also be derived by taking -$\partial/\partial z$ of Eq. (2) and using the hydrostatic approximation to calculate the pressure distribution. In the ROMS model, the equations of motions are solved in a transformed coordinate system which has a generalized topography-following σ coordinate in the vertical direction and orthogonal curvilinear coordinates in the horizontal directions [*Haidvogel et al.*, 2000]. To utilize ROMS diagnostic outputs for the analysis of vorticity dynamics, we transform Eq. (8) into an equation in the ROMS coordinate. Please see Appendix B for details.

Another goal of this chapter is to examine how the wind-driven lateral circulation affects the along-channel flow. The along-channel momentum equation is given by

$$\frac{\partial u}{\partial t} = \underbrace{-\frac{1}{\rho}\frac{\partial P}{\partial x}}_{\substack{\text{pressure}\\ \text{gradient}}} + \underbrace{\frac{\partial}{\partial z}\left(K_V \frac{\partial u}{\partial z}\right)}_{\substack{\text{stress}\\ \text{divergence}}} + \underbrace{fv}_{\substack{\text{Coriolis}\\ \text{acceleration}}} \underbrace{-\left(u\frac{\partial u}{\partial x} + v\frac{\partial u}{\partial y} + w\frac{\partial u}{\partial z}\right)}_{\substack{\text{nonlinear}\\ \text{advection}}}. \quad (9)$$

The first two terms on the right-hand side of Eq. (9) are the pressure gradient and stress divergence. The response of an idealized rectangular estuary to axial wind forcing is shown to consist of a vertically sheared two-layer circulation and has been interpreted in terms of the competition between the stress divergence and pressure gradient due to sea-level setup [e.g. *Wang*, 1979; *Garvine*, 1985; *Janzen and Wong*, 2002]. The stress divergence overcomes the pressure gradient to drive the downwind flow in the surface layer whereas the pressure gradient overcomes the stress divergence to drive the upwind flow in the bottom layer. If the lateral flows are strong, however, the Coriolis acceleration and nonlinear advection can also play important roles in the along-channel momentum balance. They will be investigated in this chapter. Appendices A and B give details on the diagnostic analyses of the momentum and vorticity equations using ROMS model outputs.

3. Vorticity dynamics of lateral circulation

In Chesapeake Bay where the baroclinic Rossby radius (about 5 km) is smaller than or comparable to the width of the estuary (5-20 km), the along-channel winds can drive lateral Ekman flows and isopycnal movements, generating upwelling/downwelling at shallow shoals [*Malone et al.*, 1986; *Sanford et al.*, 1990; *Scully*, 2010]. In this section, we investigate the dynamics of wind-driven lateral

circulation using the streamwise vorticity as the primary diagnostic quantity. First we show distributions of salinity, along- and cross-channel velocities at a cross-channel section, and study how they evolve during a down-/up-estuary wind event. We then examine temporal evolution of the streamwise vorticity and conduct diagnostic analysis of the vorticity equation to explore the generation mechanisms for the lateral circulation.

Figure 2 shows the estuary's response to the down-estuary (southward) wind with the peak wind stress τ_p = -0.07 Pa. We apply a 34-hour low-pass filter to remove tidal oscillations. The southward wind drives a westward Ekman flow (positive v) in the upper layer (about 4 m deep), which in turn drives an eastward return flow (negative v) in the lower layer. A counterclockwise circulation thus appears in the cross-channel section, with the cross-channel speed reaching about 0.1 m s^{-1} (Fig. 2a). This circulation cell is situated over the deep channel and eastern shoal, but flows on the western shoal are directed eastward where a strong lateral salinity gradient exists (Fig. 2c). The southward wind drives a seaward along-channel flow (negative u) in the upper layer and a landward flow (positive u) in the lower layer, reinforcing the two-layer gravitational circulation (Fig. 2b). However, the bottom return flow breaks into the surface over the center channel. The counterclockwise lateral circulation strains the salinity field and tilts the isopycnals (isohalines) towards the vertical direction, as shown in Fig. 2c (see *Li and Li* [2011] for more detailed discussion).

At the peak wind, the surface Ekman layer deepens to over 5 m depth and the

lateral circulation strengthens such that the maximum cross-channel velocity reaches about 0.15 m s^{-1} (Fig. 2d). The along-channel current also gets stronger: both the downwind current in the upper layer and upwind current in the lower layer reach a maximum of 0.30 m s^{-1} (Fig. 2e). Continued vertical tilting of isopycnals and vertical mixing almost erase stratification in the upper layer, as shown in Fig. 2f. In weakly stratified water, the effects of the bottom bathymetry become important such that the along-channel flows are laterally sheared with the upwind flow in the center channel [*Csanady*, 1973; *Wong*, 1994; *Winant*, 2004]. During the set-down phase of the wind event, the counterclockwise circulation is still strong on the eastern half of the cross-section, but flows on the western half are directed eastward due to the lateral density gradients there (Figs. 2g and 2i). Therefore, the wind-driven lateral circulation in a stratified estuary is not solely determined by the wind forcing but is also affected by the cross-channel density gradient and vertical stratification.

The streamwise vorticity ω_x provides a concise description of the lateral circulation, as shown in Figs. 2a, 2d and 2g. The counterclockwise lateral circulation is represented by negative values of ω_x. Strong negative vorticity emerges over the eastern half of the cross-channel section, which corresponds well with the counterclockwise circulation there. Near the bottom boundary on the shallow shoals and inside the deep channel, *v* slows down as the bottom is approached such that ω_x is positive. As the wind speed increases, the magnitude of ω_x becomes larger and the region of negative ω_x occupies a larger area of the water column. When the wind speed decreases, ω_x becomes weaker and the lateral circulation spins down.

The sense of the lateral circulation is reversed under the up-estuary (northward) wind forcing since the wind-driven Ekman transport is now directed eastward (Fig. 3). The one-cell clockwise circulation extends over the whole cross-channel section, strengthens as the wind speed increases, and then weakens as the wind speed decreases. The cross-channel velocity v reaches a maximum speed of 0.2 m s^{-1}. Compared with counterclockwise circulation generated by the down-estuary wind, the clockwise circulation generated by the up-estuary wind is much stronger. The distribution of the streamwise vorticity ω_x also shows the asymmetry clearly: the magnitude of ω_x generated by the up-estuary wind is 2-3 times as large as that generated by the down-estuary wind. The maximum value of ω_x reaches ~ $11 \times 10^{-2} s^{-1}$ at the peak wind. In the absence of wind forcing, the along-channel flow features a seaward flow in a surface layer hugging the western shore and a landward flow sitting in deep channel. The up-estuary northward wind generates landward flows in the upper layer and seaward flows in the lower layer. Initially, the gravitational circulation still dominates, as shown in Fig. 3b. At the peak wind, however, the wind-driven circulation reverses the gravitational circulation, with the upper layer moving up-estuary and the lower layer moving down-estuary (Fig. 3e). This circulation persists and gradually weakens until the end of wind event. It should be noted that the along-channel flow generated by the up-estuary wind is about 1/3 to 1/2 of the flow generated by the down-estuary wind (compare Figs. 3b, 3e, 3h with Figs. 2b, 2e, 2h). Moreover, the vertical stratification under the up-estuary wind is significantly stronger than that under the down-estuary wind. Upwelling flows lift isopycnals on

the western side up from the depressed positions (Fig. 3c and 3f). Compared with the down-estuary wind case (Fig. 2c and 2f), the isopycnals appear to be more horizontal, and significant stratification is retained in the top 5 meters and strong Ekman flow is confined to a relatively shallow surface layer. The stratification lessens the effects of bottom bathymetry on the flow structure. Hence, the along-channel flows appear to be more vertically sheared than laterally sheared. During the second half of the wind event, the continued straining of salinity field by the clockwise circulation tilts isopycnals towards the vertical direction (Fig. 3i).

The above analysis suggests that the Ekman transport is the primary driving force for the lateral circulation but other factors such as the lateral density gradient and vertical stratification also play important roles in determining the strength of the lateral circulation. To gain insights into the generation mechanisms, we conduct diagnostic analysis of the streamwise vorticity equation and select the peak wind as the time slice for the analysis. The dominant terms in the vorticity budget are the conversion of planetary vorticity by the shear in the along-channel flows, vertical diffusion and the baroclinicity due to sloping isopycnals in cross-channel sections. The horizontal diffusion term is two-orders of magnitude smaller than the vertical diffusion term. The nonlinear advection term is weak, and the time tendency $\partial\omega_x / \partial t$ is also small (Figs. 4g and 4h). Not surprisingly, the sign of the streamwise vorticity (or the sense of the lateral circulation) is set by the conversion of planetary vorticity by the along-channel current (Figs. 4a and 4b). The down-estuary wind generates the southward (negative) along-channel current. The vertical shear bends *f* down toward

the bay mouth and generates a negative streamwise vorticity. In contrast, the up-estuary wind generates the northward (positive) along-channel current which tilts *f* to generate positive ω_x. The turbulent diffusion acts to spin down ω_x and smooth the spatial gradients in ω_x (Figs. 4c and 4d). This competition between the *fdu/dz* and diffusion terms provides an interpretation of the Ekman-driven lateral circulation in unstratified channel from the vorticity point of view. In stratified estuaries such as Chesapeake Bay, the barolinicity forcing is important and is a major cause for the asymmetry in ω_x between the down-estuary and up-estuary winds. Without the wind forcing, the brackish plume is pushed to the western shore, leading to higher sea level there. On the other hand, isopycnals are tilted downwards on the western shore. Since the total pressure is the sum of the barotropic and baroclinic pressure, the isobars and isopycnals at the cross-channel section are misaligned. The down-estuary wind steepens the slopes of the sea surface and isopycnals, particularly over the western half of the cross-channel section. Since the vertically tilted isopycnals tend to slump towards the horizontal equilibrium position, the baroclinic forcing generates positive ω_x (Fig. 4e). In contrast, the up-estuary wind lifts up the isopycnals from their initial depressed positions on the western shoal (Fig. 3f) such that the baroclinic forcing is relatively weaker (Fig. 4f).

The dynamics of the wind-driven lateral circulation can be illustrated more clearly by averaging the streamwise vorticity over a control volume (see Fig. 1) and calculating the volume-averaged terms in the vorticity equation (see Appendix B). The volume-averaged $\overline{\omega_x}$ has a small value of -0.069×10^{-2} s^{-1} before the onset of

wind event (Fig. 5a). It spins up as the wind stress increases and spins down as the wind decreases. A large difference is found in the strength of $\overline{\omega_x}$ between the down- and up-estuary winds. $\overline{\omega_x}$ peaks at -0.54×10^{-2} s^{-1} during the down-estuary wind but at 1.32×10^{-2} s^{-1} (nearly 3 times larger) during the up-estuary wind (Fig. 5a and 5c). To understand what causes such an asymmetry, we compare the volume-averaged terms in the vorticity equation. Before the onset of wind forcing, the conversion of planetary vorticity $\overline{f\frac{\partial u}{\partial z}}$ (negative) is balanced by the baroclinic forcing $\overline{-g\beta\frac{\partial S}{\partial y}}$ (positive), i.e., the along-channel flow is in thermal wind balance with the lateral density gradient. This balance is disrupted by the wind forcing, particularly during the up-estuary wind. The down-estuary wind amplifies the two-layer gravitational circulation so that $\overline{f\frac{\partial u}{\partial z}}$ doubles (Fig. 5b). In contrast, the up-estuary wind generates a two-layer baroclinic current that opposes the gravitational circulation. The shear in the along-channel current is negative initially but turns to be positive as the up-estuary wind reverses the gravitational circulation (landward in the upper layer and seaward in the lower layer). Consequently $\overline{f\frac{\partial u}{\partial z}}$ is initially negative but becomes positive later (Fig. 5d). It should be noted that $\overline{f\frac{\partial u}{\partial z}}$ shows much larger departure from its pre-wind value during the up-estuary wind than during the down-estuary wind. While the conversion of planetary vorticity acts as a source for ω_x, the turbulent diffusion acts as a sink to spin down ω_x. The two terms are nearly 180^o out of phase during the wind event. Due to the lateral straining of isopycnals, the eddy

viscosity is 1.2×10^{-3} m^2s^{-1}, about 37% smaller than 1.9×10^{-3} m^2s^{-1} during down-estuary wind. However, the vertical gradient of ω_x is much larger during the up-estuary wind. The net result is that the turbulent diffusion of ω_x is much stronger during the up-estuary wind than during the down-estuary wind. As shown in Fig. 5, the time series of the volume-averaged diffusion appears to be a mirror image of the perturbation of $\overline{f\frac{\partial u}{\partial z}}$ from its pre-wind value. This reveals a counter-balance between the vorticity generation due to the conversion of the planetary vorticity and the vorticity destruction due to the turbulent diffusion. In comparison to the two terms, the nonlinear advection term is small enough to be neglected (Fig. 5b and 5d).

The baroclinic forcing is elevated during the down-estuary wind since the counterclockwise circulation tilts the isopycnals towards the vertical direction and amplifies $\overline{-g\beta\frac{\partial S}{\partial y}}$. A more dramatic effect is noted during the up-estuary wind when $\overline{-g\beta\frac{\partial S}{\partial y}}$ initially helps to generate the clockwise lateral circulation but reduces to near zero values as the isopycnals slump back to horizontal equilibrium positions. During the second half of the up-estuary wind event, continual upwelling on the western shoal lifts high salinity bottom water to the surface and creates a negative baroclinic forcing, but $\overline{-g\beta\frac{\partial S}{\partial y}}$ is relatively weak since the isopycnals are widely spaced (see Fig. 3i).

The feedback mechanisms between the baroclinicity and lateral Ekman flows are different under the down- and up-estuary winds. When the estuary is forced by the down-estuary wind, the vertical shear in the along-channel current results in a negative vorticity ($f\frac{\partial u}{\partial z}<0$), but the counterclockwise lateral circulation steepens the isopycnals, leading to a positive vorticity ($-g\beta\frac{\partial S}{\partial y}>0$). A negative feedback thus exists to weaken the lateral circulation. When the estuary is forced by the up-estuary wind, however, the along-channel shear is reversed so that the positive streamwise vorticity ($f\frac{\partial u}{\partial z}>0$) is produced. During the first half of the wind event, the baroclinic forcing $-g\beta\frac{\partial S}{\partial y}>0$ contributes to the generation of the positive streamwise vorticity but weakens as the isopycnals are flattened. Further straining of the density field by the clockwise circulation leads to a weak baroclinic forcing $-g\beta\frac{\partial S}{\partial y}<0$ that opposes $f\frac{\partial u}{\partial z}>0$. When integrated over the whole wind event, the baroclinic forcing is positive under both the down- and up-estuary winds, and contributes to the generation of positive streamwise vorticity and clockwise lateral circulation.

4. Effects on the along-channel flow

In tidally driven estuaries, recent studies have shown that nonlinear advection by lateral flows is of the first order of importance in the subtidal along-channel

momentum balance and acts as a driving force for the estuarine exchange flows [*Lerczak and Geyer*, 2004; *Scully et al.*, 2009]. In this section we investigate how the wind-driven lateral circulation affects the along-channel flow.

Figure 6 shows a comparison of the along-channel and cross-channel velocities among three runs: (1) down-estuary wind; (2) no-wind; (3) up-estuary wind. Without wind forcing, the estuary is characterized by a two-layer residual gravitational circulation with speeds reaching 0.1 m s^{-1}, as shown in the along-channel distribution of the along-channel velocity (Fig. 6b). The lateral flows are weak and generated by the interaction between moderate tidal currents and density field (Fig. 6e). When the down-estuary wind is applied over the Bay, it drives a seaward-directed current in the upper layer and a return flow in the lower layer, thus amplifying the gravitational circulation in the along-channel section (Fig. 6a). A counterclockwise lateral circulation develops in the cross-channel section (Fig. 6d). When the wind blows up-estuary, it drives a two-layer circulation that opposes the gravitational circulation (Fig. 6c). At the peak wind, the wind-driven circulation nearly cancels the gravitational circulation so that the along-channel flows are weak. In the meantime, a strong clockwise lateral circulation develops in the cross-channel section, with speeds comparable to the along-channel currents (Fig. 6f).

To determine if the lateral circulation affects the along-channel flow, we conduct a diagnostic analysis of the along-channel momentum equation (Eq. 9), as shown in Fig. 7. Both the down-estuary and up-estuary cases are considered and the time slice is

selected at 12 hour into the wind event. The stress divergence $\frac{\partial}{\partial z}\left(K_V \frac{\partial u}{\partial z}\right)$ and longitudinal pressure gradient $-\frac{1}{\rho}\frac{\partial P}{\partial x}$ are two leading terms in the momentum equation. It is interesting to note that the Coriolis force fv exhibits a two-layer structure over the cross-channel section. Under the down-estuary wind, the stress divergence overcomes the pressure gradient to drive a downwind flow in the upper layer. In the lower layer, the pressure gradient overpowers the stress divergence to drive an upwind flow (Figs. 7a and 7c). The Coriolis acceleration fv has the opposite sign to the stress divergence in the upper layer and the opposite sign to the pressure gradient in the lower layer (Fig. 7e). Hence it weakens the downwind current in the upper layer and the upwind current in the lower layer, thereby reducing the shear in the along-channel current. The same result applies to the up-estuary wind (Figs. 7b, 7d, and 7f). Figure 8 is a schematic diagram that illustrates how the Coriolis acceleration on the lateral flows weakens the shear in the along-channel currents under both down- and up-estuary winds.

The nonlinear advection term $-\left(u\frac{\partial u}{\partial x}+v\frac{\partial u}{\partial y}+w\frac{\partial u}{\partial z}\right)$ shows complex spatial patterns due to flow-topography interactions but is generally smaller than the Coriolis term (Figs. 7g and 7h). It has no obvious correlation with other terms in the momentum equation. Although the nonlinear advection by tidally driven lateral circulation has been found to play a significant role in driving the along-channel

estuarine exchange flows, we find that the nonlinear advection by wind-driven lateral circulation does not play a coherent role in driving the along-channel flows.

The above analysis is limited to a mid-bay cross-section at one time snapshot. In order to compare the magnitudes of each term in the along-channel momentum equation for the whole Bay, we calculate the volume-averaged quantities for the upper and lower layers. Since $\frac{\partial}{\partial z}\left(K_V \frac{\partial u}{\partial z} \right)$ switches sign at a depth of around 5 m (see Fig. 7), we define fixed volumes for the upper and lower layers by separating them at this depth. The time series of the layer-averaged terms are shown in Fig. 9. We experiment with other ways for the volume integration (e.g. chose a separation depth at 7 m) and obtain the same results.

First we study the down-estuary wind. For the upper layer, the stress divergence overcomes the along-channel pressure gradient to produce a negative value (with a maximum of -3.59×10^{-6} m s^{-2}) which drives the seaward flow. The Coriolis force acting the westward flows counteracts the stress divergence (with a maximum of 2.56×10^{-6} m s^{-2}) (Fig. 9a). The nonlinear advection also slightly opposes the stress divergence term, but does not change much with time. The local acceleration is relatively small and its sign change during the wind event is consistent with the temporal development of the along-channel current. In the lower layer, the longitudinal pressure gradient overpowers the stress divergence to generate positive value (with a maximum of 2.36×10^{-6} m s^{-2}) and landward return flow whereas $fv < 0$ (with a maximum of -1.66×10^{-6} m s^{-2}). Once again the Coriolis term associated with

the lateral flow opposes the pressure gradient that drives landward flow in the lower layer (Fig. 9b).

Under the up-estuary wind, the imbalance between $-\frac{1}{\rho}\frac{\partial P}{\partial x}$ and $\frac{\partial}{\partial z}\left(K_V \frac{\partial u}{\partial z}\right)$ is much larger, reaching a maximum of 4.20×10^{-6} m s^{-2} in the upper layer and a minimum of -4.39×10^{-6} m s^{-2} in the lower layer. Since the lateral circulation is 2-3 times stronger under the up-estuary wind, fv is much larger, reaching a minimum of -3.84×10^{-6} m s^{-2} in the surface layer and a maximum of 3.13×10^{-6} m s^{-2} in the bottom layer. The nonlinear advection term plays a smaller role in the along-channel momentum balance under the up-estuary wind, as shown in Figs. 7g and 7h.

5. Regime Diagrams

In the last two sections, we conducted detailed analysis of the lateral circulation dynamics under one representative wind stress of $|\tau_p|$=0.07 Pa (or wind speed of about 7.4 m s^{-1}). Now we investigate how the lateral circulation and along-channel current shear vary with the wind speed. Figure 10 shows the time series of the volume-averaged streamwise vorticity $\overline{\omega_x}$ for a wide range of wind stress (or speed) magnitudes. For all the winds considered, the magnitude of $\overline{\omega_x}$ is much larger during the up-estuary winds than during the down-estuary winds. Under the up-estuary winds, the peak value of $\overline{\omega_x}$ increases as the peak wind stress $|\tau_p|$ increases from

0.01 to 0.15 Pa but decreases slightly as $|\tau_p|$ increases further to 0.25 Pa. In contrast, the peak value of $\overline{\omega_x}$ only exhibits modest increases as $|\tau_p|$ increases from 0.01 to 0.25 Pa. It is worth noting that at high winds $\overline{\omega_x}$ peaks earlier and decreases more rapidly with time. An analysis of the streamwise vorticity budget (as in Fig. 5) shows that both $f\frac{\partial u}{\partial z}$ and diffusion terms reach their maxima before the peak wind speed and suggests that strong turbulent dissipation at high winds causes a rapid spin-down of the streamwise vorticity. As a result, the time average of $\overline{\omega_x}$ over the entire wind event is smaller at high winds than at intermediate wind speeds.

Following *Li and Li* [2011], we summarize the model results in terms of two dimensionless parameters: Wedderburn number *W* and Kelvin number *Ke*. *W* is defined as

$$W = \frac{\tau_W L}{\Delta\rho g H^2} \tag{10}$$

where L is the length of an estuary, $\Delta\rho$ the horizontal density difference, g the gravitational acceleration, and H the mean water depth [*Monismith*, 1986; *Geyer*, 1997; *Chen and Sanford*, 2009]. The Wedderburn number compares the wind forcing with the horizontal baroclinic pressure gradient. The Kelvin number is defined as

$$Ke = \frac{fB}{\sqrt{g' h_S}} \tag{11}$$

where f is the Coriolis parameter, B the estuary width, g' the reduced gravitational acceleration determined by the density difference between the upper and lower layers, and h_S the mean depth of the upper layer. The Kelvin number is the ratio of the estuary width to the internal Rossby radius of deformation [e.g. *Garvine*, 1995; *Valle-Levinson*, 2008]. For Chesapeake Bay, W varies from ~1 to 10 for wind speeds ranging 5 ~ 10 m s^{-1} and Ke=4.5. Although the model bathymetry is specific to Chesapeake Bay, we conduct numerical experiments by varying f over a range from 25%f to 150%f to explore estuaries of different widths. Table 1 summarizes all the numerical runs we have conducted.

Figure 11 shows how the time average of the streamwise vorticity $\langle \overline{\omega}_x \rangle$ over the entire wind event varies with the Wedderburn and Kelvin numbers. $\langle \overline{\omega}_x \rangle > 0$ (clockwise circulation) is for the up-estuary winds and $\langle \overline{\omega}_x \rangle < 0$ (counter-clockwise circulation) is for the down-estuary winds. At a given value of Ke, $\langle \overline{\omega}_x \rangle$ increases rapidly with increasing $|W|$ at small values of $|W|$: the lateral circulation becomes stronger as the wind forcing gets stronger. $\langle \overline{\omega}_x \rangle$ reaches a maximum value at an intermediate value of $|W|$. At larger $|W|$, $\langle \overline{\omega}_x \rangle$ decreases since the strong dissipation at high wind speeds causes a more rapid spin-down of the streamwise vorticity. As the lateral circulation is primarily driven by the wind-induced Ekman transport, it is

not surprising that $\langle \overline{\omega}_x \rangle$ increases with increasing *Ke*: the lateral circulation is stronger at higher latitudes or in wider estuaries. It is important to note the asymmetry in $\langle \overline{\omega}_x \rangle$ between the down- and up-estuary winds. At *Ke*=4.5 (at the latitude of Chesapeake Bay), $\langle \overline{\omega}_x \rangle$ generated by the up-estuary winds is 2 times as large as that generated by the down-estuary winds.

To better understand the variation of $\langle \overline{\omega}_x \rangle$ with *W* and *Ke*, we conduct a diagnostic analysis of the streamwise vorticity budget for all the model runs and plot the three leading terms in Fig. 12. We average the terms over the entire wind event to show the integrated effects. The conversion of planetary vorticity by the along-channel current $\left\langle \overline{f \frac{\partial u}{\partial z}} \right\rangle$ increases with both $|W|$ and *Ke*. As expected, the generation of the streamwise vorticity is stronger in a strongly rotating system or at higher winds. The turbulent diffusion acts in direct opposition to $\left\langle \overline{f \frac{\partial u}{\partial z}} \right\rangle$ and shows similar variation with $|W|$ and *Ke*. While the conversion of the planetary vorticity *f* tends to generate the lateral torque, the turbulent diffusion term tends to spin it down. The time-averaged baroclinic forcing term is positive during both the down-estuary and up-estuary wind events. However, it is much larger during the down-estuary winds. This difference in the baroclinic forcing $\left\langle \overline{-g\beta \frac{\partial S}{\partial y}} \right\rangle$ is the main cause for the asymmetry in the strength of the lateral circulation between the down- and up-estuary

winds. It is interesting to note that $\left\langle \overline{-g\beta \frac{\partial S}{\partial y}} \right\rangle$ approaches to constant (saturating) values at large values of $|W|$ for a given value of *Ke*. The lateral straining can only tilt the isopycnals towards the vertical directions and the lateral salinity gradient cannot increase further at higher wind speeds.

In Fig. 13 we examine how the time average of the along-channel current $\left\langle \overline{\frac{\partial u}{\partial z}} \right\rangle$ over the entire wind event varies with *W* and *Ke*. *Ke*=0 corresponds to the non-rotating runs. At *W*=0 the along-channel shear is generated by the gravitational circulation and is negative. The down-estuary winds amplify this shear. The up-estuary winds generate a two-layer baroclinic current which opposes the gravitational circulation. At low wind speeds, $\left\langle \overline{\frac{\partial u}{\partial z}} \right\rangle$ remains to be negative but turns to be positive (as the wind-driven circulation reverses the gravitational circulation) when *W* exceeds a threshold value. Compared with the rotating runs at the same value of *W*, the shear in the along-channel current is strongest in the non-rotating runs. As discussed in section 4, the Coriolis force acting on the lateral flows reduces the shear in the along-channel current. At *Ke* = 4.5 (the latitude of Chesapeake Bay), $\left\langle \overline{\frac{\partial u}{\partial z}} \right\rangle$ is about 30-40% smaller than that in runs in which the effects of the earth's rotation are not considered. The reduction in the along-channel shear is higher at higher latitudes and wide estuaries (larger values of *Ke*) but lower at lower latitudes and narrow estuaries.

6. Conclusions

Using a numerical model of Chesapeake Bay, we have investigated the dynamics of wind-driven lateral and along-channel currents in a stratified rotating estuary. The Ekman transport associated with the along-channel winds generates a counterclockwise lateral circulation under the down-estuary winds and a clockwise lateral circulation under the up-estuary winds. However, the strength of the lateral circulation is about 2 times stronger during the up-estuary winds than during the down-estuary winds. To understand what causes this asymmetry, we have developed a new approach by conducting diagnostic analysis of the streamwise vorticity equation. It reveals a primary balance among three leading terms: the conversion of the planetary vorticity by the shear in the along-channel current, the baroclinic forcing due to sloping isopycnals at cross-channel sections, and turbulent diffusion. Although the turbulent diffusion always acts to spin down the vorticity generated by the conversion of the planetary vorticity, the baroclinic forcing is highly asymmetric between the down- and up-estuary winds. The counterclockwise lateral circulation generated by the down-estuary winds tilts the isopycnals towards the vertical directions and creates adverse lateral barolinic pressure gradient to hamper the lateral Ekman transport. In contrast, the clockwise lateral circulation generated by the up-estuary winds initially flattens the isopycnals and the baroclinic forcing reinforces the lateral Ekman transport.

The analysis based on the streamwise vorticity could be extended to study lateral circulations in tidally forced estuaries. In the streamwise vorticity equation, the two-

cell lateral circulation generated by differential advection can be described by the baroclinic forcing term $-g\beta\frac{\partial S}{\partial y}$ due to the lateral density gradient while the one-cell lateral circulation generated by the tidal rectification of lateral Ekman flow can be described by the conversion of the planetary vorticity by the shear in the tidal current $f\frac{\partial u}{\partial z}$. An outstanding question is how the two mechanisms contribute to the generation of the lateral circulations in estuaries of different widths and under different river discharge and tidal forcing conditions.

Previous studies of lateral circulations in narrow estuaries have shown that the nonlinear advection $-\left(u\frac{\partial u}{\partial x}+v\frac{\partial u}{\partial y}+w\frac{\partial u}{\partial z}\right)$ associated with the lateral flows works in concert with the along-channel baroclinic pressure gradient to amplify the estuarine exchange flows. In a wide estuary such as Chesapeake Bay, however, we have found that the Coriolis acceleration fv associated with the lateral flows reduces the shear in the along-channel currents. Compared with the non-rotating system, the shear reduction is about 30-40%. Future work is needed to examine the relative roles of the nonlinear advection and Coriolis acceleration in both tidally- and wind-driven flows and for estuaries of different widths. In an effort to generalize the model results specific to Chesapeake Bay, we have conducted model runs by varying the Coriolis parameter *f*. Regime diagrams have been constructed to show how the averaged streamwise vorticity and along-channel current shear vary with the Wedderburn (*W*) and Kelvin (*Ke*) numbers. In the future we plan to conduct model runs of an idealized

generic estuary and examine how the lateral circulation and along-channel exchange flow vary in the nondimensional parameter space.

The results presented in this chapter are based on the outputs from a numerical model. Although this model has been validated against the observational data, there are to our knowledge no existing data with adequate temporal and spatial resolution to resolve the full three-dimensional structure of flow and density fields. Given the physical and ecological importance of the lateral circulations, especially for long estuary with wide channels, future observational study of the wind effects on lateral circulations is warranted.

Acknowledgements: We thank Bill Boicourt, Malcolm Scully and Peng Jia for helpful discussions. We are grateful to NSF (OCE-082543 and OCE-0961880) and NOAA (CHRP-NA07N054780191) for the financial support. This is UMCES contribution number 4682 and CHRP contribution number 168.

Appendix A. Decomposition of vectors into along- and cross-channel directions

We choose the along-channel direction to be aligned with the semi-major axis of the depth-averaged tidal current ellipse associated with the dominant tidal harmonics M_2. It is positive when pointing into the estuary. The cross-channel direction is defined to be at 90 degree to the along-channel direction. At each model grid point, the along- and cross-channel components of the horizontal velocity vector are calculated using the following formulae

$$\widetilde{u} = u_{\mathrm{R}} \cos\theta + v_{\mathrm{R}} \sin\theta \tag{A1}$$

$$\widetilde{v} = -u_{\mathrm{R}} \sin\theta + v_{\mathrm{R}} \cos\theta \tag{A2}$$

where $(\widetilde{u},\widetilde{v})$ are the velocity components in the along- and cross-channel directions $(\widetilde{x},\widetilde{y})$, (u_R, v_R) are the velocity components in the (ξ, η) directions defined in the ROMS model, and θ is the angle between the along-channel direction and the ξ-direction.

To project the momentum equations into the along- and cross-channel directions, we treat each term in the momentum equation as a vector with components in the (ξ, η) directions and then apply the same decomposition as (A1)-(A2). If (ξ, η) are curvilinear coordinates, terms in the momentum equations involve coefficients related

to the coordinate transformation [*Haidvogel et al*, 2000], but the projection into the along- and cross-channel directions can be treated in the same way.

Appendix B. Calculation of streamwise vorticity

In the Cartesian coordinate, the cross-channel momentum equation is given by

$$\frac{\partial v}{\partial t} = -fu - \frac{1}{\rho}\frac{\partial P}{\partial y} - \left(u\frac{\partial v}{\partial x} + v\frac{\partial v}{\partial y} + w\frac{\partial v}{\partial z} \right) + \frac{\partial}{\partial z}\left(K_V \frac{\partial v}{\partial z} \right) + \frac{\partial}{\partial x}\left(K_H \frac{\partial v}{\partial x} \right) + \frac{\partial}{\partial y}\left(K_H \frac{\partial v}{\partial y} \right) \tag{B1}$$

where (u, v, w) are the velocity components in the along-channel, cross-channel and vertical directions, f the Coriolis parameter, P the total pressure, and K_v and K_H are the vertical and horizontal eddy viscosities. As shown in Section 2, taking -∂/∂z of Eq. (B1) yields the equation for the streamwise vorticity.

In the ROMS model, the equations of motions are solved in a transformed coordinate system which has a generalized topography-following σ coordinate in the vertical direction and orthogonal curvilinear (ξ, η) coordinates in the horizontal directions [*Haidvogel et al.*, 2000]. After the decomposition into the along- and cross-channel directions $(\tilde{x}, \tilde{y})$, the cross-channel momentum equation in the transformed coordinates can be written as

$$\overbrace{\frac{\partial \tilde{v}}{\partial t}}^{\text{accel}} = \overbrace{-f\tilde{u}}^{\text{cor}} + \overbrace{\left(-\frac{1}{\rho}\frac{\partial P}{\partial \tilde{y}} - \frac{g\rho}{\rho_0}\frac{\partial z}{\partial \tilde{y}} \right)}^{\text{prsgrd}} + \overbrace{\left(-\frac{\partial \tilde{u}\tilde{v}}{\partial \tilde{x}} - \frac{\partial \tilde{v}\tilde{v}}{\partial \tilde{y}} + CT \right)}^{\text{hadv}} + \overbrace{\left(-\frac{1}{H_Z}\frac{\partial H_Z \tilde{v}\Omega}{\partial \sigma} \right)}^{\text{vadv}} + \underbrace{\frac{1}{H_Z}\frac{\partial}{\partial \sigma}\left(\frac{K_V}{H_Z}\frac{\partial \tilde{v}}{\partial \sigma} \right)}_{\text{vvisc}} + \underbrace{\tilde{D}_v}_{\text{hvisc}} \tag{B2}$$

in which the curvilinear transformation term (*CT*) is given by

$$
\begin{aligned}
CT = & \frac{H_Z \widetilde{u}\widetilde{v}}{mn}\frac{\partial}{\partial \widetilde{x}}\left(\frac{mn}{H_Z}\right)+\frac{H_Z \widetilde{v}\widetilde{v}}{mn}\frac{\partial}{\partial \widetilde{y}}\left(\frac{mn}{H_Z}\right) \\
& + m(\widetilde{u}\sin\theta+\widetilde{v}\cos\theta)(\widetilde{u}\cos\theta-\widetilde{v}\sin\theta)\frac{\partial}{\partial \widetilde{x}}\left(\frac{1}{m}\right)+m(\widetilde{u}\cos\theta-\widetilde{v}\sin\theta)^2\frac{\partial}{\partial \widetilde{y}}\left(\frac{1}{m}\right) \\
& - n(\widetilde{u}\sin\theta+\widetilde{v}\cos\theta)(\widetilde{u}\cos\theta-\widetilde{v}\sin\theta)\frac{\partial}{\partial \widetilde{x}}\left(\frac{1}{n}\right)+n(\widetilde{u}\sin\theta+\widetilde{v}\cos\theta)^2\frac{\partial}{\partial \widetilde{y}}\left(\frac{1}{n}\right).
\end{aligned}
\tag{B3}
$$

Here $(\widetilde{u},\widetilde{v})$ are the velocity components in the along- and cross-channel directions, Ω is the velocity component in the σ-direction, m and n are the scale factors that relate the differential distances in ξ-η grid to the actual (physical) arc lengths, $H_z = \partial z/\partial\sigma$, and $\widetilde{D}_v$ represents the horizontal viscosity terms. All the terms in the two horizontal momentum equations are calculated in the diagnostics package provided by ROMS. They can be combined to yield the terms in the along- and cross-channel momentum equations using the decomposition method described in Appendix A.

To obtain the equation for the streamwise vorticity, we take the vertical derivative of Eq. (B2) and make use of $\frac{\partial}{\partial z}=\frac{1}{H_Z}\frac{\partial}{\partial\sigma}$. In the transformed coordinate system, the streamwise vorticity is given by

$$
\omega_x = -\frac{1}{H_Z}\frac{\partial \widetilde{v}}{\partial\sigma} \tag{B4}
$$

and the equation of the streamwise vorticity becomes

$$\frac{\partial \omega_x}{\partial t} = \overbrace{\frac{f}{H_Z}\frac{\partial \tilde{u}}{\partial \sigma}}^{\substack{\text{conversion of} \\ \text{planetary vorticity}}} + \overbrace{\frac{1}{H_Z}\frac{\partial}{\partial \sigma}\left(\frac{1}{\rho}\frac{\partial P}{\partial \tilde{y}} + \frac{g\rho}{\rho_0}\frac{\partial z}{\partial \tilde{y}}\right)}^{\text{baroclinicity}} + \overbrace{\frac{1}{H_Z}\frac{\partial}{\partial \sigma}\left(\frac{\partial \tilde{u}\tilde{v}}{\partial \tilde{x}} + \frac{\partial \tilde{v}\tilde{v}}{\partial \tilde{y}} - \mathrm{C}T + \frac{1}{H_Z}\frac{\partial (H_Z \tilde{v}\Omega)}{\partial \sigma}\right)}^{\text{nonlinear advection}} - \overbrace{\frac{1}{H_Z^2}\frac{\partial^2}{\partial \sigma^2}\left(\frac{K_V}{H_Z}\frac{\partial \tilde{v}}{\partial \sigma}\right)}^{\substack{\text{vertical} \\ \text{diffusion}}} \overbrace{-\frac{1}{H_Z}\frac{\partial \tilde{D}_v}{\partial \sigma}}^{\substack{\text{horizontal} \\ \text{diffusion}}} \tag{B5}$$

The nonlinear advection term is zero if the variation in along-channel direction is zero, as assumed in the derivation of Eq. (8). In all the model runs considered in this chapter, the nonlinear advection term and horizontal diffusion terms are much smaller than the other terms in the streamwise vorticity equation.

In this chapter we integrate Eq. (B5) over a control volume to examine the overall balance in the streamwise vorticity equation. The volume integration is defined as

$$\overline{\omega}_x = \frac{\iint_A \overline{\omega}_x^{\,depth} dA}{\iint_A dA} \tag{B6}$$

where $\overline{\omega_x}^{depth} = \frac{\int_{-h}^{\varsigma} \omega_x dz}{\int_{-h}^{\varsigma} dz}$ and A is the surface area of the selected region.

References

Burchard, H., R. D. Hetland, E. Schulz, and H. M. Schuttelaars (2011), Drivers of Residual Estuarine Circulation in Tidally Energetic Estuaries: Straight and Irrotational Channels with Parabolic Cross Section, *J. Phys. Oceanogr.*, *41*(3), 548-570， doi: 10.1175/2010JPO4453.1

Burchard, H., and H. M. Schuttelaars (2012), Analysis of tidal straining as driver for estuarine circulation in well mixed estuaries, *J. Phys. Oceanogr.*, *42*, 261-271, doi: 10.1175/JPO-D-11-0110.1.

Chant, R. J. (2002), Secondary circulation in a region of flow curvature: Relationship with tidal forcing and river discharge, *J. Geophys. Res.*, *107*(3131), 207-223, doi: 10.1029/2001JC001082

Chen, S.-N., and L. P. Sanford (2009), Axial wind effects on stratification and longitudinal salt transport in an idealized, partially mixed estuary, *J. Phys. Oceanogr.*, *39*(8), 1905-1920, doi: 10.1175/2009JPO4016.1.

Chen, S.-N., L. P. Sanford, and D. K. Ralston (2009), Lateral circulation and sediment transport driven by axial winds in an idealized, partially mixed estuary, *J. Geophys. Res.*, *114*, C12006, doi: 10.1029/2008JC005014.

Cheng, P., R. E. Wilson, R. J. Chant, D. C. Fugate, and R. D. Flood (2009), Modeling influence of stratification on lateral circulation in a stratified estuary, *J. Phys. Oceanogr.*, *39*(9), 2324-2337, doi: 10.1175/2009JPO4157.1.

Csanady, G. T. (1973), Wind-induced barotropic motions in long lakes, *J. Phys. Oceanogr.*, *3*(4), 429-438, doi: 10.1175/1520-0485(1973)003<0429:WIBMIL>2.0.CO;2.

Friedrichs, C. T., and J. M. Hamrick (1996), Effects of channel geometry on cross sectional variations in along channel velocity in partially stratified estuaries, *Buoyancy Effects on Coastal and Estuarine Dynamics*, *53*, 283–300.

Garvine, R. W. (1985), A simple-model of estuarine subtidal fluctuations forced by local and remote wind stress, *J. Geophys. Res.*, *90*(C6), 1945-1948, doi: 10.1029/JC090iC06p11945.

Garvine, R. W. (1995), A dynamical system for classifying buoyant coastal discharges, *Cont. Shelf Res.*, *15*(13), 1585-1596, doi: 10.1016/0278-4343(94)00065-U.

Geyer, W. R. (1997), Influence of wind on dynamics and flushing of shallow estuaries, *Estuarine Coastal Shelf Sci.*, *44*(6), 713-722, doi: doi:10.1006/ecss.1996.0140.

Geyer, W. R., J. D. Woodruff, and P. Traykovski (2001), Sediment transport and trapping in the Hudson River estuary, *Estuaries Coasts*, *24*(5), 670-679, doi: 10.2307/1352875.

Guo, X. Y., and A. Valle-Levinson (2008), Wind effects on the lateral structure of density-driven circulation in Chesapeake Bay, *Cont. Shelf Res.*, *28*(17), 2450-2471, doi: 10.1016/j.csr.2008.06.008.

Haidvogel, D. B., H. G. Arango, K. Hedstrom, A. Beckmann, P. Malanotte-Rizzoli, and A. F. Shchepetkin (2000), Model evaluation experiments in the North Atlantic Basin: simulations in nonlinear terrain-following coordinates, *Dynam. Atmos. Oceans*, *32*(3), 239-281, doi: 10.1016/S0377-0265(00)00049-X.

Huijts, K., H. Schuttelaars, H. De Swart, and C. Friedrichs (2009), Analytical study of the transverse distribution of along-channel and transverse residual flows in tidal estuaries, *Cont. Shelf Res.*, *29*(1), 89-100, doi: 10.1016/j.csr.2007.09.007.

Janzen, C. D., and K. C. Wong (2002), Wind-forced dynamics at the estuary-shelf interface of a large coastal plain estuary, *J. Geophys. Res.*, *107*(C10), 3138, doi: 10.1029/2001jc000959.

Kundu, P. K., and I. M. Cohen (2004), *Fluid Mechanics, 3rd Edition*, 759 pp., Elsevier Academic Press, San Diego, Calif.

Lacy, J. R., M. T. Stacey, J. R. Burau, and S. G. Monismith (2003), Interaction of lateral baroclinic forcing and turbulence in an estuary, *J. Geophys. Res.*, *108*(C3), 3089, doi: 10.1029/2002JC001392.

Lerczak, J. A., and W. R. Geyer (2004), Modeling the lateral circulation in straight, stratified estuaries, *J. Phys. Oceanogr.*, *34*(6), 1410-1428, doi: 10.1175/1520-0485(2004)034<1410:MTLCIS>2.0.CO;2.

Li, M., and L. J. Zhong (2009), Flood-ebb and spring-neap variations of mixing, stratification and circulation in Chesapeake Bay, *Cont. Shelf Res.*, *29*(1), 4-14, doi: 10.1016/j.csr.2007.06.012.

Li, M., L. Zhong, and W. C. Boicourt (2005), Simulations of Chesapeake Bay estuary: Sensitivity to turbulence mixing parameterizations and comparison with observations, *J. Geophys. Res.*, *110*, C12004, doi: 10.1029/2004JC002585.

Li, M., L. Zhong, W. C. Boicourt, S. L. Zhang, and D. L. Zhang (2007), Hurricane-induced destratification and restratification in a partially-mixed estuary, *J. Mar. Res.*, *65*(2), 169-192.

Li, Y., and M. Li (2011), Effects of winds on stratification and circulation in a partially mixed estuary, *J. Geophys. Res.*, *116*, C12012, doi: 10.1029/2010JC006893.

Malone, T. C., W. M. Kemp, H. W. Ducklow, W. R. Boynton, J. H. Tuttle, and R. B. Jonas (1986), Lateral variation in the production and fate of phytoplankton in a partially stratified estuary, *Mar. Ecol. Prog. Ser.*, *32*(2-3), 149-160, doi: 10.3354/meps032149.

Marchesiello, P., J. McWilliams, and A. Shchepetkin (2001), Open boundary conditions for long-term integration of regional oceanic models, *Ocean Modell.*, *3*(1), 20, doi: 10.1016/S1463-5003(00)00013-5.

Monismith, S. (1986), An experimental-study of the upwelling response of stratified reservoirs to surface shear-stress, *J. Fluid Mech.*, *171*, 407-439, doi: 10.1017/S0022112086001507.

Nunes, R., and J. Simpson (1985), Axial convergence in a well-mixed estuary, *Estuarine Coastal Shelf Sci.*, *20*(5), 637-649, doi: 10.1016/0272-7714(85)90112-X.

Reyes-Hernández, C., and A. Valle-Levinson (2010), Wind modifications to density-driven flows in semienclosed, rotating basins, *J. Phys. Oceanogr.*, *40*, 1473-1487, doi: 10.1175/2010JPO4230.1

Reynolds-Fleming, J. V., and R. A. Luettich (2004), Wind-driven lateral variability in a partially mixed estuary, *Estuarine Coastal Shelf Sci.*, *60*(3), 395-407, doi: 10.1016/j.ecss.2004.02.003.

Sanford, L. P., K. G. Sellner, and D. L. Breitburg (1990), Covariability of dissolved-oxygen with physical processes in the summertime Chesapeake Bay, *J. Mar. Res.*, *48*(3), 567-590.

Scully, M. E. (2010), Wind modulation of dissolved oxygen in Chesapeake Bay, *Estuaries Coasts*, *33*(5), 1164-1175, doi: 10.1007/s12237-010-9319-9.

Scully, M. E., W. R. Geyer, and J. A. Lerczak (2009), The influence of lateral advection on the residual estuarine circulation: A numerical modeling study of the Hudson River estuary, *J. Phys. Oceanogr.*, *39*(1), 107-124, doi: 10.1175/2008jpo3952.1.

Valle-Levinson, A. (2008), Density-driven exchange flow in terms of the Kelvin and Ekman numbers, *J. Geophys. Res.*, *113*(C4), C04001, doi: 10.1029/2007jc004144.

Wang, D. P. (1979), Wind-driven circulation in the Chesapeake Bay, winter 1975, *J. Phys. Oceanogr.*, *9*(3), 564-572, doi: 10.1175/1520-0485(1979)009<0564:WDCITC>2.0.CO;2.

Warner, J. C., W. R. Geyer, and J. A. Lerczak (2005), Numerical modeling of an estuary: A comprehensive skill assessment, *J. Geophys. Res.*, *110*, C05001, doi: 10.1029/2004JC002691.

Weisberg, R. H., and W. Sturges (1976), Velocity Observations in West Passage of Narragansett Bay - Partially Mixed Estuary, *J. Phys. Oceanogr.*, *6*(3), 345-354, doi: 10.1175/1520-0485(1976)006<0345:VOITWP>2.0.CO;2.

Wilson, R. E., R. L. Swanson, and H. A. Crowley (2008), Perspectives on long-term variations in hypoxic conditions in western Long Island Sound, *J. Geophys. Res.*, *113*, C12011, doi: 10.1029/2007JC004693.

Winant, C. (2004), Three-dimensional wind-driven flow in an elongated, rotating basin, *J. Phys. Oceanogr.*, *34*(2), 462-476, doi: 10.1175/1520-0485(2004)034<0462: TWFIAE>2.0.CO;2.

Wong, K. C. (1994), On the nature of transverse variability in a coastal-plain estuary, *J. Geophys. Res.*, *99*(C7), 14209-14222, doi: 10.1029/94JC00861.

Zhong, L., and M. Li (2006), Tidal energy fluxes and dissipation in the Chesapeake Bay, *Cont. Shelf Res.*, *26*(6), 752-770, doi: 10.1016/j.csr.2006.02.006.

Zhong, L., M. Li, and M. G. G. Foreman (2008), Resonance and sea level variability in Chesapeake Bay, *Cont. Shelf Res.*, *28*(18), 2565-2573, doi: 10.1016/j.csr.2008.07.007.

Tables

Table 2-1. Idealized Wind Experiments. The wind is spatially uniform and a temporal half-sinusoidal function from day 25 to 27.5, with peak wind stress shown below. Kelvin number (*Ke*) is calculated using Coriolis Parameter *f* that is 0, 25, 50, 100, 125 and 150 percent of the value for Chesapeake Bay. *W* is Wedderburn number. Both numbers are defined in Section 5.

Wind Stress	Wind Speed	*Ke* = 0.00		*Ke* = 1.04		*Ke* = 2.14		*Ke* = 4.50		*Ke* = 5.45		*Ke* = 6.76	
(Pa)	(m/s)	No.	*W*	No.	*W*	No.	*W*	No.	*W*	No.	*W*	No.	*W*
						no wind							
0.00	0.00	**1**	0	**18**	0	**35**	0	**52**	0	**69**	0	**86**	0
						down-estuary wind							
-0.005	-2.35	**2**	-0.24	**19**	-0.25	**36**	-0.27	**53**	-0.26	**70**	-0.25	**87**	-0.26
-0.01	-3.20	**3**	-0.49	**20**	-0.51	**37**	-0.54	**54**	-0.52	**71**	-0.51	**88**	-0.52
-0.02	-4.34	**4**	-0.97	**21**	-1.00	**38**	-1.07	**55**	-1.06	**72**	-1.00	**89**	-1.02
-0.03	-5.17	**5**	-1.46	**22**	-1.50	**39**	-1.59	**56**	-1.57	**73**	-1.49	**90**	-1.52
-0.05	-6.41	**6**	-2.46	**23**	-2.49	**40**	-2.63	**57**	-2.64	**74**	-2.46	**91**	-2.52
-0.07	-7.37	**7**	-3.44	**24**	-3.49	**41**	-3.67	**58**	-3.71	**75**	-3.45	**92**	-3.52
-0.15	-10.03	**8**	-7.66	**25**	-7.57	**42**	-7.82	**59**	-8.02	**76**	-7.34	**93**	-7.36
-0.25	-12.27	**9**	-13.43	**26**	-13.15	**43**	-13.25	**60**	-13.42	**77**	-12.23	**94**	-12.01
						up-estuary wind							
0.005	2.35	**10**	0.26	**27**	0.26	**44**	0.27	**61**	0.26	**78**	0.25	**95**	0.26
0.01	3.20	**11**	0.52	**28**	0.53	**45**	0.56	**62**	0.53	**79**	0.51	**96**	0.53
0.02	4.34	**12**	1.04	**29**	1.08	**46**	1.13	**63**	1.09	**80**	1.03	**97**	1.08
0.03	5.17	**13**	1.56	**30**	1.65	**47**	1.72	**64**	1.65	**81**	1.54	**98**	1.64
0.05	6.41	**14**	2.56	**31**	2.85	**48**	2.98	**65**	2.74	**82**	2.61	**99**	2.78
0.07	7.37	**15**	3.57	**32**	4.04	**49**	4.34	**66**	3.93	**83**	3.73	**100**	3.90
0.15	10.03	**16**	7.45	**33**	8.39	**50**	9.56	**67**	9.77	**84**	8.69	**101**	9.12
0.25	12.27	**17**	12.32	**34**	13.61	**51**	15.49	**68**	16.74	**85**	16.14	**102**	17.36

Figures

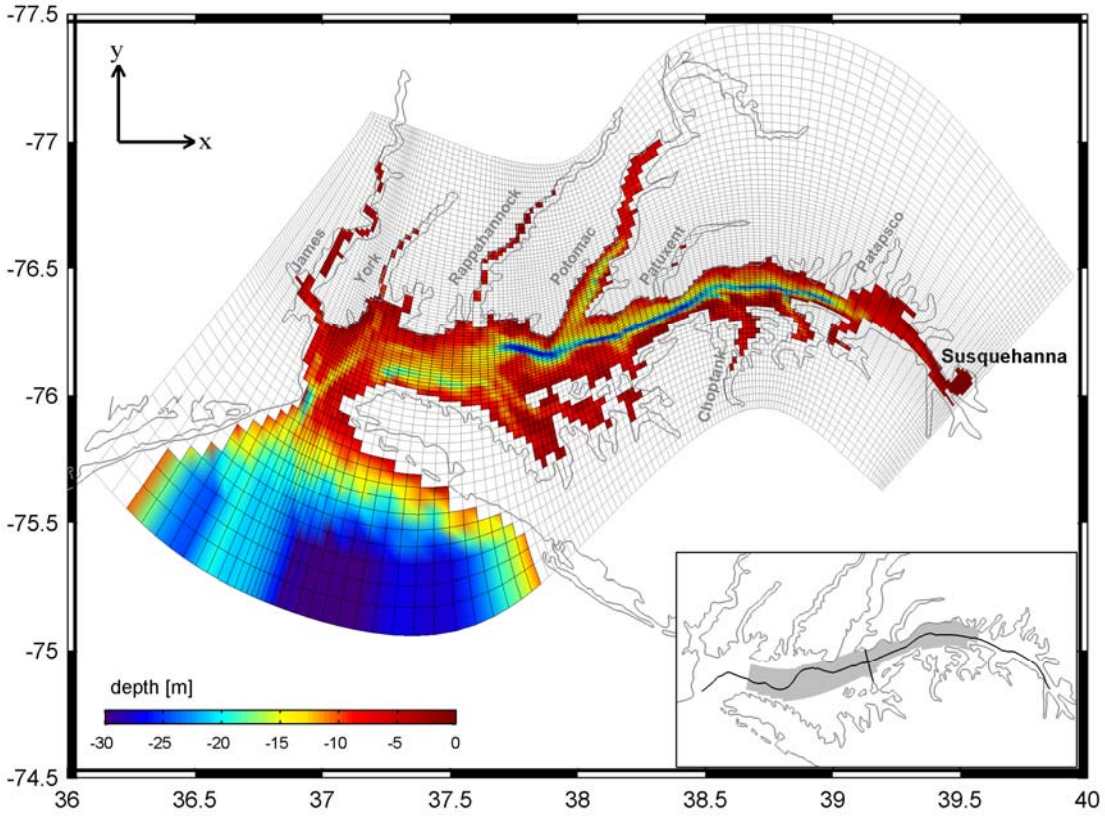

Figure 2-1. Bathymetry of Chesapeake Bay and its adjacent coastal shelf. Major tributaries are marked. Depths are in meters. The shaded areas in the insert are used for calculating volume-averaged quantities in this study. The solid lines represent the along-channel and cross-channel transects.

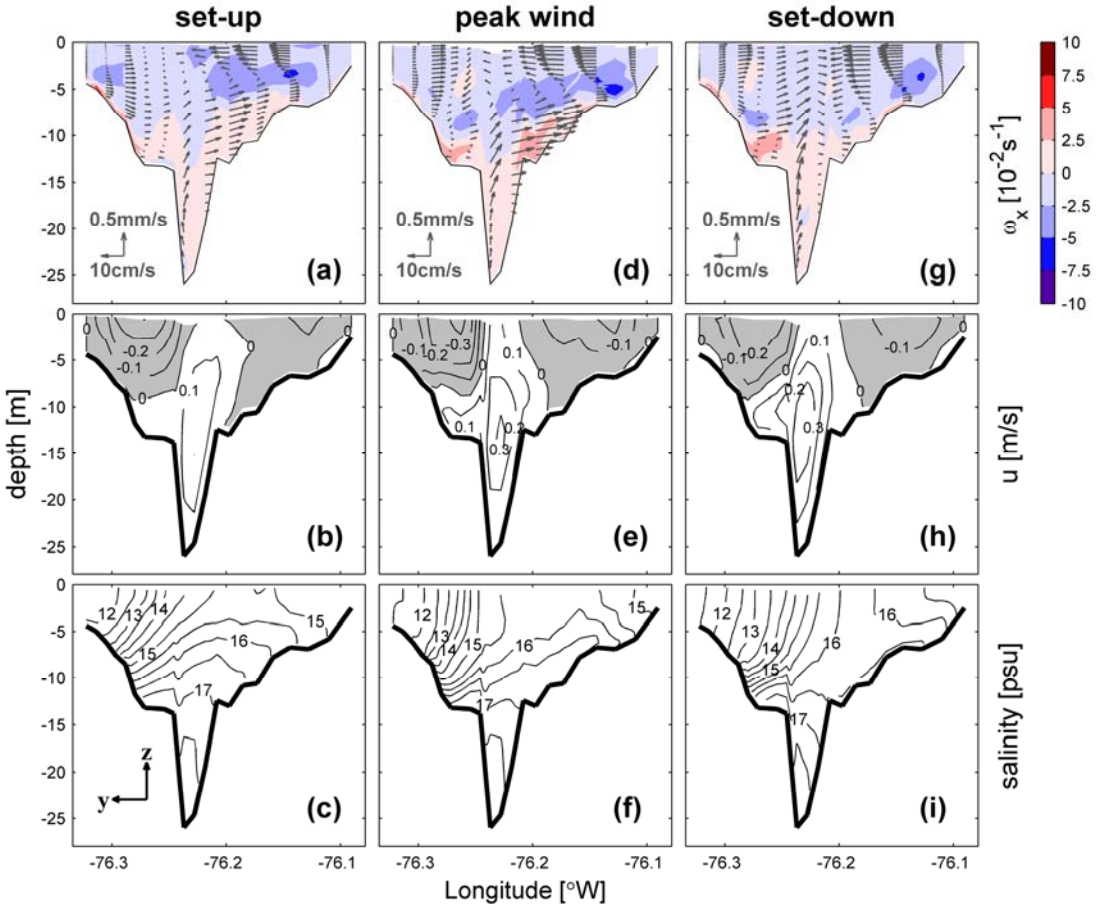

Figure 2-2. Temporal evolution of (a/d/g) the streamwise vorticity (color) and the lateral-vertical velocity vectors, (b/e/h) the along-channel velocity, and (c/f/i) salinity at a cross-channel section under the down-estuary wind with the peak wind stress of -0.07 Pa. The snapshots are taken at 12-hr into the wind event (day 25.5), peak wind (day 26.25), and 12-hr toward the end of wind (day 27). The plot is looking into estuary and the positive vorticity indicates clockwise motion.

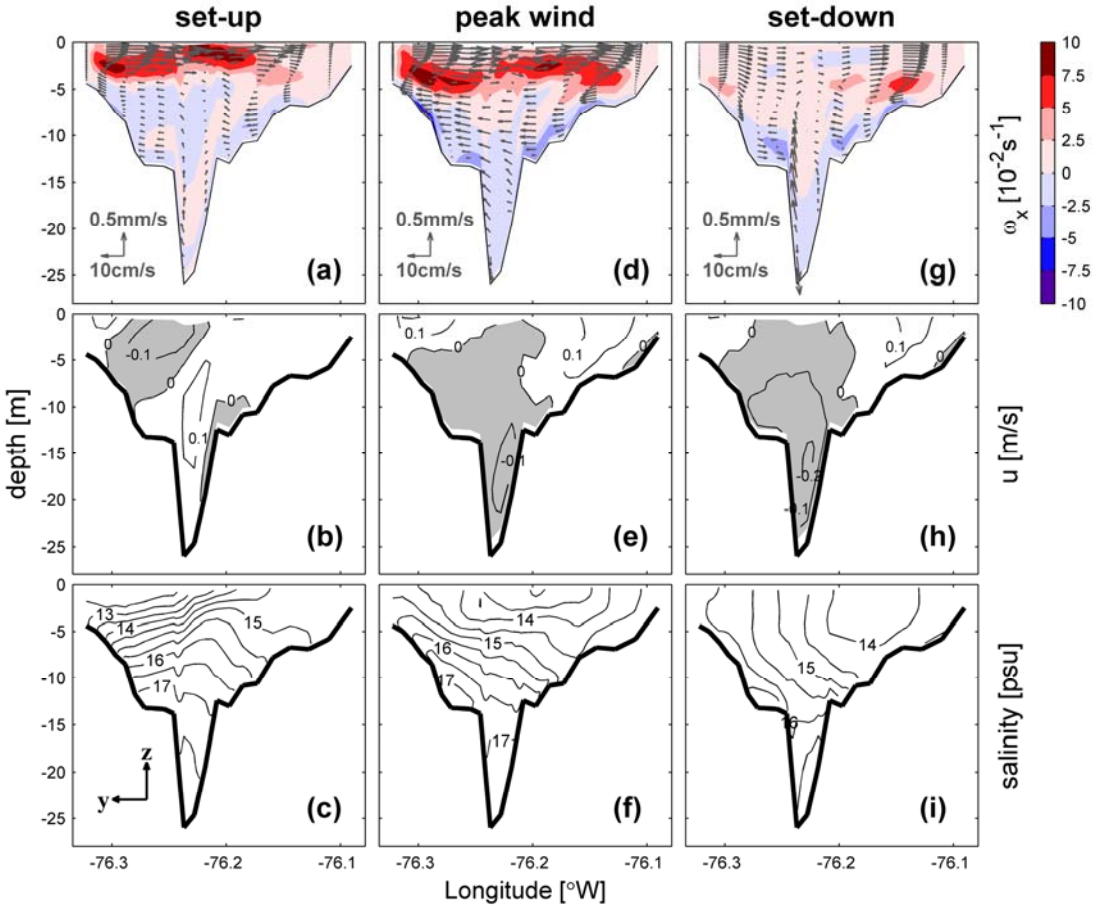

Figure 2-3. Temporal evolution of (a/d/g) the streamwise vorticity (color) and the lateral-vertical velocity vectors, (b/e/h) the along-channel velocity, and (c/f/i) salinity at a cross-channel section under the up-estuary wind with the peak wind stress of 0.07 Pa. The snapshots are taken at 12-hr into the wind event (day 25.5), peak wind (day 26.25), and 12-hr toward the end of wind (day 27). The plot is looking into estuary and the positive vorticity indicates clockwise motion.

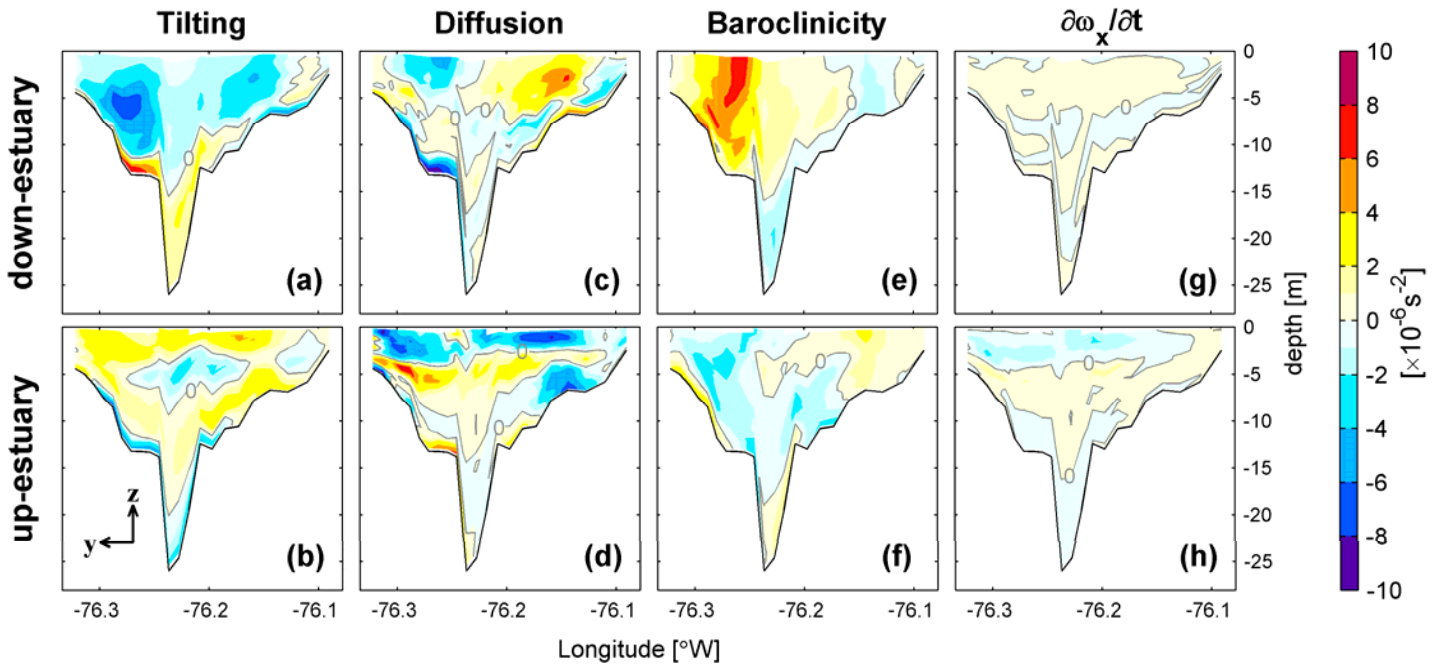

Figure 2-4. Terms in the streamwise-vorticity equation: (a/b) the conversion of planetary vorticity, (c/d) turbulent diffusion, (e/f) baroclinicity, and (g/h) time tendency under the down- and up-estuary wind with the peak magnitude of 0.07 Pa. The snapshots are taken at the peak of wind event. The cross-section is looking into estuary, and positive values indicate clockwise rotation. The unit of vorticity terms is $10^{-6}s^{-2}$

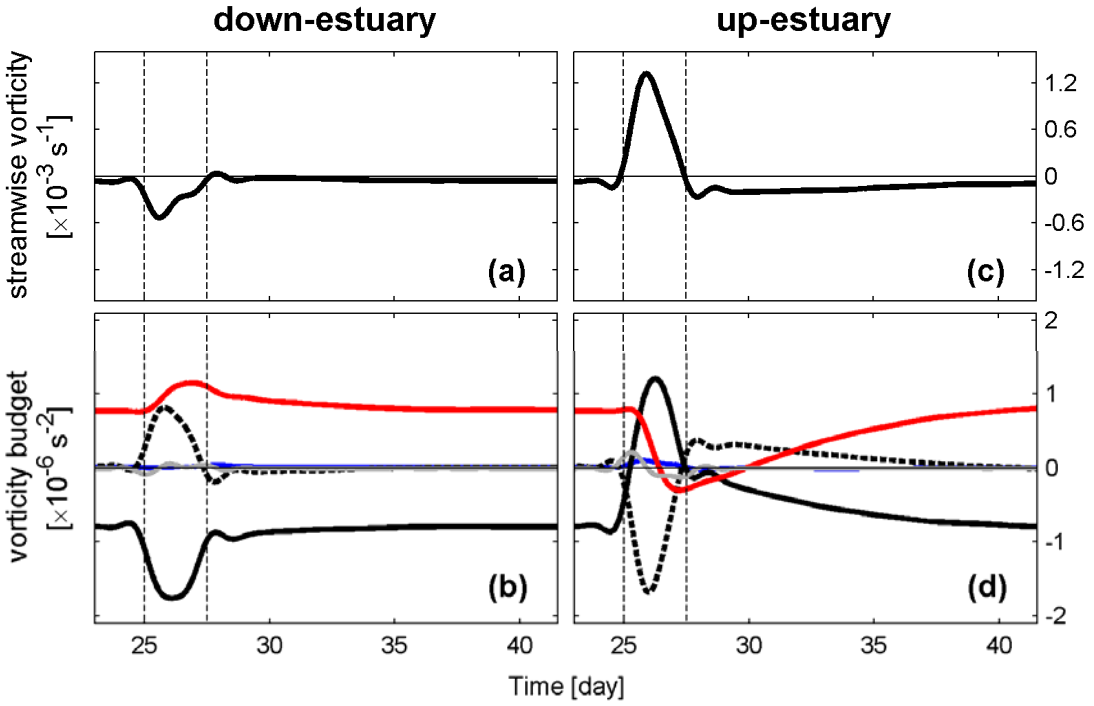

Figure 2-5. Time series of the volume-averaged (a/c) streamwise vorticity ($\overline{\omega_x}$) and (b/d) the terms in the vorticity equation: the conversion of planetary vorticity f (black solid), turbulent diffusion (black dashed), baroclinicity (red), nonlinear advection (blue) and time change rate (gray) under the down- and up-estuary wind with the peak magnitude of 0.07 Pa.

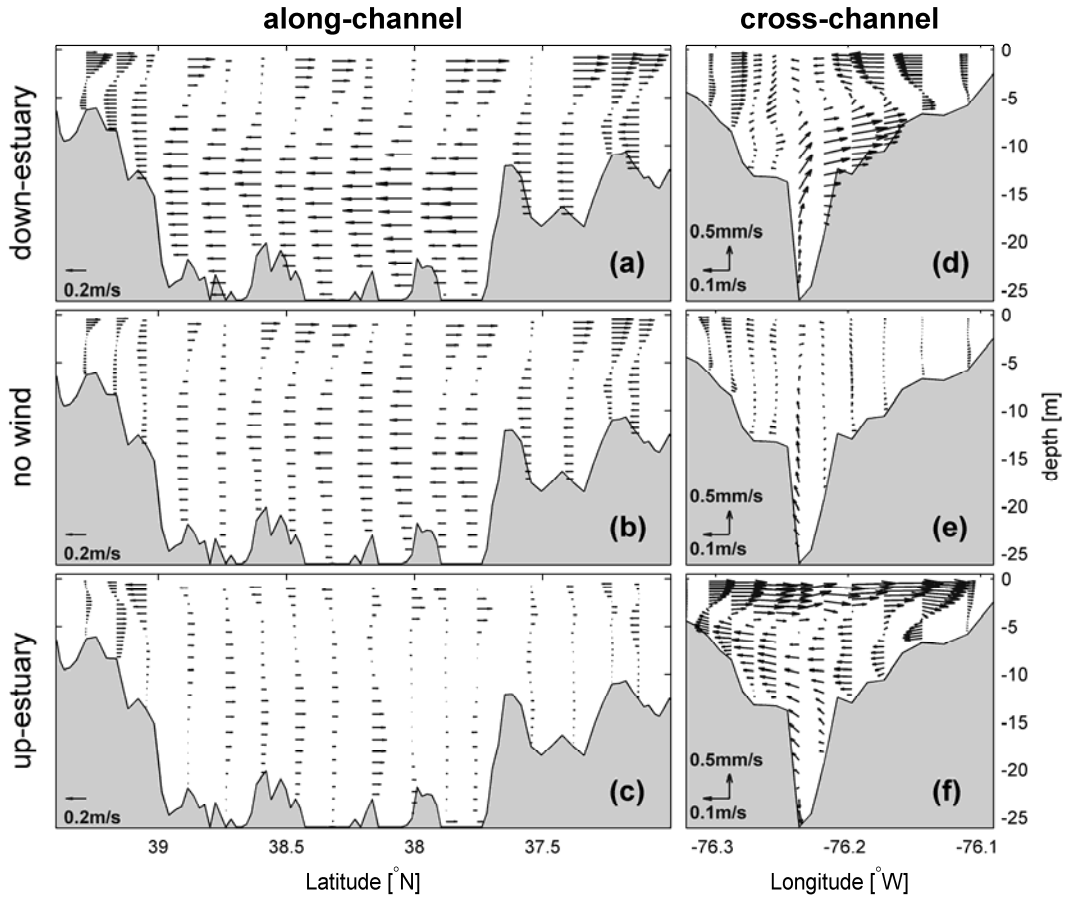

Figure 2-6. Distributions of (a-c) the subtidal along-channel current in the along-channel section and (d-f) velocity vectors at a cross-channel section for three model runs: down-estuary wind (upper panel); no wind (mid-panel) and up-estuary wind (lower panel). The snapshots are taken on 26.25 day when the wind stress reaches the peak magnitude of 0.07Pa in the two wind runs.

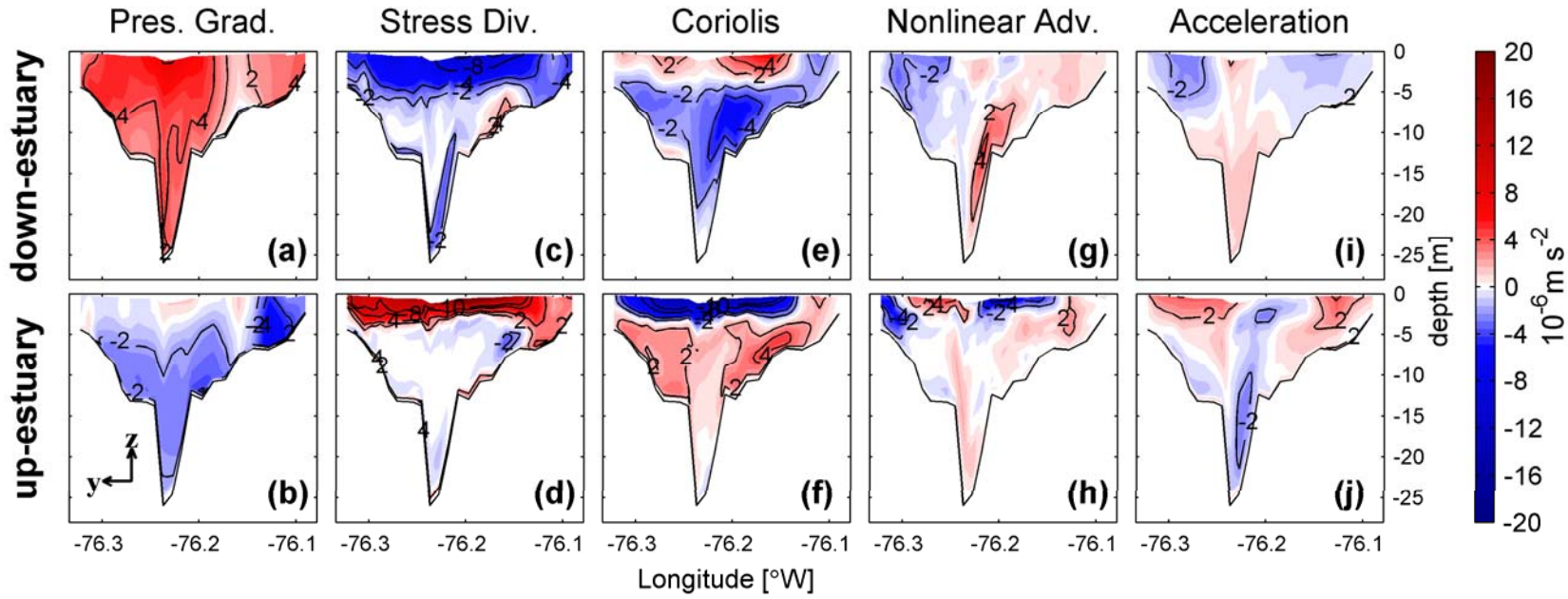

Figure 2-7. Distributions of the dominant terms in the subtidal along-channel momentum equation at a cross-channel section: (a/b) pressure gradient, (c/d) stress divergence, (e/f) Coriolis acceleration, (g/h) nonlinear advection, and (i/j) local acceleration. The top panel is for the down-estuary run and the bottom panel is for the up-estuary run. The snapshots are taken at 12 hr into the wind event with the peak magnitude of 0.07Pa.

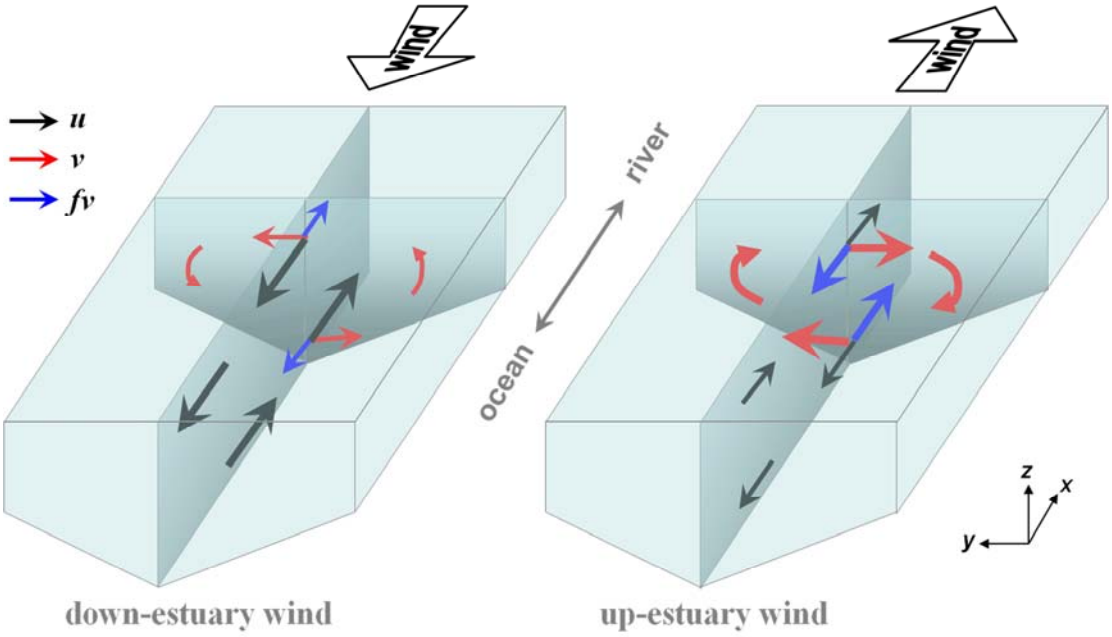

Figure 2-8. Conceptual diagram to illustrate the effects of Coriolis acceleration (*fv,* in blue) on the along-channel currents (*u,* in black). The lateral circulation is marked by red lines. The down-estuary wind generates seaward flow in the upper layer and landward flow in the lower layer, but the Coriolis force on the counterclockwise lateral circulation weakens this two-layer flow. The up-estuary wind generates landward flow in the upper layer and seaward flow in the lower layer, but the Coriolis force on the clockwise lateral circulation opposes this reversed two-layer flow.

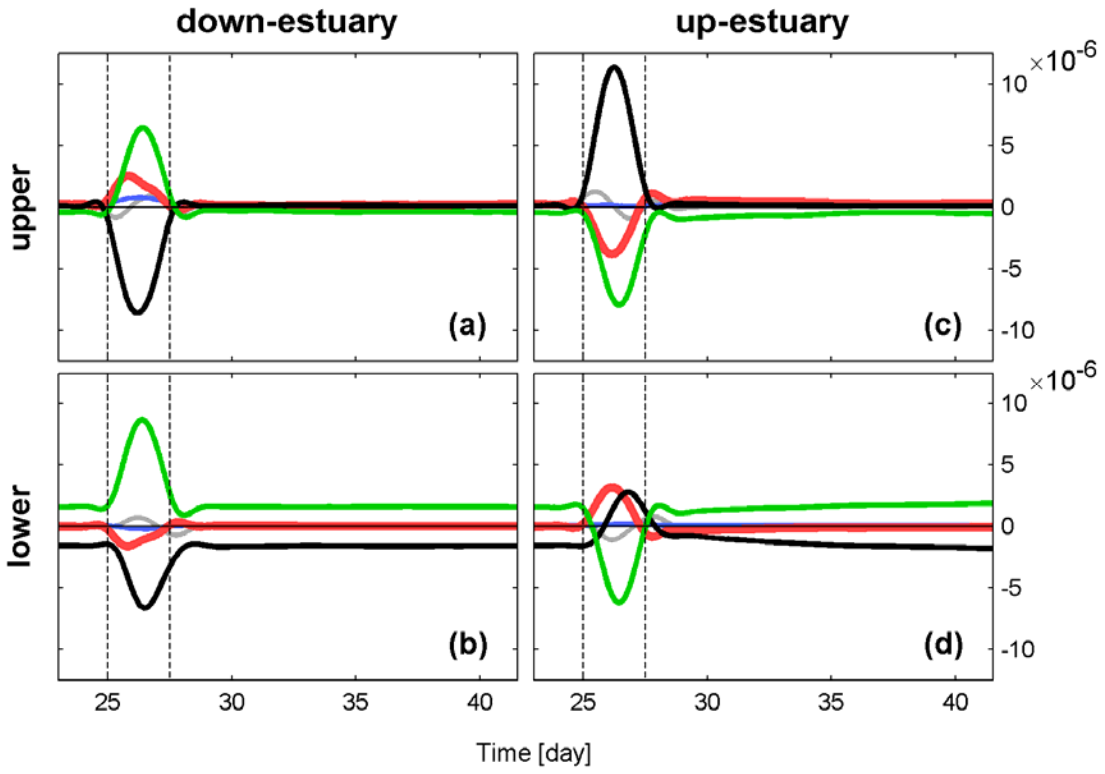

Figure 2-9. Integrated subtidal along-channel momentum balance for the upper and lower layers. The terms are the along-channel pressure gradient $-P_x/\rho_0$ (green), stress divergence $K_v v_{zz}$ (black), the Coriolis force fv (red) , the nonlinear advection $-(uu_x+vu_y+wu_z)$ (blue), and local acceleration u_t (gray). The terms are averaged over the upper (≤5 m) and lower (>5 m) layers and in unit of m s^{-2}. The down-estuary case is shown in the left column and the up-estuary case is shown in the right column. The peak magnitude of the wind is 0.07Pa.

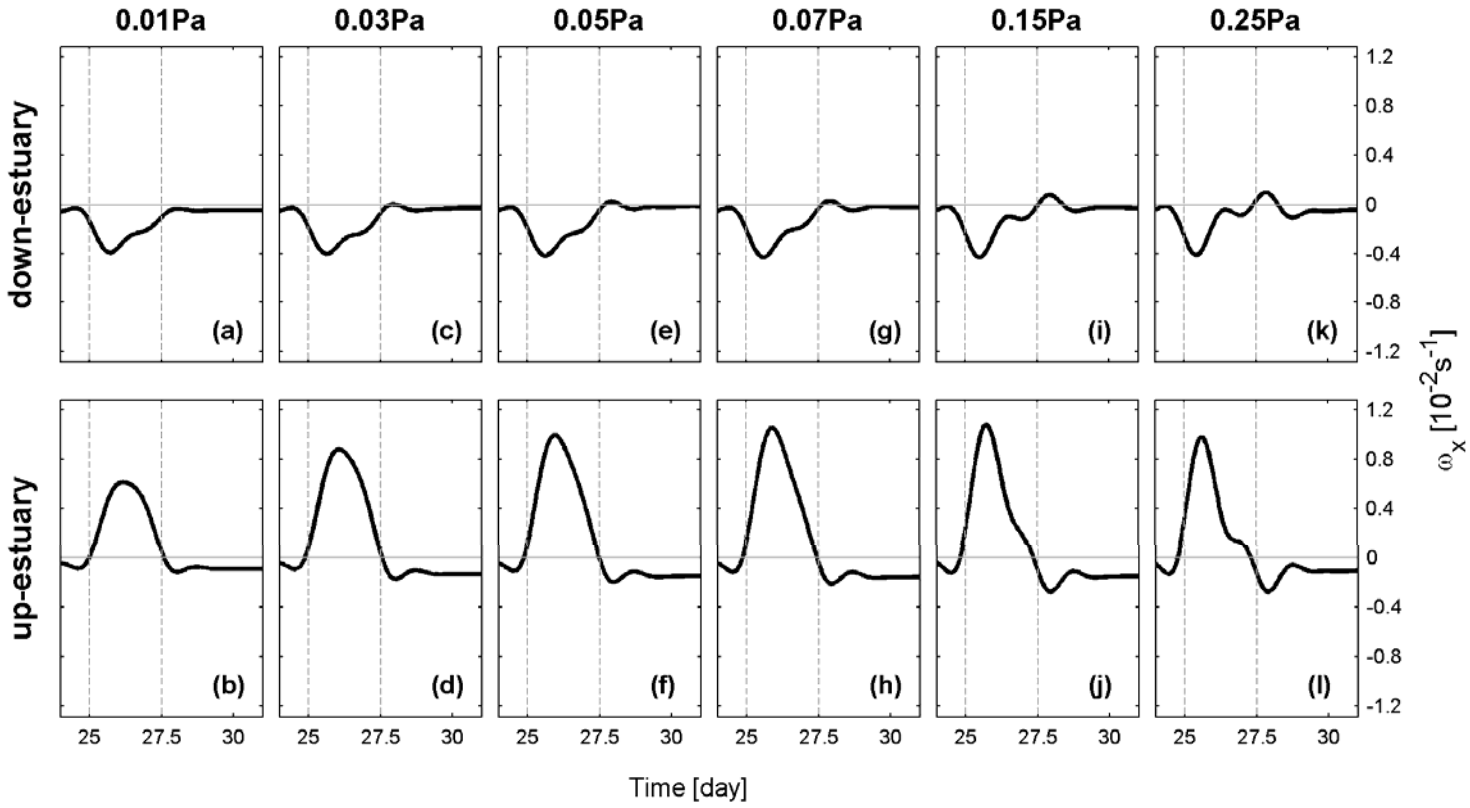

Figure 2-10. Time series of the volume-averaged streamwise vorticity in Chesapeake Bay at different wind-stress magnitudes: down-estuary winds (upper panel); up-estuary winds (lower panel). The two dashed lines mark the wind event.

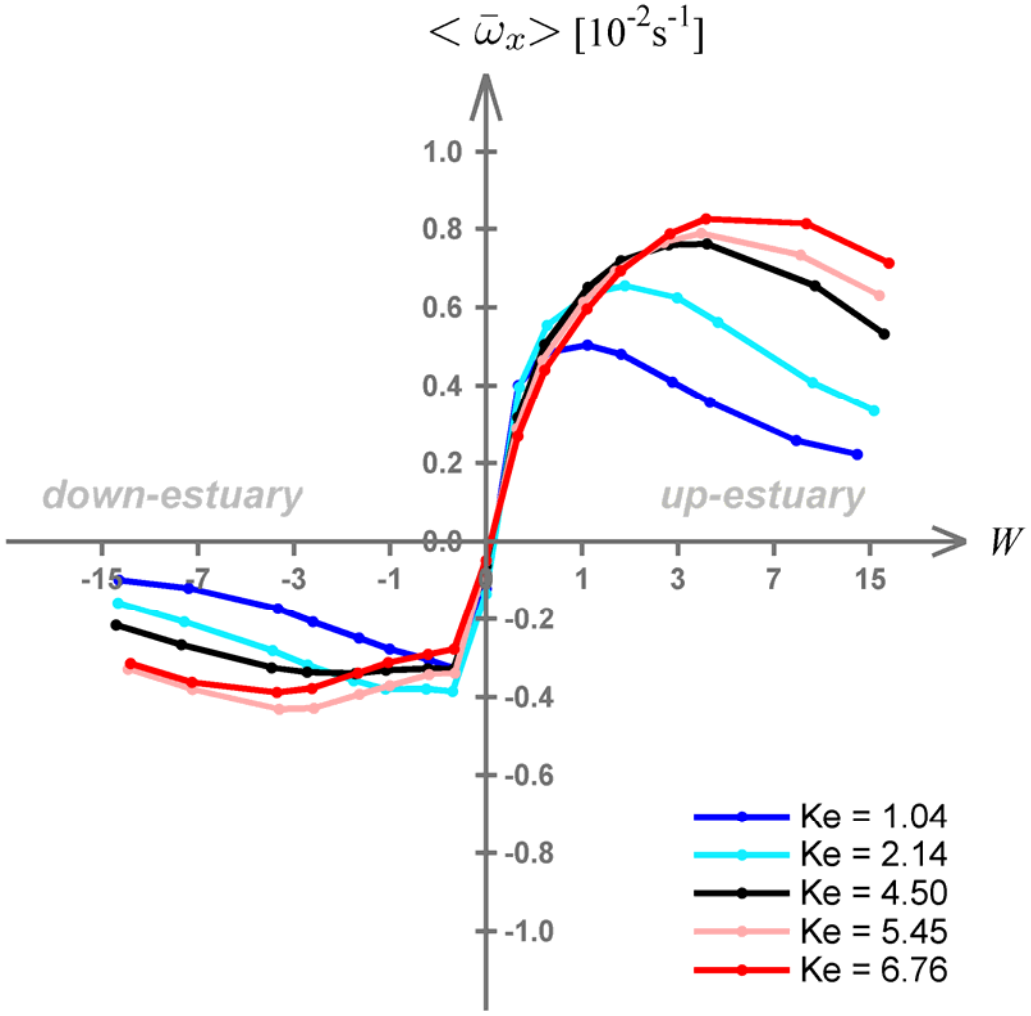

Figure 2-11. The volume-averaged streamwise vorticity $\langle \overline{\omega}_x \rangle$ as a function of Wedderburn (W) and Kelvin (Ke) numbers. Positive $\langle \overline{\omega}_x \rangle$ indicates the clockwise circulation. The W-axis is plotted in logarithmic scale with $\log_2(|W|+1)$ to reveal rapid changes of $\langle \overline{\omega}_x \rangle$ at low $|W|$ values.

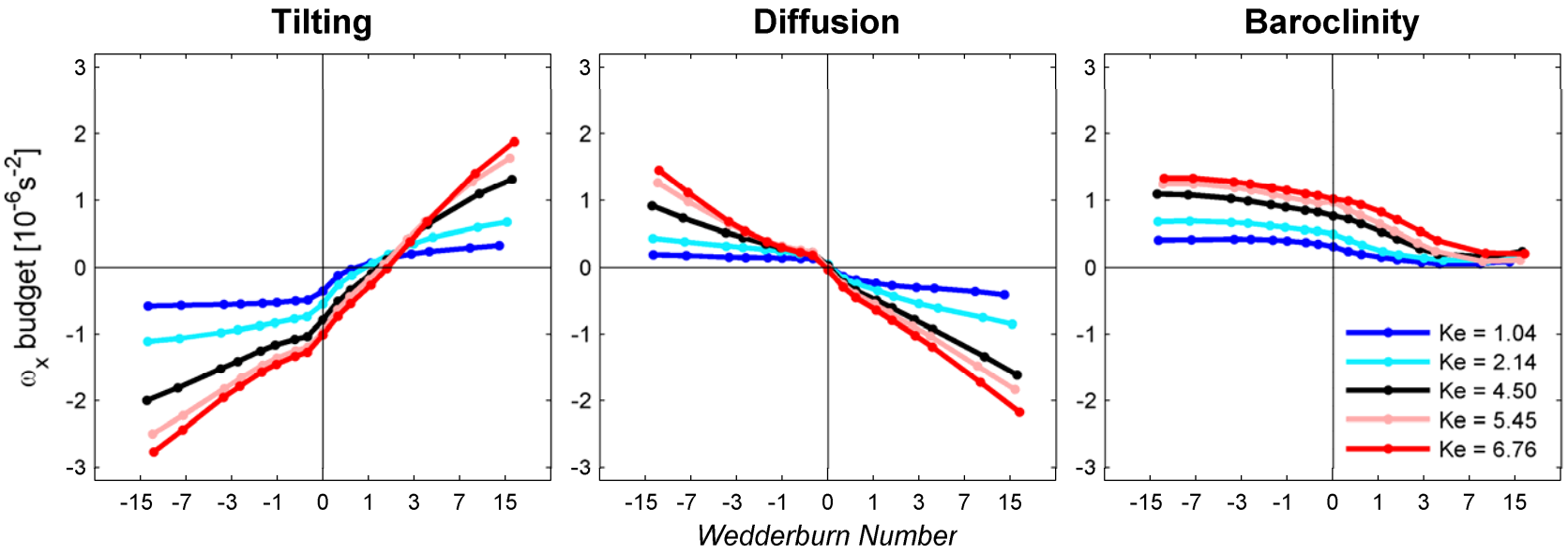

Figure 2-12. The volume-averaged terms in the streamwise vorticity as a function of Wedderburn (*W*) and Kelvin (*Ke*) numbers for all runs. The quantities are averaged over the whole wind event and in unit of $10^{-6}s^{-2}$. Positive values correspond to the generation of clockwise circulation. *W>0* corresponds to the up-estuary winds whereas *W<0* corresponds to the down-estuary winds.[3]

[3] Tilting in the 1st plot represents the conversion of the planetary vorticity *f* due to along-channel current shear.

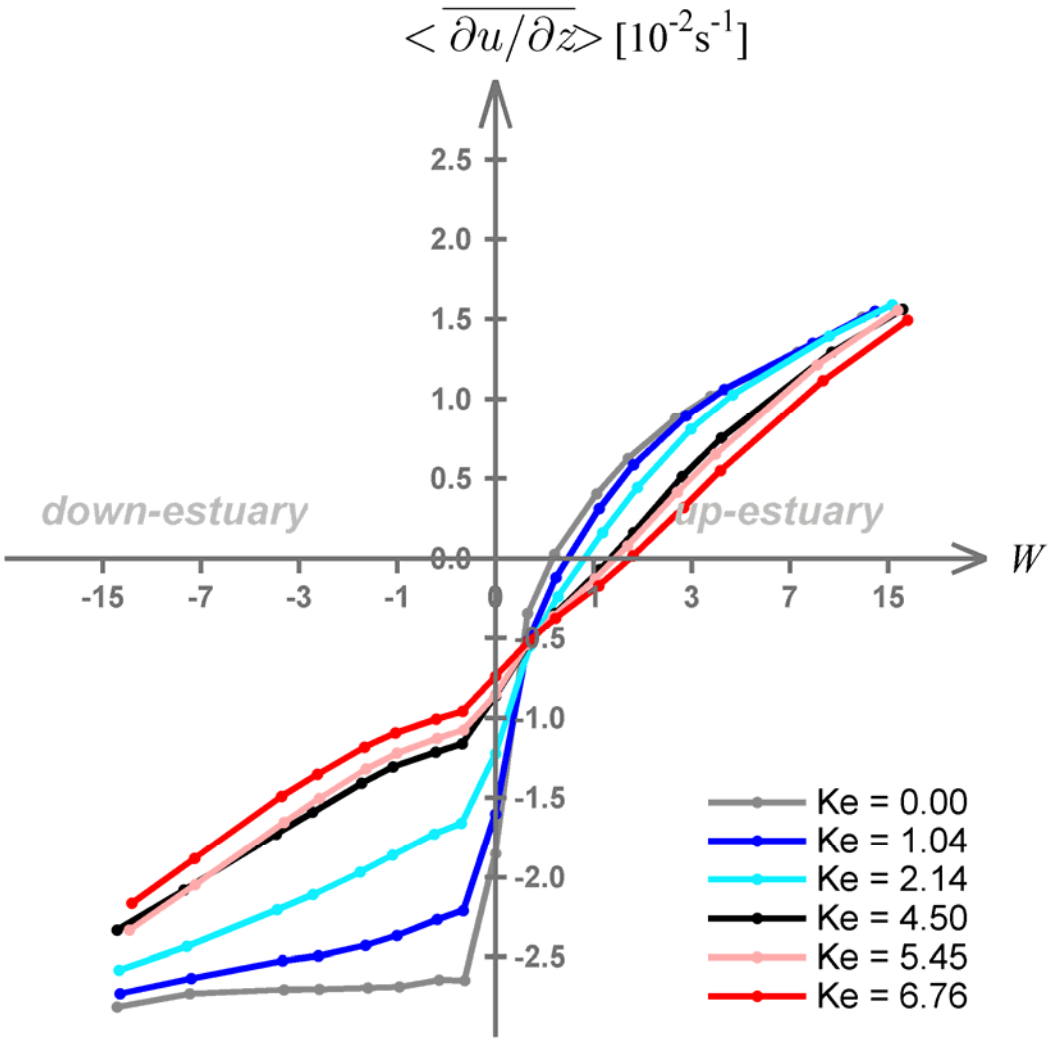

Figure 2-13. The volume-averaged along-channel shear $\langle\overline{\partial u/\partial z}\rangle$ as a function of Wedderburn (W) and Kelvin (Ke) numbers. Negative $\langle\overline{\partial u/\partial z}\rangle$ corresponds to the seaward flow in the upper layer and the landward flow in the lower layer.

Chapter 3: Effects of Winds on Stratification and Circulation in a Partially Mixed Estuary[4]

Abstract

Numerical experiments are conducted to investigate how axial winds affect stratification and circulation in the partially mixed estuary of Chesapeake Bay. In the absence of rotational effects, stratification in the estuary decreases following both down- and up-estuary winds, but stratification experiences larger reduction and takes longer to recover under up-estuary winds. In the presence of rotational effects, wind-driven lateral circulations cause the lateral straining of density field and weaken the shear in the along-channel flows. Under the down-estuary winds, a counter-clockwise lateral circulation steepens isopycnals in the cross-channel sections while the Coriolis force acting on it decelerates the downwind current in the surface layer and the upwind-directed current in the bottom layer. Under the up-estuary winds, a clockwise lateral circulation flattens isopcynals in the cross-channel sections and reduces the shear between the surface and bottom currents. Hence, in the presence of rotational effects, the lateral straining offsets the effects of longitudinal straining such that the asymmetry in stratification reduction is significantly reduced between the down- and up-estuary winds. Regime diagrams based on Wedderburn (W) and Kelvin (Ke) numbers are constructed to summarize the net effects of winds on estuarine stratification during both wind-perturbation and post-wind adjustment periods.

[4] Li, Y., and M. Li (2011), Effects of Winds on Stratification and Circulation in a Partially Mixed Estuary, *J. Geophys. Res.*, *116*, C12012, doi: 10.1029/2010JC006893

1. Introduction

Most of the research in estuarine dynamics has focused on the effects of tides. Relatively little attention has been paid to the role of winds in estuarine circulation, despite early predictions of first-order effects [*Bowden*, 1953; *Rattray and Hansen*, 1962] and observational evidence of strong wind driven flows [e.g., *Wang*, 1979a, b; *Goodrich et al.*, 1987; *Wong and Moses-Hall*, 1998; *Wong and Valle-Levinson*, 2002]. Recent studies have suggested that wind effects are not limited to mixing in the vertical direction. Since estuaries typically have strong horizontal density gradients, wind-driven currents can significantly alter estuarine stratification through the straining of density field.

North et al. [2004] and *Scully et al.* [2005] observed stratification and exchange flows that increased during moderate down-estuary winds but decreased during moderate up-estuary winds. *Scully et al.* [2005] proposed a wind straining mechanism analogous to Simpson's tidal straining: down-estuary wind enhances subtidal vertical shear and strains the along channel density gradient to increase stratification; up-estuary wind reduces or even reverses the vertical shear, thus reducing stratification. *Wilson et al.* [2008] and *O'Donnell et al.* [2008] suggested that along-channel wind straining regulates stratification and turbulent mixing, thereby influencing the flux of oxygen into hypoxic regions of western Long Island Sound.

Using a numerical model of an idealized estuarine channel featuring a triangular cross-section, *Chen and Sanford* [2009a] found that the net effect of winds on estuarine stratification depends on the competition between wind-driven mixing and wind-induced straining: moderate down-estuary winds enhance estuarine stratification whereas strong down-estuary winds and all up-estuary winds reduce stratification. They proposed a hypothetical diagram to classify the wind effects on estuarine stratification and suggested that the Wedderburn number and the ratio of the surface mixed layer to the water depth are two important non-dimensional parameters. How do the results from this idealized estuary apply to real estuaries with complex bathymetry? The Chesapeake Bay features broad shallow shoals and a narrow deep center-channel. What will be the net effects of wind-induced mixing and straining? *Chen and Sanford* [2009a] did not consider the effects of Coriolis force in their modeling study. The width of Chesapeake Bay and other similar estuaries is comparable to or larger than the internal Rossby radius of deformation. How does the Earth's rotation affect the estuarine response to wind forcing?

The response of wind-driven circulation in the along-channel direction has previously been interpreted in terms of the competition between the wind stress and barotropic pressure gradient due to sea-level setup [*Wang*, 1979b; *Garvine*, 1985; *Chuang and Boicourt*, 1989; *Janzen and Wong*, 2002]. While this two-layer theory seems well established, a number of studies in Chesapeake Bay have shown that along-channel winds can drive strong lateral Ekman flows and isopycnal movements, generating upwelling/downwelling at shallow shoals [*Malone et al.*, 1986; *Sanford et*

al., 1990; *Scully*, 2010]. The lateral flows can interact with cross-channel density gradient in a way analogous to the straining of density field in the along-channel direction. Without wind forcing, a freshwater plume hugs the western shore as it moves seaward and isopycnals tilt downwards on the western side of a cross-channel section. Southward (down-estuary) winds generate downwelling on the western shore and may tilt the isopycnals towards the vertical direction, reducing stratification. On the other hand, moderate northward (up-estuary) winds may flatten isopycnals in cross-channel sections, enhancing stratification in the water column. These lateral processes may offset the effects of wind-driven straining in the along-channel direction. Moreover, recent modeling investigations of secondary flows in tidally driven estuaries have shown that lateral advection can be of first-order importance in the along-channel momentum balance [*Lerczak and Geyer*, 2004; *Scully et al.*, 2009]. It is likely that wind-driven lateral circulations will also affect the dynamics and structure of along-channel flows, thereby indirectly affecting the density straining in the longitudinal direction.

Several recent papers have investigated the dynamics and effects of wind-driven lateral circulations. In the absence of rotational effects, *Chen and Sanford* [2009b] showed that differential advection of the axial salinity gradient by wind-driven axial flow drives bottom-divergent/convergent lateral circulation during down/up-estuary winds. In an idealized rotating basin, *Reyes-Hernández and Valle-Levinson* [2010] explored wind modifications on the lateral structure of density-driven flow. *Guo and Valle-Levinson* [2008] examined how winds affect the lateral structure of density-

driven circulation in Chesapeake Bay. Using a simplified oxygen model, *Scully* [2010] investigated wind-driven ventilation of hypoxic waters in Chesapeake Bay and found that northward winds were most effective at supplying oxygen to hypoxic regions whereas eastward winds were least effective. These interesting papers motivate the current research which is directed at understanding how wind-driven along-channel and cross-channel flows affect the stratification response in the partially mixed estuary of Chesapeake Bay.

The plan for this chapter is as follows. Section 2 describes model configuration and the design of numerical experiments. In Section 3 we analyze the estuary's response to down- and up-estuary wind events in a non-rotating system. In Section 4 we investigate how the Coriolis force and wind-driven lateral circulations affect the density stratification. Regime diagrams are constructed to summarize the wind effects on stratification in Section 5. Finally, conclusions are made in Section 6.

2. Model description

A 3D hydrodynamic model based on the Regional Ocean Modeling System (ROMS) has been developed for Chesapeake Bay and validated against observational data [*Li et al.*, 2005, 2007; *Li and Zhong*, 2009; *Zhong and Li*, 2006; *Zhong et al.*, 2008]. We use this model to investigate the effects of winds on the circulation and stratification in Chesapeake Bay.

The model domain includes 8 major tributaries and a part of the coastal ocean to facilitate free exchange across the bay mouth (Fig. 1). The total number of grid points is 120 × 80. The model has 20 layers in the vertical direction. A quadratic stress is exerted at the bed, assuming that the bottom boundary layer is logarithmic over a roughness height of 0.5 mm. The vertical eddy viscosity and diffusivity are computed using the *k-kl* turbulence closure scheme [*Warner et al.*, 2005] with the background diffusivity and viscosity set at 10^{-5} m^2 s^{-1}. Coefficients of horizontal eddy viscosity and diffusivity are set to 1 m^2 s^{-1}, which produce little dissipation of the resolved flow energy [*Zhong and Li*, 2006]. The model is forced by sea level fluctuations, temperature and salinity at the open ocean boundary, by freshwater inflows at river heads and by winds across the water surface. The open-ocean boundary condition for the barotropic component consists of Chapman's condition for surface elevation and Flather's condition for barotropic velocity. The boundary condition for the baroclinic component includes an Orlanski-type radiation condition for baroclinic velocity. To deal with both inward and outward scalar fluxes across the open boundary, we use a combination of radiation condition and nudging (with a relaxation time scale of 1 day) for temperature and salinity [*Marchesiello et al.*, 2001].

We focus on winds in the along-channel (south-north) direction since winds in the cross-channel (east-west) direction have short fetches. Weather systems passing over the Chesapeake Bay have typical periods of 2 to 5 days [*Wang*, 1979a]. In this study, we impose a spatially uniform wind forcing

$$\tau_W = \begin{cases} A\sin[\omega(t-25)] & 25 \le t \le 27.5 \\ 0 & \textit{other times} \end{cases} \quad (1)$$

where τ_W is the along-channel wind stress, t the time (days), $\omega = \frac{2\pi}{5day}$ the frequency of the wind forcing, and A the peak wind stress. We study both down- (southward) and up-estuary (northward) winds: positive τ_W corresponds to up-estuary winds. The maximum wind-stress magnitude A ranges from 0.005 to 0.25 Pa, with the corresponding range of 2.35 to 12.27 m s^{-1} for the wind speed (Table 1). To further simplify the model setup, we fix the total river discharge into the Bay at a long-term average of 1500 m^3 s^{-1} and distribute it to 8 major tributaries according to observations: Susquehanna (51%), Patapsco (3.67%), Patuxent (3.67%), Potomac (18%), Rappahannock (4%), York (2%), James (14%), and Choptank (3.67%) [c.f., *Guo and Valle-Levinson*, 2008]. We only consider tidal forcing at the dominant M_2 frequency and fix salinity at 30 psu and temperature at 15^{o}C at the offshore open boundary. To spin up the hydrodynamic model, we run it without wind forcing for 3 years so that the estuarine circulation in the Bay reaches a steady-state. The model is then forced with along-channel winds of different magnitudes and directions. In order to examine possible long-term impacts, the model is run for additional 70 days after each wind event.

3. Longitudinal straining and stratification asymmetry

Using a numerical model of an idealized estuarine channel featuring a triangular cross-section, *Chen and Sanford* [2009a] found that the net effect of winds on estuarine stratification depends on the competition between wind-driven mixing and wind-induced straining: moderate down-estuary winds enhance estuarine stratification whereas strong down-estuary winds and all up-estuary winds reduce stratification. Does this result apply to Chesapeake Bay?

We can gauge the relative importance of wind forcing by calculating the Wedderburn number [*Monismith*, 1986; *Geyer*, 1997; *Chen and Sanford*, 2009a]

$$W = \frac{\tau_W L}{\Delta\rho g H^2} \tag{2}$$

where L is the length of an estuary, $\Delta\rho$ the horizontal density difference, g the gravitational acceleration, and H the mean water depth. Assuming H = 9 m and estimating $\Delta\rho$ over the distance L between 37.2°N and 38.9°N, we find that W in Chesapeake Bay varies from ~1 to 6 for wind speeds ranging 5 ~ 10 m s^{-1} (see Table 1). Therefore, winds will significantly modify the estuarine circulation and stratification in the Bay.

Figure 2 shows a comparison of current and salinity fields among three runs: Run 1 (no wind forcing, W = 0), Run 7 (down-estuary wind with the peak wind stress at 0.07 Pa, W = -2.79), and Run 15 (up-estuary wind with the same peak stress, W = 2.56) (Table 1). We apply a 34-hr low-pass filter to remove tidal oscillations. In the

absence of wind forcing, the estuary is characterized by the two-layer gravitational circulation with sloping isohalines in the along-channel section (Figs. 2d and 2e). The tidally averaged residual flows are of order of 0.1 m s^{-1}. Vertical salinity differences of 4 ~ 6 psu stratify the water column. Strong turbulent mixing (i.e. eddy diffusivity > 10^{-4} m^2 s^{-1}) is mainly confined to the tidally driven bottom boundary layer (Fig. 2f).

When the down-estuary wind is applied over the Bay, it drives a seaward-directed current in the surface layer and causes a sea-level depression at the Bay's head. The associated pressure gradient subsequently drives a return flow in the bottom layer. Hence the down-estuary wind drives a two-layer baroclinic circulation in the stratified water, reinforcing the gravitational circulation (Fig. 2a). As a result, low salinity surface water tends to spread further downstream and high-salinity bottom water intrudes further upstream. This would sharpen the vertical salinity gradient. However, the wind also produces strong mixing in the surface layer (Fig. 2c) and erases the stratification there. As shown in the comparison between Fig. 2b and Fig. 2e, stratification in Run 7 is still weaker than in Run 1 since mixing overpowers straining effect.

When the wind blows up-estuary (Run 15), it drives a two-layer circulation that opposes the gravitational circulation (Fig. 2g). At the peak wind, the sense of the circulation is completely reversed: landward flow in the surface layer and seaward flow in the bottom layer. This shear flow moves heavier water over lighter water and steepens the isopycnals. Both the along-channel straining and wind mixing work in

concert to destabilize the water column (Figs. 2h and 2i). As a result, there is a larger reduction in stratification in Run 15 than in Run 7.

To understand how the down- and up-estuary winds affect the salinity distribution in the estuary, we analyze the salt flux through a mid-Bay section (location indicated in Fig. 1a) and decompose it as

$$\begin{aligned} F_S &= \iint (uS)(h+\zeta)d\sigma\, dy \\ &= \iint (u_0 S_0 + u_E S_E + u_T S_T)(h+\zeta)d\sigma\, dy \\ &= -Q_f S_0 + F_E + F_T \end{aligned} \tag{3}$$

where u is the velocity component orthogonal to the cross-section, S salinity, h the local depth, ζ the instantaneous sea level, and σ, y are vertically stretched s-coordinate and horizontal coordinate in the cross-channel direction [*Lerczak and Geyer*, 2006; *Chen and Sanford*, 2009a]. The velocity and salinity are decomposed into tidally and cross-sectionally averaged (u_0 , S_0), tidally averaged but cross-sectionally varying (u_E , S_E), and tidally and cross-sectionally varying (u_T , S_T) component, respectively. The resultant salt flux consists of three terms: $-Q_f S_0$ includes the river-induced salt loss and wind-induced barotropic adjustment; F_E results from shear dispersion[5] due to estuarine exchange flow; and F_T represents tidal oscillatory salt flux. Because tides in Chesapeake Bay are relatively weak, the tidal

[5] After cross-section average, the salt transport F_E due to shear-induced differential advection is expressed as a process creating longitudinal spreading, which we name "shear dispersion" to be consistent with *Lerczak and Geyer* [2004].

oscillatory salt flux F_T is small ($F_T/F_E \approx 0.01$ at this section). Since F_E is the product of subtidal exchange flow and subtidal salinity variability, it is closely related to the stratification change in the estuary: the estuarine stratification increases when $F_E > 0$ and decreases when $F_E < 0$.

The down-estuary wind initially produces a seaward-directed barotropic current that drives the water and salt out of estuary, as shown in Fig. 3a. Subsequently, the sea-level depression at the head drives a landward flow which advects salt back to the estuary. More importantly, the salt flux due to shear dispersion F_E doubles during the down-estuary wind event, with the peak value reaching 3.44×10^4 kg s^{-1} as compared with the pre-wind value of 1.71×10^4 kg s^{-1} (Fig. 3b). This corresponds to an amplification of subtidal velocity shear (defined to be the averaged velocity shear between the surface and bottom layers) from the pre-wind value of 1.8×10^{-2} s^{-1} to the maximum of 3.5×10^{-2} s^{-1} (Fig. 3c). This shear flow exports less saline water seaward and imports more saline water landward, producing a net influx of salt into the estuary and increasing stratification in the water column. When the Bay is forced by the up-estuary wind, however, the wind-driven barotropic flow initially transports salt into the estuary while the subsequent sea-level pileup at the Bay's head drives a seaward flow and salt out of the estuary (Fig. 3e). Since the wind-driven current cancels or even reverses the gravitational flow (Fig. 3g), F_E decreases and even becomes negative around the peak wind (-1.9×10^4 kg s^{-1}, Fig. 3f) such that salt is removed from the estuary and vertical stratification is weakened. Therefore, the

asymmetry in stratification reduction between the down- and up-estuary winds is closely related to the differences in the shear-dispersion salt flux F_E.

To quantify the wind effects on the estuarine stratification, we select a control volume inside the main stem of Chesapeake Bay (the shaded area in Fig. 1b) and calculate the volume-averaged buoyancy frequency $\overline{N^2}$. $\overline{N^2}$ is 2.5×10^{-3} rad^2 s^{-2} prior to the wind event. During the wind event (day 25 to 27.5), stratification decreases under both the up-estuary and down-estuary winds (Figs. 4e and 4f). We conduct several other runs with wind stress ranging from 0.01 to 0.15 Pa (Table 1). In all the cases studied, the volume-averaged stratification decreases following both the down-estuary and up-estuary wind events and the stratification reduction is larger at higher winds (Fig. 4). *Chen and Sanford* [2009a] showed that stratification reduction occurs for down-estuary winds when $W <\sim -1.8$. The horizontal salinity gradient dS/dx in Chesapeake Bay is about 4×10^{-5} psu m^{-1}, an order of magnitude smaller than that in other estuaries, such as York River [O(10^{-4})] [*Scully et al.*, 2005] and Hudson River [O(10^{-4})] [*Lerczak and Geyer*, 2006; *Ralston et al.*, 2008]. Hence $|W|>1.8$ for wind speeds over 6 m s^{-1}, placing Chesapeake Bay to the mixing-dominated regime under most wind-forcing conditions. The weak horizontal salinity gradient limits the advective buoyancy flux and hence its ability to create stratification during the down-estuary winds.

Although the stratification decreases under both wind directions, it experiences larger reductions and takes longer to recover under the up-estuary winds than under

the down-estuary winds, as shown in Fig. 4. It is particularly interesting to note that the stratification takes 1-3 weeks to recover fully after the up-estuary wind event. In contrast, the stratification recovers shortly after the passage of the down-estuary wind event. *Chen and Sanford* [2009a] also noticed this long adjustment time after the up-estuary winds, but did not provide an explanation. Ignoring the effects of lateral flows, the stratification change in an estuary depends on the balance between the straining in the along-channel direction and turbulent mixing [see terms (4) and (7) in Eq. (4)]. The shear $\partial u / \partial z$ at the end of the down-estuary wind is about 4 times of that at the end of the up-estuary wind (Figs. 3c and 3g) while the averaged eddy diffusivity *Ks* is about 50% smaller (Figs. 3d and 3h). These differences in the shear and diffusivity will result in large differences in $\partial N^2 / \partial t$. Moreover, the net reduction in $\overline{N^2}$ at the end of the wind event is considerably larger for the up-estuary winds than for the down-estuary winds. All these differences contribute to the large asymmetry in the post-wind stratification recovery times between the two wind directions. We also note that the salt flux due to shear dispersion takes longer to recover under the up-estuary wind than under the down-estuary wind (Figs. 3b and 3f).

4. Lateral versus longitudinal straining on stratification

In Chesapeake Bay where the baroclinic Rossby radius (about 5 km) is smaller than or comparable to the width of the estuary (5-20 km), along-channel winds can drive lateral Ekman flows and isopycnal movements, generating upwelling/downwelling at shallow shoals [*Malone et al.*, 1986; *Sanford et al.*, 1990;

Scully, 2010]. In this section, we investigate how the wind-driven lateral flows affect stratification in the estuary.

First we compare current and salinity fields at a mid-Bay cross-section among three model runs: Run 18 (no wind forcing); Run 24 (down-estuary wind with the peak wind stress at 0.07Pa); and Run 32 (up-estuary wind with the same peak stress), all incorporating the rotational effects (see Table 1 and Fig. 5). Without wind forcing, the brackish plume is deflected toward the western shore due to the Coriolis force. In the cross-channel section, isopycnals slope downwards on the western flank, with the seaward flow hugging the western shore and the landward flow confined to the deep channel (Fig. 5d and 5e). The lateral flows are weak (Fig. 5d) and the eddy diffusivity is low (Fig. 5f).

When along-channel winds are applied over the Bay's surface, they drive strong lateral flows with speeds reaching O(0.1) m s^{-1}. Under the down-estuary wind, the wind-driven Ekman transport is directed westward and a counter-clockwise circulation appears over deep channel and eastern shoal. The strong lateral salinity gradient drives an eastward flow on the western shoal. The isopycnals are steepened in the upper 5-10 m, featuring weak stratification and strong mixing (Figs. 5a-c). The along-channel flow reveals a laterally sheared structure, with the downwind flow in the two shallow shoals and the upwind flow over the deep channel. This laterally sheared flow structure is consistent with the theoretical predictions of *Csanady* [1973], *Wong* [1994] and *Winant* [2004] for wind-driven barotropic flows over varying

bottom bathymetry. The sense of the lateral circulation (clockwise) is reversed under the up-estuary wind forcing since the wind-driven Ekman transport is now directed eastward (Fig. 5g). The upwelling flows lift the isopycnals on the western side up from the depressed positions (Fig. 5h). Compared with the down-estuary wind case (Fig. 5b), the isopycnals appear to be more horizontal, and significant stratification is retained in the water column (Fig. 5h) while strong turbulent mixing is confined to a relatively shallow surface layer (Fig. 5i). The along-channel flow is primarily a vertically sheared two-layer flow. The stratification lessens the effects of bottom bathymetry on the flow structure. It is noted that the clockwise circulation generated during the up-estuary wind appears to be stronger than the counter-clockwise circulation generated during the down-estuary wind.

Wind-driven lateral flows affect the estuarine stratification not only by rearranging isopycnals in cross-channel sections but also by reducing the shear in the along-channel current and thus the effectiveness of the longitudinal wind straining of the density field. To illustrate this second effect, we plot the along-channel distributions of subtidal along-channel current, salinity and eddy diffusivity for the rotational runs (Fig. 6) and compare them with those from the non-rotational runs (Fig. 2). Although the down-estuary wind amplifies the two-layer circulation, the velocity shear is weaker in Run 24 than in Run 7 (compare Fig. 6a with Fig. 2a). The Coriolis force acting on the westward lateral flow decelerates the downwind current in the surface layer while the Coriolis force acting the eastward lateral flow decelerates the upwind-directed current in the deep channel. Therefore, the shear in

the along-channel current is weakened in the presence of rotational effects. Analysis of the along-channel momentum balance shows that the Coriolis acceleration fv is of the similar order of magnitude as the net driving force (sum of pressure gradient and stress divergence) $-\frac{1}{\rho}\frac{\partial P}{\partial x}+\frac{\partial}{\partial z}\left(K_V\frac{\partial u}{\partial z}\right)$ in each flow layer but has the opposite sign. Detailed analysis of the along-channel and cross-channel momentum equations as well as the streamwise vorticity equation is presented in Chapter 2. Similarly, the along-channel flow under the up-estuary wind (Run 32) does not feature a strong reversed two-layer circulation as seen in the non-rotating run (Run 15). It is weak over most of the along-channel section (compare Figs. 6g and 2g). This weak shear is also due to the Coriolis force acting on the clockwise lateral flows. The along-channel salinity distribution also exhibits large differences between the rotational and non-rotational runs. Under the down-estuary wind, the isopycnals near surface are tilted vertically and strong turbulent mixing extends down to about 10 m depth (Figs. 6b and 6c). Under the up-estuary wind, however, significant stratification remains in the surface layer and strong turbulent mixing is limited to a shallower depth (Figs. 6h and 6i). In the absence of the rotational effects, however, the turbulent mixing in the surface layer is stronger under the up-estuary winds than under the down-estuary winds (see Figs. 2c and 2i).

Next we calculate the salt flux through the mid-bay section, as shown in Fig. 7. The barotropic salt flux shows a reversal near the onset and termination of the wind event, as in the non-rotating runs. We focus our attention on the salt flux due to shear dispersion F_E, which is directly related to the estuarine stratification. Similar to the

non-rotating runs, F_E recovers more quickly under the down-estuary wind than under the up-estuary wind. However, F_E in the rotating runs is different from that in the non-rotating runs in three noticeable ways. First, the maximum deviations of F_E from its pre-wind equilibrium are 1.45×10^4 kg s^{-1} (down-estuary wind) and -3.44×10^4 kg s^{-1} (up-estuary wind) in the rotational runs. They are weaker than 1.73×10^4 kg s^{-1} (down-estuary wind) and -3.62×10^4 kg s^{-1} (up-estuary wind) in the non-rotating runs. Second, F_E reaches its maximum/minimum value at 6 hours later than in the non-rotating runs. Third, the salt flux due to shear dispersion remains weak for about 10 days after the passage of the up-estuary wind event, though it recovers to the pre-wind level shortly after the down-estuary wind event. As discussed earlier, the Coriolis force acting on the lateral flows weakens the shear in the along-channel flow (compare Figs. 7c and g with Figs. 3c and g), resulting in weak salt flux and slow recovery of salt in the estuary. Finally, we note that the volume-averaged eddy diffusivity is larger in the down-estuary wind case than in the up-estuary wind case during the wind-perturbation period (also see Figs. 5c and 5i), but the diffusivity is slightly stronger after the up-estuary wind than after the down-estuary wind (Figs. 7d and h).

To quantify the effects of winds on the stratification in the Bay, we calculate the volume-averaged $\overline{N^2}$ for all rotating runs, as shown in Fig. 8. Compared with the time series for the non-rotating runs (Fig. 4), the stratification reduction during the wind event (day 25 to 27.5) is significantly weaker. Similar to the non-rotating runs,

the stratification decreases under all the down-estuary winds. However, the stratification change is very different under the up-estuary winds. At moderate wind speeds, the lateral advection actually causes a brief increase of $\overline{N^2}$ (Figs. 8d, f). This stratification increase is caused by the flattening of isopycnals at the cross-channel sections at the beginning phase of the wind event. Further upwelling at the western shore will tilt the isopycnals towards the vertical direction and reduce the stratification (c.f. Fig. 5h). At high up-estuary winds, strong upwelling associated with the clockwise lateral circulation and vertical tilting will quickly lead to a reduction in stratification. Moreover, the longitudinal straining and strong wind mixing contribute to further stratification reduction (Figs. 8f and 8h). In the presence of rotational effects, the magnitude of stratification reduction is nearly the same between the down-estuary and up-estuary winds for wind stress at 0.07 and 0.15 Pa. This contrasts with the large stratification asymmetry found in the non-rotating runs (Fig. 4). More significant difference between the down- and up-estuary winds lies in the post-wind stratification-recovery time. Under the down-estuary winds, $\overline{N^2}$ recovers shortly after the passage of the wind. Under the up-estuary winds, however, the stratification recovery takes 1-3 weeks to complete.

To understand how the estuarine stratification responds to the wind forcing, we conduct a diagnostic analysis of the stratification equation given by

$$\frac{\partial N^2}{\partial t} = \underbrace{\overbrace{(-u\frac{\partial N^2}{\partial x})}^{(1)} + \overbrace{(-v\frac{\partial N^2}{\partial y})}^{(2)} + \overbrace{(-w\frac{\partial N^2}{\partial z})}^{(3)}}_{\text{advection}} + \underbrace{\overbrace{(g\beta\frac{\partial u}{\partial z}\frac{\partial S}{\partial x}}^{(4)} + \overbrace{g\beta\frac{\partial v}{\partial z}\frac{\partial S}{\partial y}}^{(5)} + \overbrace{g\beta\frac{\partial w}{\partial z}\frac{\partial S}{\partial z}}^{(6)})}_{\text{straining}}$$

$$+ \underbrace{\overbrace{\left[-g\beta\frac{\partial^2}{\partial z^2}(K_S\frac{\partial S}{\partial z})\right]}^{(7)} + \overbrace{\left[-g\beta\frac{\partial^2}{\partial z\partial x}(K_H\frac{\partial S}{\partial x})\right]}^{(8)} + \overbrace{\left[-g\beta\frac{\partial^2}{\partial z\partial y}(K_H\frac{\partial S}{\partial y})\right]}^{(9)}}_{\text{diffusion}} \tag{4}$$

where terms (1)-(3) represent the advection terms, terms (4)-(6) represent the straining terms and terms (7)-(9) represent the diffusion terms. The appendix provides details how to calculate these terms numerically in the ROMS model.

We compare the magnitudes of the straining terms in the along- and cross-channel directions at the mid-Bay section (Fig. 9). The along-channel salinity gradient $\partial S/\partial x$ is estimated as the average value between 37.2°N and 38.9°N while the cross-channel salinity gradient $\partial S/\partial y$ is estimated as the average salinity difference between the western and eastern shore in the mid-bay section. The currents are detided through a 34-hr low-pass filter and the vertical shears $(\partial u/\partial z, \partial v/\partial z)$ are calculated from the surface-to-bottom velocity difference and then averaged over the cross-section. Under the down-estuary wind, the along-channel current shear is amplified (Fig. 9a) and acts on the longitudinal salinity gradient to create stratification (Fig. 9c). On the other hand, the counter-clockwise lateral circulation steepens the isopycnals to reduce the stratification. Since $\partial S/\partial y$ is 3-5 times larger than $\partial S/\partial x$, the lateral straining overcomes the longitudinal straining at this mid-Bay

section (Fig. 9c). The relative magnitudes of $g\beta\frac{\partial u}{\partial z}\frac{\partial s}{\partial x}$ and $g\beta\frac{\partial v}{\partial z}\frac{\partial s}{\partial y}$ change at different cross-channel sections, but they are always of the opposite signs. Under the up-estuary wind, the shear in the along-channel direction is reversed (Fig. 9d) such that its straining over the longitudinal salinity gradient causes a stratification reduction (Fig. 9f). The clockwise lateral circulation acting on the lateral salinity gradient initially opposes it by flattening the isopycnals in the cross-channel sections, causing a temporal rise in the stratification (Fig. 9f). Later on, however, upwelling and lifting of isopycnals on the western shore causes a reversal of the lateral salinity gradient (Fig. 9e). The straining of $\partial S/\partial y$ by the lateral circulation leads to the tilting of isopycnals towards the vertical direction and a stratification reduction. Therefore, the lateral straining opposes the longitudinal straining to cause a temporal stratification increase in the first part of the wind event, but the lateral and longitudinal straining work together to destroy stratification in the later part of the wind event. This explains why the stratification decreases after the initial spike under the up-estuary winds (Fig. 8).

The above analysis can be summarized in terms of the competition between along-channel and cross-channel straining. When forced by the down-estuary wind, the velocity shear in the along-channel direction is enhanced. The straining of this shear across the longitudinal salinity gradient leads to restratification since $\frac{\partial u}{\partial z}\frac{\partial S}{\partial x} > 0$. On the other hand, the counter-clockwise secondary circulation steepens the isopycnals in the cross-channel sections, increases the lateral salinity gradient and

reduces stratification since $\frac{\partial v}{\partial z}\frac{\partial S}{\partial y} < 0$. When forced by the up-estuary wind, the clockwise secondary circulation flattens the isopycnals, reduces the lateral baroclinic gradient and increases N^2 since $\frac{\partial v}{\partial z}\frac{\partial S}{\partial y} > 0$, even though the wind straining in the along-channel direction acts to reduce the stratification ($\frac{\partial u}{\partial z}\frac{\partial S}{\partial x} < 0$). Hence the wind-driven lateral flows offset the effects of the along-channel straining. The only exception to this offsetting effect is found during the second half of up-estuary wind events when the along- and cross-channel straining may act together to reduce the stratification in the estuary.

We have integrated Eq. (4) over the same control volume used to calculate the estuary-wide averaged stratification and compared the relative magnitudes of the advection, straining and turbulent diffusion terms, as shown in Fig. 10. Before the wind event, the stratification reaches quasi-equilibrium due to the balance between the straining and turbulent diffusion. The introduction of wind forcing upsets this balance. At the beginning of the down-estuary wind event, the lateral straining overcomes the longitudinal straining to cause a small drop in the total straining term. Subsequently, the wind-driven along-channel straining enhances the straining term. The advection term is an order of magnitude smaller than the straining term. The diffusion term reaches a maximum around the peak wind. The sum of straining, advection and diffusion is equal to the temporal change of the volume-averaged $\overline{N^2}$ which is negative in the first half of the wind event but becomes positive during the

second half. This explains the time series of $\overline{N^2}$ which decreases in the first half of the down-estuary wind event but increases in the second half (Figs. 8a, c, e, g). The diagnostics of the stratification equation (4) reveals more dramatic changes during the up-estuary winds. The total straining term is enhanced due to the isopycnal flattening in the cross-channel sections in the first half of the wind event but is reduced due to the along-channel straining in the second half. Again the advection term is much smaller than the straining term. The time tendency $\partial N^2 / \partial t$ is positive initially but turns negative later on. This explains the initial spike of $\overline{N^2}$ and the subsequent drop in stratification under the up-estuary winds (Figs. 8b, d, f).

5. Regime diagram

The effects of along-channel and lateral straining on estuarine stratification can be summarized in a regime diagram based on dimensionless parameters. The effect of along-channel straining can be described by the Wedderburn number W [*Monismith*, 1986; *Geyer*, 1997; *Chen and Sanford*, 2009a]. The relative importance of the Earth's rotation can be described by Kelvin number *Ke*, which can be described as the ratio of the basin's width to internal Rossby radius [*Garvine*, 1995; *Valle-Levinson*, 2008].

$$Ke = \frac{fB}{\sqrt{g' h_S}} \tag{5}$$

where f is the Coriolis parameter, B the basin/estuary width, g' the reduced gravitational acceleration determined by the density difference between the surface and bottom layers, and h_S the mean depth of the surface layer. The rotational effect becomes important if $Ke > 1$. The non-rotating runs correspond to Ke = 0 while the rotating runs correspond to Ke = 4.26. Although the model bathymetry is specific to Chesapeake Bay, we change f by $\pm 50\%$ as a preliminary way to explore estuaries of different widths (Table 1).

To characterize changes in estuarine stratification during the wind-forcing period, we average the volume-averaged buoyancy frequency over the entire duration of the wind event $\overline{N^2}$ and normalize it by its pre-wind value $\overline{N_0^2}$. When the normalized stratification is below unity, the net wind effect is a decrease in the stratification, and *vice versa*. As shown in Fig. 11a, the stratification always decreases at large values of $|W|$, indicating that strong wind mixing overcomes straining processes to reduce stratification. In the non-rotating cases (Ke = 0), the wind straining opposes/augments wind mixing during down-/up-estuary winds, as suggested in *Scully et al.* [2005]. Hence the stratification reduction during the down-estuary winds is smaller than that during the up-estuary winds of the same magnitude. In the presence of rotation, this stratification-reduction asymmetry is weakened. The lateral tilting offsets the along-channel straining to produce smaller stratification reduction under up-estuary winds. At moderate positive W values, the lateral straining overpowers the longitudinal straining to increase stratification. This effect is stronger at higher values of Ke

(strongly rotating systems or wider estuaries). In comparison, the stratification reduction is relatively insensitive to *Ke* values under the down-estuary winds.

As shown in Figs. 4 and 8, the wind effects are not limited to the period of active wind forcing but may persist well after the termination of the wind event. For example, one striking difference between the down- and up-estuary winds is the stratification recovery time after the passage of the wind event. Figure 11b summarizes the recovery time (defined as the time taken for $\overline{N^2}$ to recover to 95% of its pre-wind value) as a function of Wedderburn number *W* at different values of Kelvin number *Ke*. There is a strong asymmetry in the post-wind recovery time between the down- and up-estuary winds under all values of *Ke*, although the asymmetry is somewhat weaker in the non-rotating case (*Ke* = 0). The stratification recovers quickly (less than 1 day) to the pre-wind values under all down-estuary winds in the presence of the rotational effects. In contrast, it takes considerably longer for the stratification to recover under the up-estuary winds. The recovery time increases with *Ke* and is a rapidly increasing function of *W* for $W < 2$ but a slowly increasing function of *W* for $W > 2$. Another way to present the post-wind effects is to calculate the average value of $\overline{N^2}$ during the post-wind recovery period, as shown in Fig. 11c. Since the stratification takes much longer to recover under the up-estuary winds than the down-estuary winds, the time-averaged stratification is weaker after the up-estuary winds than after the down-estuary winds.

6. Conclusions

We have conducted process-oriented numerical experiments to investigate how the Chesapeake Bay estuary responds to down- and up-estuary winds. In the absence of rotational effects, stratification in the estuary decreases following both down- and up-estuary winds, but the stratification experiences larger reduction and takes longer to recover under up-estuary winds. In the presence of rotational effects, the down-/up-estuary winds drive counter-clockwise/clockwise lateral circulations which rearrange isopycnals in cross-channel sections and reduce shear in the along-channel currents. Therefore, the lateral straining weakens the effects of the longitudinal straining and reduces the asymmetry in stratification reduction between the down- and up-estuary winds.

Regime diagrams are constructed to summarize the wind effects on estuarine stratification and post-wind recovery time in the non-dimensional parameter space of Wedderburn (W) and Kelvin (Ke) numbers. For the down-estuary winds ($W < 0$), the estuarine stratification decreases with increasing magnitude of $|W|$ but is nearly independent of Ke. For the up-estuary winds ($W > 0$), the stratification decreases with increasing W but increases with Ke. The post-wind stratification recovery time shows a strong asymmetry between the down- ($W < 0$) and up-estuary ($W > 0$) winds. The stratification recovers quickly (less than 1 day) to the pre-wind values under all down-estuary winds, but it takes 1-3 weeks to recover under the up-estuary winds. The regime diagrams are based on the model results for Chesapeake Bay. Although

the Bay is a good example of a partially mixed estuary, it is somewhat special since it receives freshwater inputs from western tributaries, in addition to that from the Susquehanna River at its northern end. Nevertheless, the regime diagrams could provide a starting point to assess the relative importance of lateral versus longitudinal straining in different types of wind-forced estuaries, such as Long Island Sound, York River, and Albemarle and Pamlico Sound.

We have examined the sensitivity of model results to turbulence closure schemes and conducted parallel numerical experiments using the KPP model. The model results are quantitatively similar to those based on the k-kl turbulence model. Our previous model simulations [*Li et al.*, 2005*,* 2007] also found such insensitivity to different turbulence parameterization schemes.

For the future work, we plan to conduct model simulations using idealized but more generic estuarine-channel geometry (such as those used in *Chen and Sanford* [2009a, b] and *Lerczak and Geyer* [2004]) and examine if the regime diagrams are sensitive to details in the estuarine bathymetry. Further work is also needed to relate these idealized mechanistic studies to field observations of the estuarine response to wind events. In wide estuaries such as Chesapeake Bay, our modeling investigations demonstrate that the rotational effects are important and a full understanding of the estuarine response to the wind forcing requires the documentation of the three-dimensional flow and density fields.

Appendix

The equation for the salt conservation is given by

$$\frac{\partial S}{\partial t} = -\left(u\frac{\partial S}{\partial x} + v\frac{\partial S}{\partial y} + w\frac{\partial S}{\partial z} \right) + \frac{\partial}{\partial z}\left(K_S \frac{\partial S}{\partial z} \right) + \frac{\partial}{\partial x}\left(K_H \frac{\partial S}{\partial y} \right) + \frac{\partial}{\partial x}\left(K_H \frac{\partial S}{\partial y} \right) \qquad \text{(A1)}$$

where S is the salinity, u, v and w are the velocity components in the x-, y- and z-directions, K_S and K_H are the vertical and horizontal eddy diffusivity. Assuming that the stratification in the estuary is dominated by the salinity difference, i.e., $N^2 = -g\beta\frac{\partial S}{\partial z}$, we obtain from Eq. (A1)

$$\begin{aligned} \frac{\partial N^2}{\partial t} = & \underbrace{-\left(u\frac{\partial N^2}{\partial x} + v\frac{\partial N^2}{\partial y} + w\frac{\partial N^2}{\partial z}\right)}_{\text{advection}} + \underbrace{\left(g\beta\frac{\partial u}{\partial z}\frac{\partial S}{\partial x} + g\beta\frac{\partial v}{\partial z}\frac{\partial S}{\partial y} + g\beta\frac{\partial w}{\partial z}\frac{\partial S}{\partial z}\right)}_{\text{straining}} \\ & \underbrace{-g\beta\left[\frac{\partial^2}{\partial z^2}\left(K_S\frac{\partial S}{\partial z}\right) + \frac{\partial^2}{\partial z\partial x}\left(K_H\frac{\partial S}{\partial x}\right) + \frac{\partial^2}{\partial z\partial y}\left(K_H\frac{\partial S}{\partial y}\right)\right]}_{\text{diffusion}}. \end{aligned} \qquad \text{(A2)}$$

To evaluate the terms in (A2) numerically on the Arakawa C-grid used in ROMS, we rewrite the advection terms in the flux form such that the flux out of each grid-cell is identical to the flux into the adjacent cell and the sum of the grid-point values conserves the advected quantity in the finite-difference approximation. Similarly, we can rewrite the straining terms for the easy and accuracy of numerical calculations. Then Eq. (A2) becomes

$$\frac{\partial N^2}{\partial t} = \overbrace{\left[-\frac{\partial uN^2}{\partial x} + N^2\frac{\partial u}{\partial x}\right]}^{\text{term (1)}} + \overbrace{\left[-\frac{\partial vN^2}{\partial y} + N^2\frac{\partial v}{\partial y}\right]}^{\text{term (2)}} + \overbrace{\left[-\frac{\partial wN^2}{\partial z} + N^2\frac{\partial w}{\partial z}\right]}^{\text{term (3)}}$$
$$+\left[g\beta\frac{\partial}{\partial z}\left(\frac{\partial uS}{\partial x} - S\frac{\partial u}{\partial x}\right) - \text{term(1)}\right]$$
$$+\left[g\beta\frac{\partial}{\partial z}\left(\frac{\partial vS}{\partial y} - S\frac{\partial v}{\partial y}\right) - \text{term(2)}\right] \qquad \text{(A3)}$$
$$+\left[g\beta\frac{\partial}{\partial z}\left(\frac{\partial wS}{\partial z} - S\frac{\partial w}{\partial z}\right) - \text{term(3)}\right]$$
$$-g\beta\left[\frac{\partial^2}{\partial z^2}\left(K_S\frac{\partial S}{\partial z}\right) + \frac{\partial^2}{\partial z\partial x}\left(K_H\frac{\partial S}{\partial x}\right) + \frac{\partial^2}{\partial z\partial y}\left(K_H\frac{\partial S}{\partial y}\right)\right]$$

In the ROMS model which uses a terrain-following vertical coordinate, the form of the stratification equation used for the diagnostic analysis is given by

$$\frac{\partial N^2}{\partial t} = \overbrace{\frac{1}{H_Z}\left[-\frac{\partial uH_Z N^2}{\partial x} + N^2\frac{\partial uH_Z}{\partial x}\right]}^{\text{term (1)}}$$
$$+\overbrace{\frac{1}{H_Z}\left[-\frac{\partial vH_Z N^2}{\partial y} + N^2\frac{\partial vH_Z}{\partial y}\right]}^{\text{term (2)}}$$
$$+\overbrace{\frac{1}{H_Z}\left[-\frac{\partial \Omega H_Z N^2}{\partial \sigma} + N^2\frac{\partial \Omega H_Z}{\partial \sigma}\right]}^{\text{term (3)}}$$
$$+\left[\frac{g\beta}{H_Z}\frac{\partial}{\partial\sigma}\frac{1}{H_Z}\left(\frac{\partial uH_Z S}{\partial x} - S\frac{\partial uH_Z}{\partial x}\right) - \text{term(1)}\right]$$
$$+\left[\frac{g\beta}{H_Z}\frac{\partial}{\partial\sigma}\frac{1}{H_Z}\left(\frac{\partial vH_Z S}{\partial y} - S\frac{\partial vH_Z}{\partial y}\right) - \text{term(2)}\right]$$
$$+\left[\frac{g\beta}{H_Z}\frac{\partial}{\partial\sigma}\frac{1}{H_Z}\left(\frac{\partial \Omega H_Z S}{\partial \sigma} - S\frac{\partial \Omega H_Z}{\partial \sigma}\right) - \text{term(3)}\right]$$
$$-\frac{g\beta}{H_Z}\left[\frac{\partial D_\sigma}{\partial\sigma} + \frac{\partial D_X}{\partial\sigma} + \frac{\partial D_Y}{\partial\sigma}\right] \qquad \text{(A4)}$$

where σ is the vertical distance from surface as a fraction of total water depth H_Z ($-1 \le \sigma \le 0$), Ω is the vertical velocity in the s-coordinate, and D_X, D_Y and D_σ represent the horizontal and vertical diffusion terms.

Acknowledgements: We thank Bill Boicourt, Malcolm Scully and Peng Jia for helpful discussions and two reviewers for thoughtful comments. We are grateful to NSF (OCE-082543 and OCE-0961880) and NOAA (CHRP-NA07N054780191) for the financial support. This is UMCES contribution number 4566 and CHRP contribution number 150.

References

Bowden, K. F. (1953), Note on wind drift in a channel in the presence of tidal currents, *Proc. R. Soc. London, A*, *219*(1139), 426-446, doi: 10.1098/rspa.1953.0158.

Chen, S.-N., and L. P. Sanford (2009a), Axial wind effects on stratification and longitudinal salt transport in an idealized, partially mixed estuary, *J. Phys. Oceanogr.*, *39*(8), 1905-1920, doi: 10.1175/2009JPO4016.1.

Chen, S.-N., L. P. Sanford, and D. K. Ralston (2009b), Lateral circulation and sediment transport driven by axial winds in an idealized, partially mixed estuary, *J. Geophys. Res.*, *114*, C12006, doi: 10.1029/2008JC005014.

Chuang, W. S., and W. C. Boicourt (1989), Resonant seiche motion in the Chesapeake Bay, *J. Geophys. Res.*, *94*(C2), 2105-2110, doi: 10.1029/JC094iC02p02105.

Csanady, G. T. (1973), Wind-induced barotropic motions in long lakes, *J. Phys. Oceanogr.*, *3*(4), 429-438, doi: 10.1175/1520-0485(1973)003<0429:WIBMIL>2.0.CO;2.

Garvine, R. W. (1985), A simple-model of estuarine subtidal fluctuations forced by local and remote wind stress, *J. Geophys. Res.*, *90*(C6), 1945-1948, doi: 10.1029/JC090iC06p11945.

Garvine, R. W. (1995), A dynamical system for classifying buoyant coastal discharges, *Cont. Shelf Res.*, *15*(13), 1585-1596, doi: 10.1016/0278-4343(94)00065-U.

Geyer, W. R. (1997), Influence of wind on dynamics and flushing of shallow estuaries, *Estuarine Coastal Shelf Sci.*, *44*(6), 713-722, doi: doi:10.1006/ecss.1996.0140.

Goodrich, D. M., W. C. Boicourt, P. Hamilton, and D. W. Pritchard (1987), Wind-induced destratification in Chesapeake Bay, *J. Phys. Oceanogr.*, *17*(12), 2232-2240, doi: 10.1175/1520-0485(1987)017<2232:WIDICB>2.0.CO;2.

Guo, X. Y., and A. Valle-Levinson (2008), Wind effects on the lateral structure of density-driven circulation in Chesapeake Bay, *Cont. Shelf Res.*, *28*(17), 2450-2471, doi: 10.1016/j.csr.2008.06.008.

Janzen, C. D., and K. C. Wong (2002), Wind-forced dynamics at the estuary-shelf interface of a large coastal plain estuary, *J. Geophys. Res.*, *107*(C10), 3138, doi: 10.1029/2001jc000959.

Lerczak, J. A., and W. R. Geyer (2004), Modeling the lateral circulation in straight, stratified estuaries, *J. Phys. Oceanogr.*, *34*(6), 1410-1428, doi: 10.1175/1520-0485(2004)034<1410:MTLCIS>2.0.CO;2.

Lerczak, J. A., W. R. Geyer, and R. J. Chant (2006), Mechanisms driving the time-dependent salt flux in a partially stratified estuary, *J. Phys. Oceanogr.*, *36*(12), 2296-2311, doi: 10.1175/JPO2959.1.

Li, M., and L. J. Zhong (2009), Flood-ebb and spring-neap variations of mixing, stratification and circulation in Chesapeake Bay, *Cont. Shelf Res.*, *29*(1), 4-14, doi: 10.1016/j.csr.2007.06.012.

Li, M., L. Sanford, and S. Y. Chao (2005), Effects of time dependence in unstratified tidal boundary layers: Results from large eddy simulations, *Estuarine Coastal Shelf Sci.*, *62*(1-2), 193-204, doi: 10.1016/j.ecss.2004.08.017.

Li, M., L. Zhong, W. C. Boicourt, S. L. Zhang, and D. L. Zhang (2007), Hurricane-induced destratification and restratification in a partially-mixed estuary, *J. Mar. Res.*, *65*(2), 169-192.

Malone, T. C., W. M. Kemp, H. W. Ducklow, W. R. Boynton, J. H. Tuttle, and R. B. Jonas (1986), Lateral variation in the production and fate of phytoplankton in a partially stratified estuary, *Mar. Ecol. Prog. Ser.*, *32*(2-3), 149-160, doi: 10.3354/meps032149.

Marchesiello, P., J. McWilliams, and A. Shchepetkin (2001), Open boundary conditions for long-term integration of regional oceanic models, *Ocean Modell.*, *3*(1), 20, doi: 10.1016/S1463-5003(00)00013-5.

Monismith, S. (1986), An experimental-study of the upwelling response of stratified reservoirs to surface shear-stress, *J. Fluid Mech.*, *171*, 407-439, doi: 10.1017/S0022112086001507.

North, E. W., S. Y. Chao, L. P. Sanford, and R. R. Hood (2004), The influence of wind and river pulses on an estuarine turbidity maximum: Numerical studies and field observations in Chesapeake Bay, *Estuaries*, *27*(1), 132-146.

O'Donnell, J., H. G. Dam, W. F. Bohlen, W. Fitzgerald, P. S. Gay, A. E. Houk, D. C. Cohen, and M. M. Howard-Strobel (2008), Intermittent ventilation in the hypoxic zone of western Long Island Sound during the summer of 2004, *J. Geophys. Res.*, *113*, C09025, doi: 10.1029/2007JC004716.

Ralston, D. K., W. R. Geyer, and J. A. Lerczak (2008), Subtidal salinity and velocity in the Hudson River estuary: Observations and modeling, *J. Phys. Oceanogr.*, *38*(4), 753-770, doi: 10.1175/2007JPO3808.1.

Rattray, M., and D. V. Hansen (1962), A similarity solution for circulation in an estuary, *J. Mar. Res.*, *20*(2), 121-133.

Reyes-Hernández, C., and A. Valle-Levinson (2010), Wind modifications to density-driven flows in semienclosed, rotating basins, *J. Phys. Oceanogr.*, *40*, 1473-1487, doi: 10.1175/2010JPO4230.1

Sanford, L. P., K. G. Sellner, and D. L. Breitburg (1990), Covariability of dissolved-oxygen with physical processes in the summertime Chesapeake Bay, *J. Mar. Res.*, *48*(3), 567-590.

Scully, M. E. (2010), Wind modulation of dissolved oxygen in Chesapeake Bay, *Estuaries Coasts*, *33*(5), 1164-1175, doi: 10.1007/s12237-010-9319-9.

Scully, M. E., C. Friedrichs, and J. Brubaker (2005), Control of estuarine stratification and mixing by wind-induced straining of the estuarine density field, *Estuaries*, *28*(3), 321-326, doi: 10.1007/BF02693915.

Scully, M. E., W. R. Geyer, and J. A. Lerczak (2009), The influence of lateral advection on the residual estuarine circulation: A numerical modeling study of the Hudson River estuary, *J. Phys. Oceanogr.*, *39*(1), 107-124, doi: Doi 10.1175/2008jpo3952.1.

Valle-Levinson, A. (2008), Density-driven exchange flow in terms of the Kelvin and Ekman numbers, *J. Geophys. Res.*, *113*(C4), C04001, doi: 10.1029/2007jc004144.

Wang, D. P. (1979a), Subtidal sea-level variations in the Chesapeake Bay and relations to atmospheric forcing, *J. Phys. Oceanogr.*, *9*(2), 413-421, doi: 10.1175/1520-0485(1979)009<0413:SSLVIT>2.0.CO;2.

Wang, D. P. (1979b), Wind-driven circulation in the Chesapeake Bay, winter 1975, *J. Phys. Oceanogr.*, *9*(3), 564-572, doi: 10.1175/1520-0485(1979)009<0564:WDCITC>2.0.CO;2.

Wang, D. P., and A. J. Elliott (1978), Non-tidal variability in Chesapeake Bay and Potomac River - evidence for nonlocal forcing, *J. Phys. Oceanogr.*, *8*(2), 225-232, doi: 10.1175/1520-0485(1978)008<0225:NTVITC>2.0.CO;2.

Warner, J. C., W. R. Geyer, and J. A. Lerczak (2005), Numerical modeling of an estuary: A comprehensive skill assessment, *J. Geophys. Res.*, *110*, C05001, doi: 10.1029/2004JC002691.

Wilson, R. E., R. L. Swanson, and H. A. Crowley (2008), Perspectives on long-term variations in hypoxic conditions in western Long Island Sound, *J. Geophys. Res.*, *113*, C12011, doi: 10.1029/2007JC004693.

Winant, C. (2004), Three-dimensional wind-driven flow in an elongated, rotating basin, *J. Phys. Oceanogr.*, *34*(2), 462-476, doi: 10.1175/1520-0485(2004)034<0462:TWFIAE>2.0.CO;2.

Wong, K. C. (1994), On the nature of transverse variability in a coastal-plain estuary, *J. Geophys. Res.*, *99*(C7), 14209-14222, doi: 10.1029/94JC00861

Wong, K. C., and J. E. Moses-Hall (1998), On the relative importance of the remote and local wind effects to the subtidal variability in a coastal plain estuary, *J. Geophys. Res.*, *103*(C9), 18393-18404, doi: 10.1029/98JC01476.

Wong, K. C., and A. Valle-Levinson (2002), On the relative importance of the remote and local wind effects on the subtidal exchange at the entrance to the Chesapeake Bay, *J. Mar. Res.*, *60*(3), 477-498.

Zhong, L., and M. Li (2006), Tidal energy fluxes and dissipation in the Chesapeake Bay, *Cont. Shelf Res.*, *26*(6), 752-770, doi: 10.1016/j.csr.2006.02.006.

Zhong, L., M. Li, and M. G. G. Foreman (2008), Resonance and sea level variability in Chesapeake Bay, *Cont. Shelf Res.*, *28*(18), 2565-2573, doi: 10.1016/j.csr.2008.07.007.

Tables

Table 3-1. Wind Experiments. Idealized winds are applied from day 25 to day 27.5.

Wind Stress	Wind Speed	$Ke = 0$ [1]		$Ke = 4.26$		$Ke = 2.06$		$Ke = 6.82$	
(Pa)	(m/s)	No.	W [2]	No.	W	No.	W	No.	W
without wind									
0.00	0.00	**1**	0	**18**	0	**35**	0	**52**	0
down-estuary wind									
-0.005	-2.35	**2**	-0.19	**19**	-0.19	**36**	-0.21	**53**	-0.17
-0.01	-3.20	**3**	-0.38	**20**	-0.39	**37**	-0.41	**54**	-0.35
-0.02	-4.34	**4**	-0.77	**21**	-0.77	**38**	-0.82	**55**	-0.69
-0.03	-5.17	**5**	-1.17	**22**	-1.16	**39**	-1.24	**56**	-1.04
-0.05	-6.41	**6**	-1.96	**23**	-1.94	**40**	-2.08	**57**	-1.74
-0.07	-7.37	**7**	-2.79	**24**	-2.72	**41**	-2.91	**58**	-2.45
-0.15	-10.03	**8**	-6.10	**25**	-6.04	**42**	-6.28	**59**	-5.41
-0.25	-12.27	**9**	-10.4	**26**	-10.1	**43**	-10.5	**60**	-9.15
up-estuary wind									
0.005	2.35	**10**	0.19	**27**	0.19	**44**	0.21	**61**	0.17
0.01	3.20	**11**	0.38	**28**	0.39	**45**	0.42	**62**	0.35
0.02	4.34	**12**	0.76	**29**	0.78	**46**	0.83	**63**	0.70
0.03	5.17	**13**	1.12	**30**	1.16	**47**	1.24	**64**	1.06
0.05	6.41	**14**	1.84	**31**	1.94	**48**	2.05	**65**	1.78
0.07	7.37	**15**	2.56	**32**	2.71	**49**	2.84	**66**	2.50
0.15	10.03	**16**	5.34	**33**	5.67	**50**	5.99	**67**	5.33
0.25	12.27	**17**	8.81	**34**	9.32	**51**	9.84	**68**	8.94

[1] Ke is Kelvin number. When $Ke = 0$, rotation effect is not considered.
[2] W is Wedderburn number.

Figures

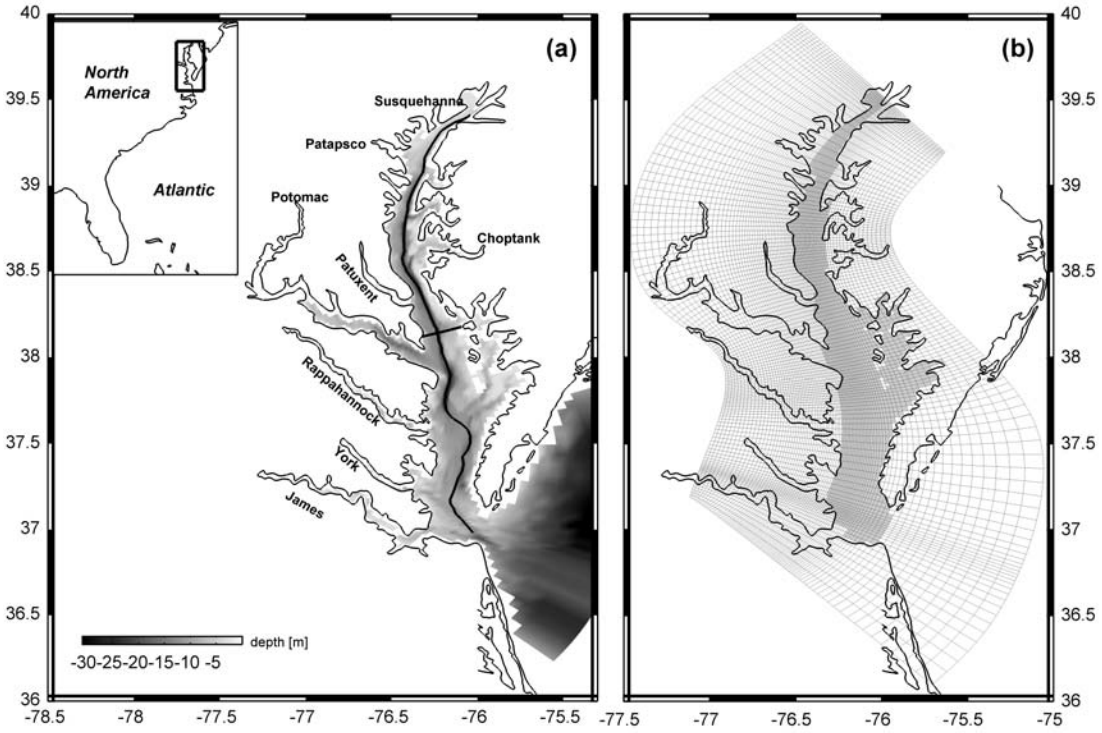

Figure 3-1. (a) Bathymetry of Chesapeake Bay and its adjacent coastal area. Major tributaries are marked. Depths are in meters. The insert indicates the geographic location of Chesapeake Bay in North America. The solid lines represent the along-channel and cross-channel transects. (b) ROMS grid for Chesapeake Bay Model. The shaded areas are used for calculating volume-averaged stratification in later analysis.

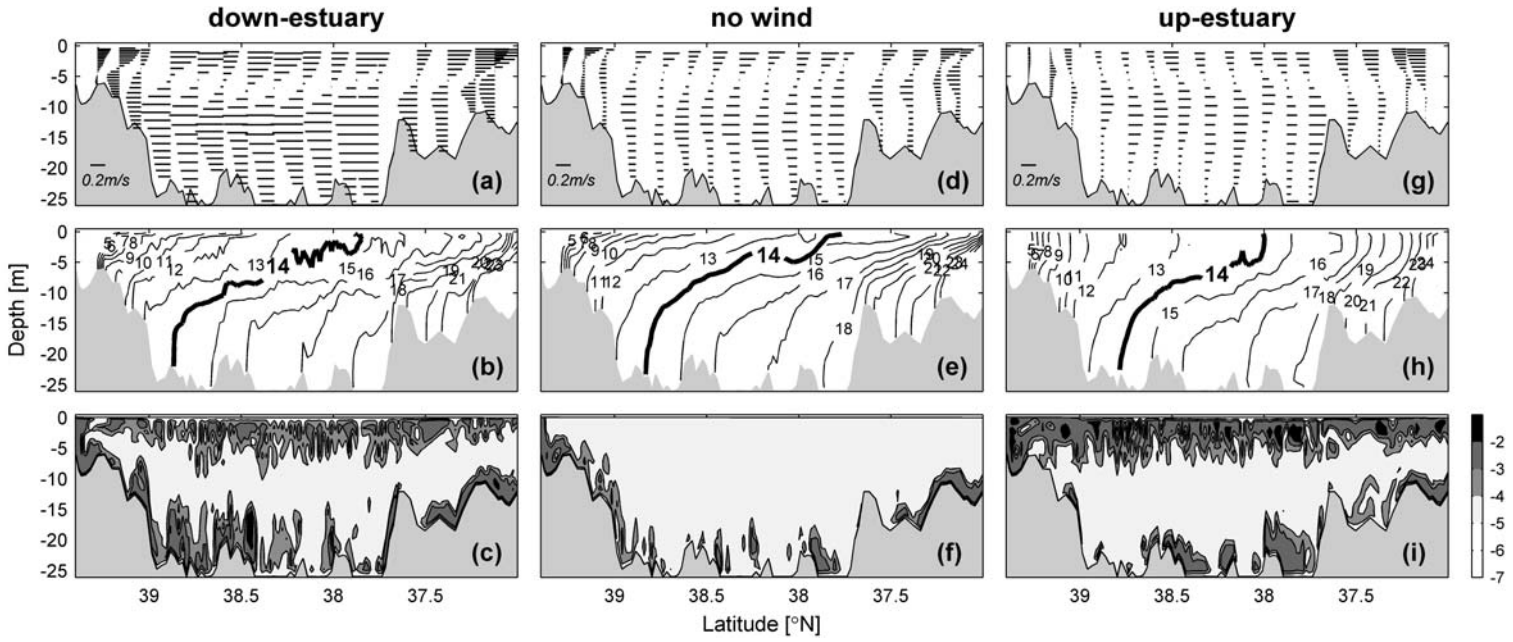

Figure 3-2. Along-channel distributions of (a/d/g) subtidal currents, (b/e/h) salinity and (c/f/i) the logarithm of eddy diffusivity at the time of peak wind stress for Run 7 (left column), Run 1 (middle column) and Run 15 (right column). Coriolis force is switched off in these runs. The 14-psu isohalines are marked as thick lines.

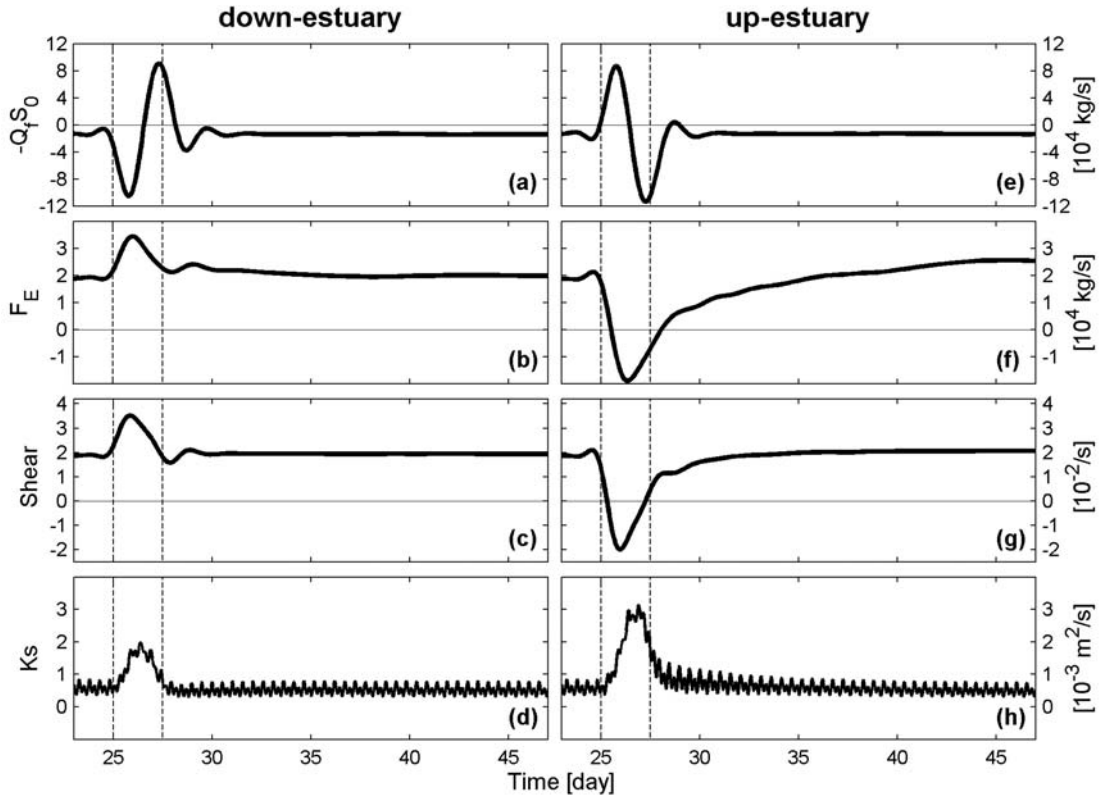

Figure 3-3. Time series of (a/e) subtidal salt flux due to barotropic transport ($-Q_fS_0$), (b/f) shear dispersion (F_E), (c/g) averaged shear in the along-channel current, and (d/h) diffusivity (Ks) for Run 7 (down-estuary wind, left column) and Run 15 (up-estuary wind, right column), in the absence of rotational effect. Positive flux corresponds to the landward flux. The two dashed lines mark the wind event.

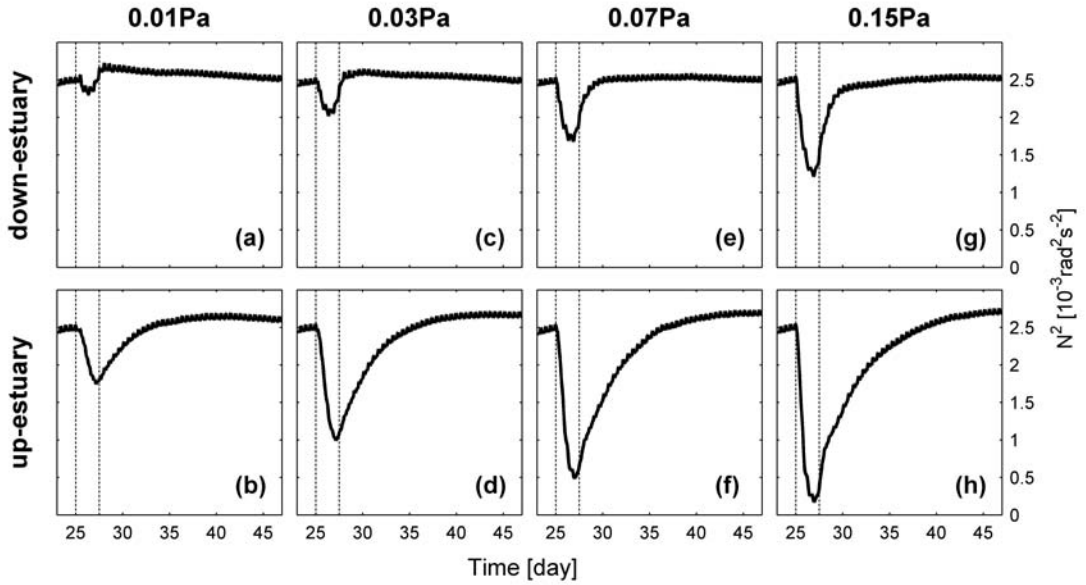

Figure 3-4. Time series of volume-averaged stratification for down-estuary and up-estuary winds at different wind-stress magnitudes and in the absence of rotational effects. The two dashed lines mark the wind event.

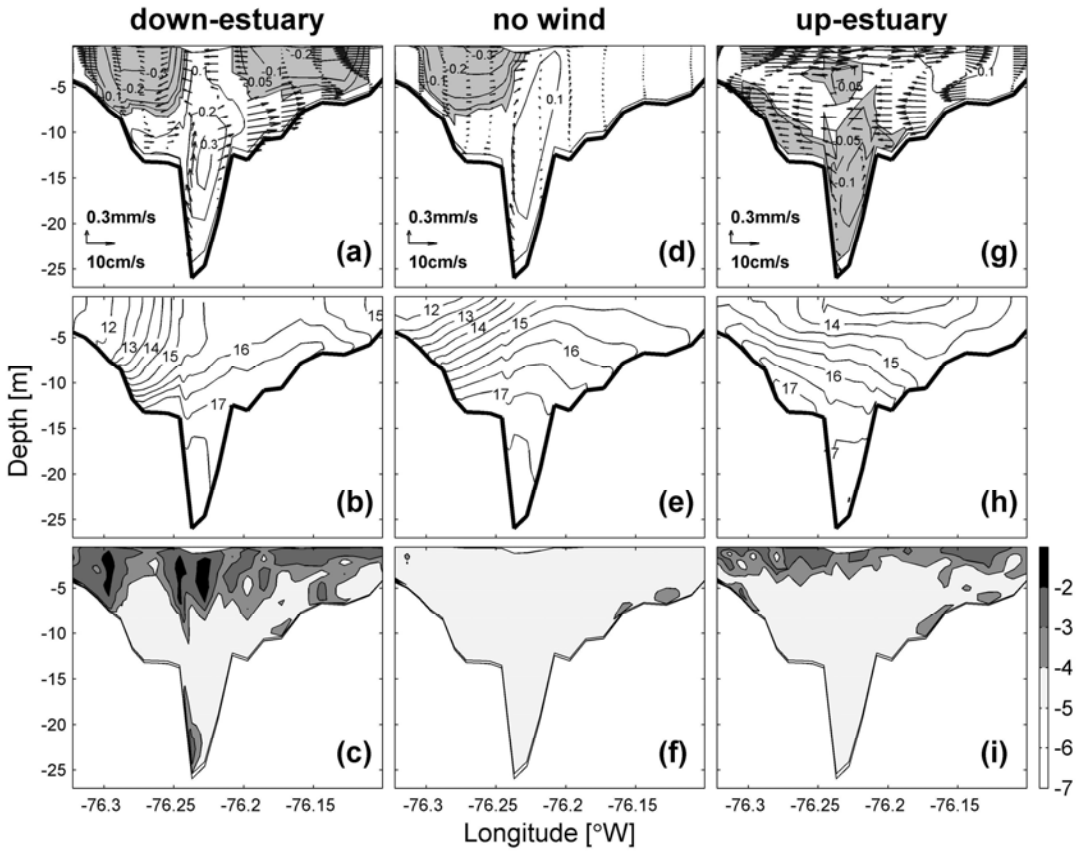

Figure 3-5. Distributions of (a/d/g) along-channel current (contours) and cross-channel velocity vectors (arrows), (b/e/h) salinity, and (c/f/i) the logarithm of eddy diffusivity in a mid-bay section at the time of peak wind stress (day 26.25) for Run 24 (left column), Run 18 (middle column) and Run 32 (right column). The cross-section is looking up-estuary, and negative flows pointing seaward are shaded in gray. The Coriolis force is included in these runs.

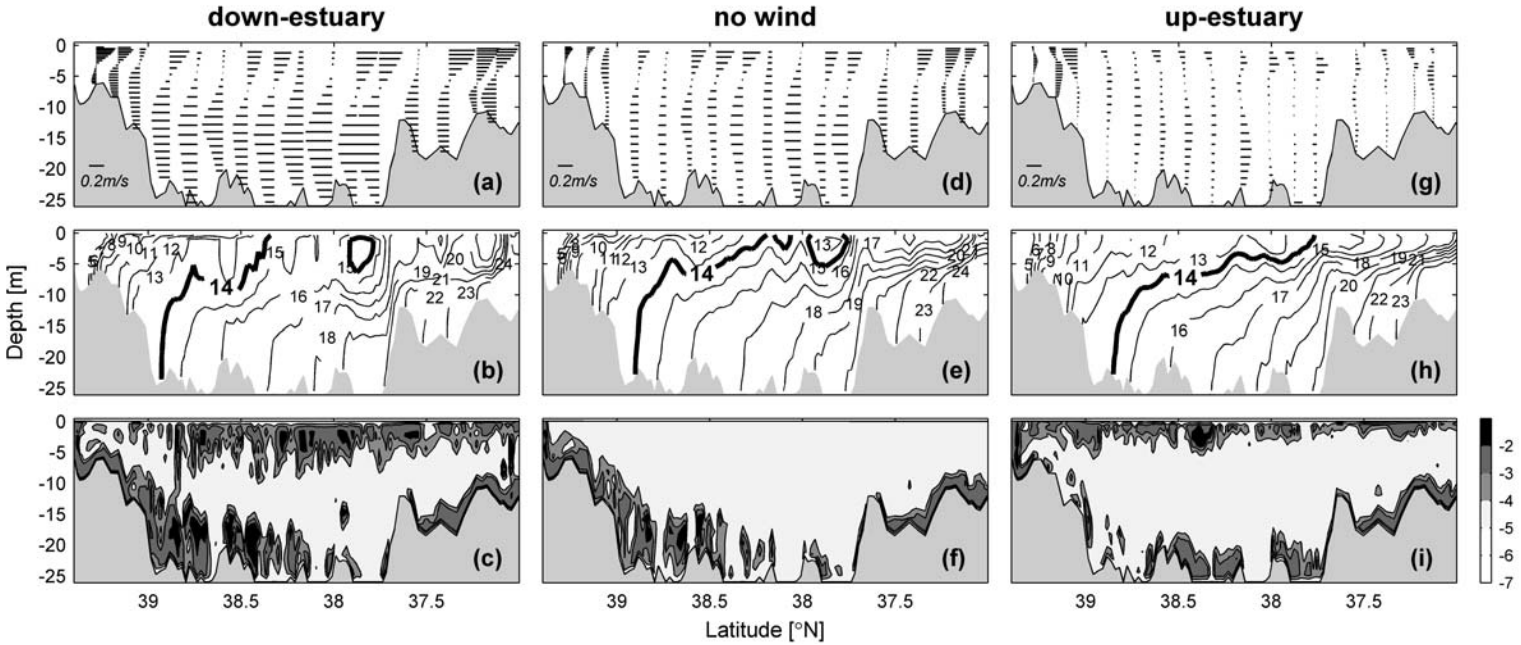

Figure 3-6. Along-channel distributions of (a/d/g) subtidal currents, (b/e/h) salinity and (c/f/i) the logarithm of eddy diffusivity at the time of maximum wind stress for Run 24 (left column), Run 18 (middle column), and Run 32 (right column). Coriolis force is switched on in those runs. The 14-psu isohalines are marked as thick lines.

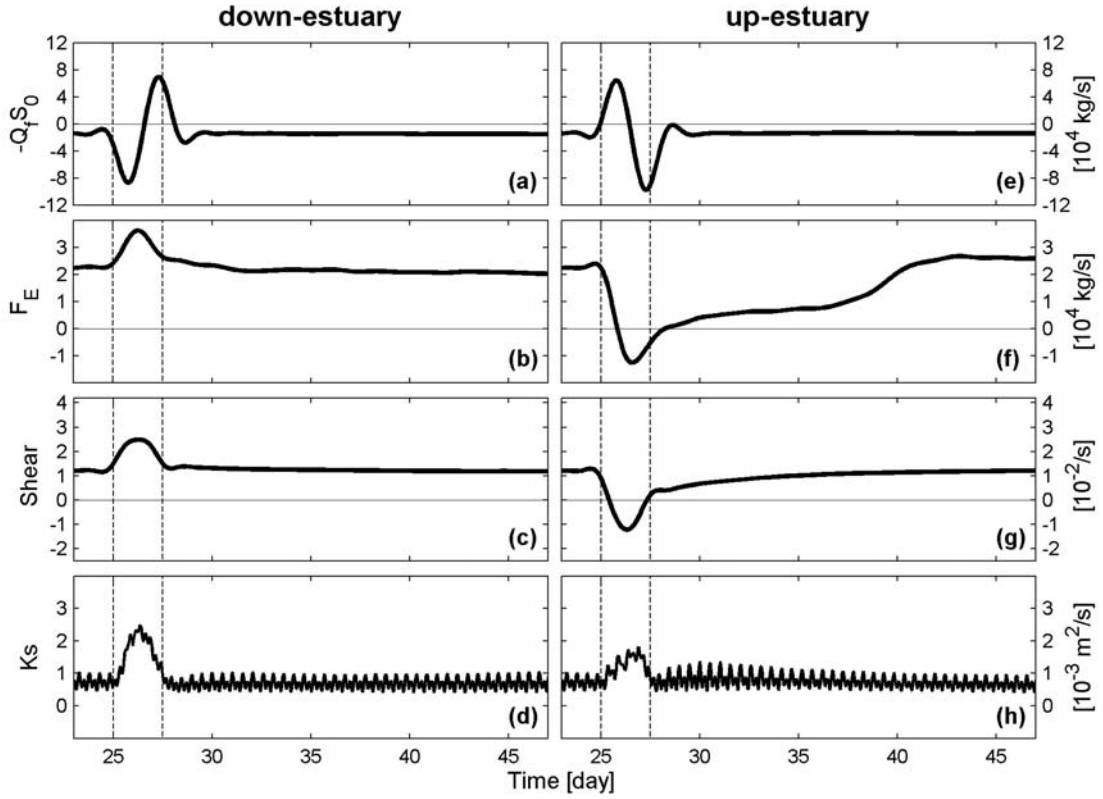

Figure 3-7. Time series of (a/e) subtidal salt flux due to barotropic transport ($-Q_fS_0$), (b/f) shear dispersion (F_E), (c/g) averaged shear in the along-channel current, and (d/h) diffusivity (Ks) for Run 24 (down-estuary wind, left column) and Run 32 (up-estuary wind, right column), in the presence of rotational effect. Positive flux corresponds to the landward flux. The two dashed lines mark the wind event.

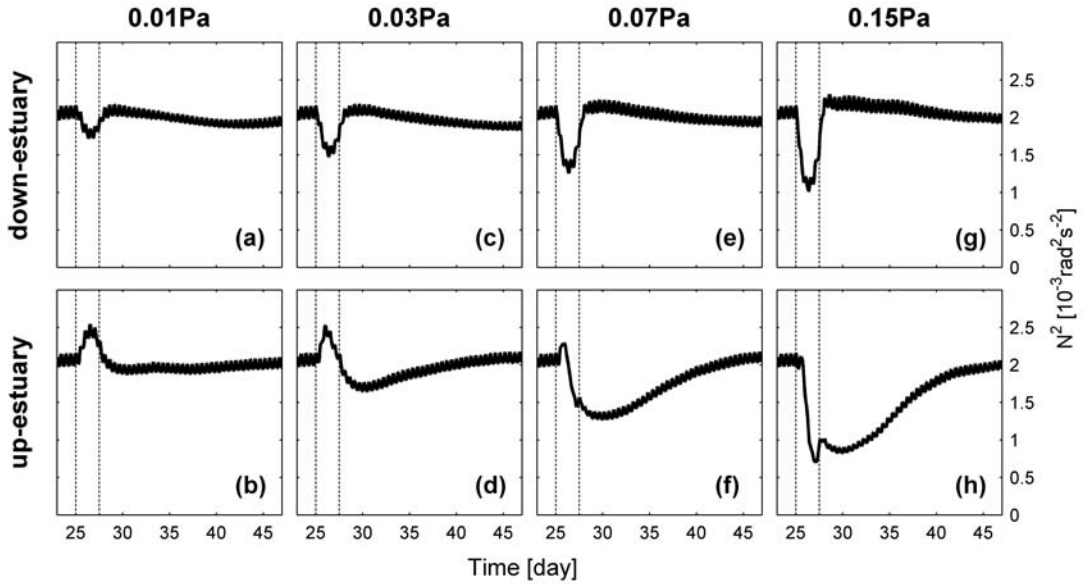

Figure 3-8. Time series of volume-averaged stratification for down-estuary and up-estuary winds at different wind-stress magnitudes and in the presence of rotation. The time period between the two dashed lines marks the wind event.

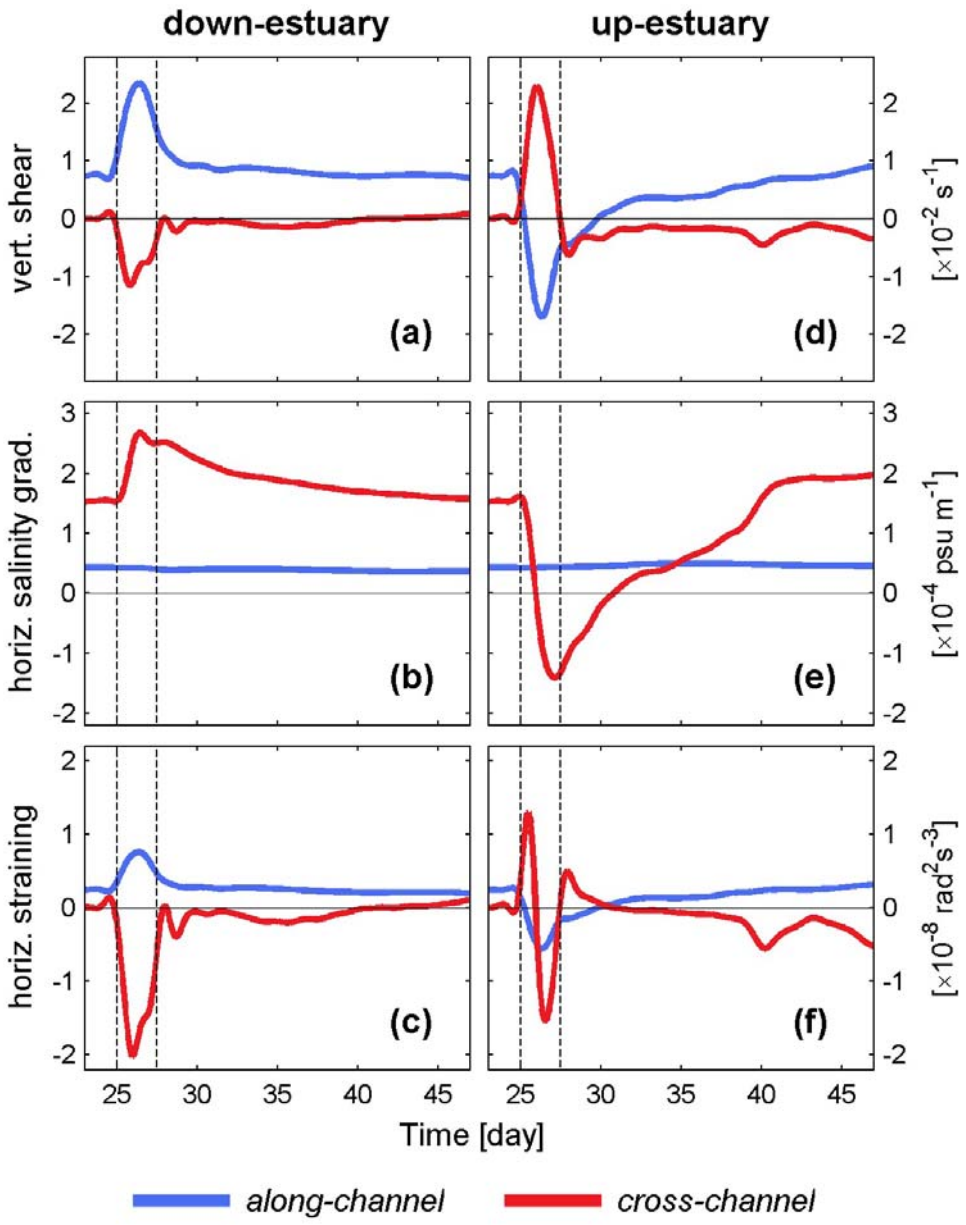

Figure 3-9. Time series of (a/d) vertical shear, (b/e) horizontal salinity gradient and (c/f) horizontal straining for the down- (left column) and up-estuary (right column) winds with the maximum stress of 0.07 Pa. Each variable is decomposed into along-channel (blue) and cross-channel (red) components, and then detided by a 34-hr low-pass filter. The time period between the two dashed lines marks the wind event.

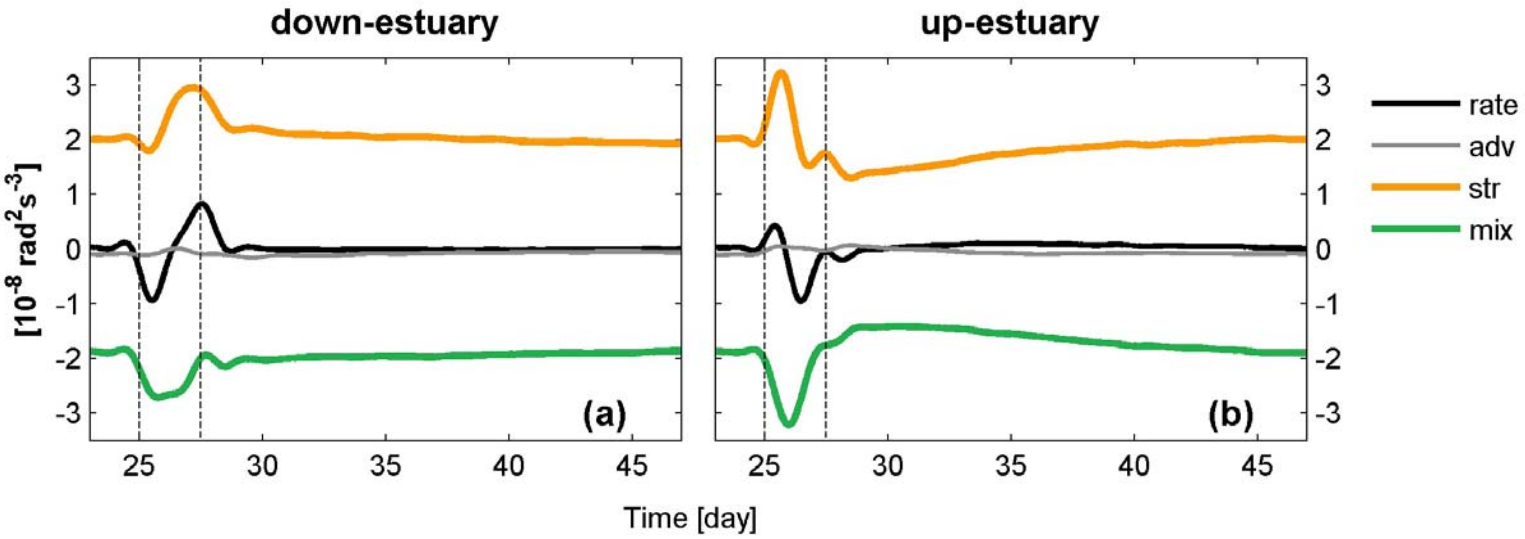

Figure 3-10. Time series of the terms in the volume-averaged stratification equation: time-change-rate (black), advection (grey), straining (orange) and mixing (green). Positive value represents the tendency to increase stratification. The left panel is obtained from Run 24 (down-estuary wind) and the right panel from Run 32 (up-estuary wind). The time period between the two dashed lines marks the wind event.

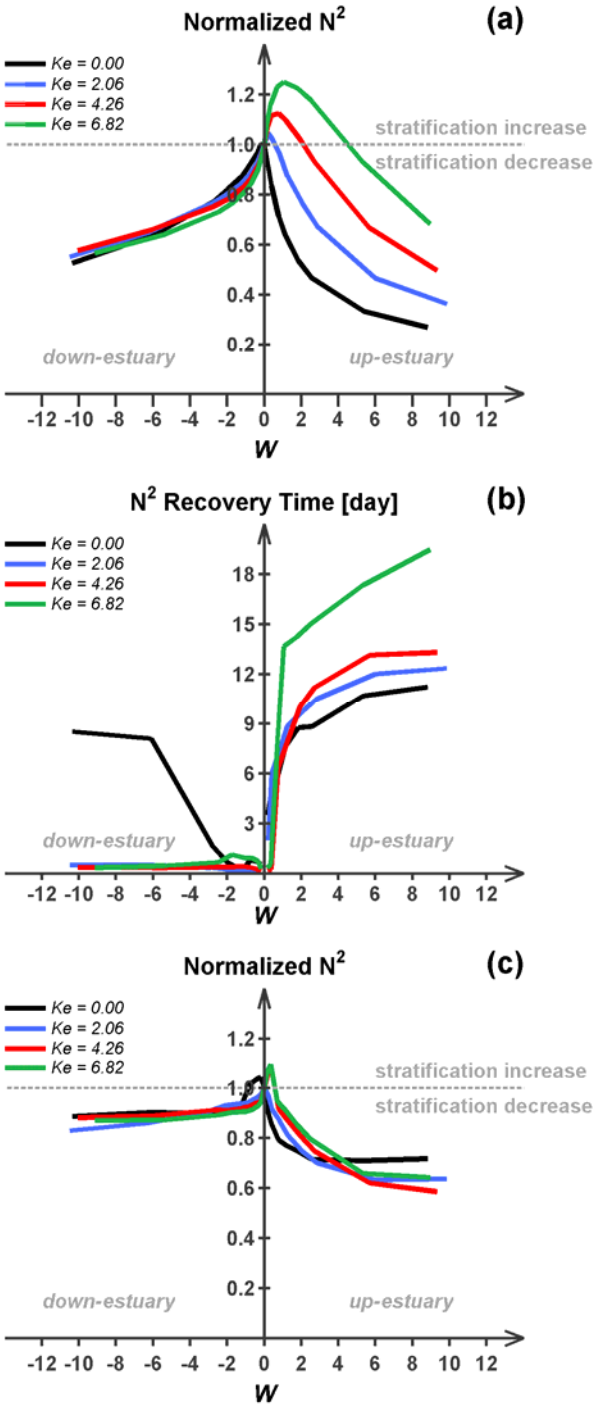

Figure 3-11. (a) Stratification change during the wind perturbation, (b) stratification recovery time, and (c) mean stratification during the recovery stage as functions of Wedderburn (*W*) and Kelvin numbers (*Ke*). Positive Wedderburn number corresponds to up-estuary wind. The stratification is averaged over the wind event in panel (a) and over the recovery period in panel (c), and then normalized against its pre-wind level, so that values below 1 indicate stratification reduction. The recovery time is defined as the time required for the volume-averaged stratification to resume 95% of its pre-wind level after the passage of the wind.

Chapter 4: What Regulates the Seasonal Cycle of Dissolved Oxygen in Chesapeake Bay?

Abstract

A coupled hydrodynamic-biogeochemical model is developed to simulate the seasonal cycle of dissolved oxygen in Chesapeake Bay and investigate physical and biogeochemical processes which regulate summer hypoxia in the estuary. Diagnostic analysis of the oxygen budget for the bottom water reveals a balance between physical transport and biological consumption. In addition to the vertical diffusive flux, the along-channel and cross-channel advective fluxes are found to be important contributors to supply oxygen to the bottom water. While the vertical diffusive oxygen flux varies over the spring-neap tidal cycle and is enhanced during wind events, the advective oxygen fluxes show long-term averages due to the gravitational estuarine circulation but display strong oscillations due to wind-driven circulations. Winds from south weaken the landward bottom flow and generate a clockwise lateral circulation to eject hypoxic water onto the shallow western shoal and inject well-oxygenated surface water into the bottom layer, thereby reducing the along-channel advective flux and increasing the cross-channel advective flux. In contrast, winds from north amplify the along-channel flux but reduce the cross-channel flux. It is found that water column respiration contributes to about 74% of the total biological consumption and sediment oxygen demand contributes 26%. Sensitivity-analysis model runs are conducted to further quantify the effects of river flow, winds, water column respiration and sediment oxygen demand on the hypoxic volume in the estuary.

1. Introduction

Oxygen depletion due to nutrient enrichment is a widespread phenomenon that is growing globally [*Diaz*, 2001]. It is widely believed that anthropogenic nutrient enrichment fuels algal production and causes oxygen depletion from bottom waters [*Diaz and Rosenberg*, 1995]. Hypoxia is usually defined as dissolved oxygen (DO) concentrations falling below approximately 2 mg L^{-1} that interrupts normal metabolism of marine organisms. Two principal factors that are widely believed to control the summer hypoxia are water-column stratification, which isolates the bottom DO exchange from oxygen-rich surface water, and decomposition of organic matter in the bottom water, which reduces oxygen levels.

Many U.S. coastal and estuarine areas suffer from seasonal hypoxia including Chesapeake Bay [*Kemp et al.*, 2009]. Chesapeake Bay is a temperate, partially-mixed estuary, and it receives more than 60% of the total freshwater input from Susquehanna River at the northern end. As spring freshet strengthens stratification, warming temperature stimulates respiration of sinking organic matter that has been accumulated from spring blooms and causes oxygen depletion in the deep portion of the estuary in summer [*Taft et al.*, 1980]. Seasonal hypoxia is mainly caused by the imbalance between physical supply and biogeochemical consumption [*Kemp et al.,* 1992]. In additional to seasonal cycle, there have been large interannual variations of the hypoxic volume over the past couple of decades: with severe hypoxia found during wet years and mild hypoxia found during dry years [*Hagy et al.*, 2004]. Large

inter-annual fluctuations in river flow result in highly variable nutrient loading and estuarine stratification. In addition, shifts in wind regimes also exert more subtle controls [*Scully et al.*, 2010a]. A major impediment to developing successful nutrient reduction strategy is the lack of adequate understanding of how the river flow and winds influence the physical and biological controls on hypoxia.

Several physical processes were suggested essential to oxygen supply in the Bay, but their contributions to oxygen balance remain unclear. The traditional view of oxygen balance during the summertime is between diapycnal exchange and the oxygen utilization [*Taft et al.*, 1980; *Officer et al.*, 1984]. *Kemp et al.,* [1992] conducted oxygen budget analysis in the mesohaline region using field measurements. They showed that longitudinal oxygen transport from lower bay region is also important to oxygen replenishment in the middle bay. Other studies also emphasized the along-channel transport of oxygen in estuarine environment [*Kuo and Neilson*, 1987; *Boicourt et al.*, 1992]. Moreover, observational evidences [*Malone et al*., 1986, *Sanford et al.*, 1990] and numerical simulations [*Scully et al.*, 2010b] suggest significant wind-driven lateral motions are effective to supply oxygen into the subpycnal waters. The lateral flows can advect hypoxic water onto shallow shoals where it mixes with well-oxygenated surface water due to wind mixing. Subsequent re-injection of the oxygenated water back to the bottom water thus raises the dissolved oxygen concentration there. However, it remains unclear if the wind-driven mixing on the shallow shoal or the wind-induced upwelling and ventilation is responsible for the recharge of oxygen to the bottom water.

In additional to the physical controls, biogeochemical controls are split into pelagic and benthic respiration, but it is still unclear whether both are equally important in driving summer hypoxia in the Bay. The relative contributions of pelagic and benthic respiration were shown to vary with water depth and season [*Kemp et al.*, 1992]. In Chesapeake Bay, previous studies attributed most oxygen utilization either to pelagic respiration [i.e. *Taft et al.*, 1980; *Scully et al.*, 2010b] or benthic consumption [i.e. *Officer et al.*, 1984].

The physical and biological controls of DO can not be understood by observations alone; a coupled hydrodynamic-biogeochemical model is needed to eclucidate the mechanism. Water quality models that simulate complex oxygen kinetics as a stoichiometric relation to nutrient cycles did not yield a simple correlation between climatic forcing and hypoxic volume. For example, the water quality model that involves full biogeochemistry and over 100 parameters has been used to simulate hypoxia for Chesapeake Bay [*Cerco and Cole*, 1993; *Cerco*, 1995]. Although the model does a good job in reproducing the seasonal cycle of hypoxia it has difficulties in capturing the interannual variability.

Models that couple full three-dimensional hydrodynamic models with simplified parameterizations of biogeochemical processes may offer a better opportunity to illuminate the effects of physical processes on the seasonal cycle and interannual variability of hypoxia. Recently, in order to gain insights into the role of stratification

and circulation for the development of hypoxia on the Texas–Louisiana continental shelf, *Hetland and DiMarco* [2009] parameterized biological activity through various forms of respiration rather than using a complex biogeochemical model. In the attempt to isolate physical processes that control hypoxia, their study provides a new framework to employ simplified biogeochemistry in a fully prognostic three-dimensional hydrodynamic model. Similarly, in a recent study in Chesapeake Bay, *Scully* [2010b] assumed constant respiration in the water column, and used this oxygen model to explain the mechanism that governs replenishment of oxygen by wind-induced mixing and lateral motions.

In this chapter, we derive a model that includes a complete DO balance with oxygen source and sink terms prescribed via data-based parameterization for Chesapeake Bay. This oxygen model is coupled with a three-dimensional hydrodynamic model to investigate the seasonal oxygen cycle. Our goal is to identify the key physical and biogeochemical controls of dissolved oxygen in the Bay. The chapter is organized as follows: Section 2 describes the configuration of the coupled hydrodynamic-dissolved-oxygen model and compares model results with observations. In Section 3, we conduct budget analysis of seasonal oxygen balance in the lower layer and address the key physical and biogeochemical controls. The mechanisms of the physical controls are discussed in Section 4. In Section 5, we conduct sensitivity runs to examine the response of hypoxia volume to the variations in river flow, wind speed and biogeochemical consumption. Finally, the conclusions are given in Section 6.

2. Model description

In this section, we describe the hydrodynamic and dissolved-oxygen models and the setup of hindcast model simulations.

a. Hydrodynamic model

The three-dimensional hydrodynamic model is an implementation of the Regional Ocean Modeling System [ROMS; *Haidvogel et al.*, 2000] for Chesapeake Bay [*Li et al.*, 2005]. The model has been validated against a wide range of observational data and has shown considerable capability in reproducing estuarine dynamics at tidal, synoptic and seasonal time-scales [*Li et al.*, 2005; *Zhong and Li*, 2006; *Li et al.*, 2007; 2009]. Here we use a finer-resolution version of this model with 160×240 grid points in the horizontal direction (about ~500 m grid size) and 20 layers in the vertical direction (Fig. 1). A quadratic stress is exerted at the bed, assuming that the bottom boundary layer is logarithmic over a roughness height of 0.5 mm (see Xu *et al.*, 2002). The vertical eddy viscosity and diffusivity are computed using the *k-kl* turbulence closure scheme [*Warner et al.*, 2005] with the background diffusivity and viscosity set at 5×10^{-6} m^2s^{-1}.

The hydrodynamic model is forced by freshwater discharge at river heads, by tidal and nontidal elevations at the offshore boundary, and by wind, heat, and

freshwater fluxes across the air-sea surface. At the offshore open boundary, we employ a Chapman's condition for surface elevation, a Flather's condition for barotropic velocity, an Orlanski-type radiation condition for baroclinic flow and a combination of radiation condition and nudging for tracers (with a relaxation time scale of 1 day) [*Marchesiello et al.*, 2001]. Tidal forcing at the open ocean boundary consists of 10 constituents (M2, S2, N2, K2, K1, O1, P1, Q1, Mf, and Mm) linearly interpolated from the Oregon State University global inverse tidal model of TPXO7 [*Egbert et al.*, 1994; *Egbert and Erofeeva*, 2002]. Nontidal water elevations were acquired from detided observations at NOAA Duck, NC station. Salinity and temperature at the oceanic boundary are obtained from monthly Levitus climatology [*Levitus*, 1983]. At the riverine boundaries of 8 major tributaries, daily discharge along with zero salinity and seasonal water temperature are prescribed using USGS and Chesapeake Bay Program (CBP) monitoring data. Atmospheric forcing is applied via standard bulk formulae [*Fairall et al*., 2003] to North America Regional Reanalysis (NARR) from National Center for Environmental Prediction products [*Mesinger et al.*, 2006], including 3-hourly winds, net shortwave and downward longwave radiation, air temperature, relative humidity, and pressure. In addition, Chesapeake Bay Program monitored surface water temperature throughout the Bay, and we produced a SST field based on linear interpolation of monitoring data from 23 stations along the Bay. Modeling SST is relaxed toward this temperature field with a fast time scale of 6 hours.

b. Oxygen model

The governing equation of dissolved oxygen (Ox) is given by

$$\frac{\partial Ox}{\partial t} = \overbrace{-u\frac{\partial Ox}{\partial x}}^{\text{longitudinal advection}} \overbrace{-\left(v\frac{\partial Ox}{\partial y} + w\frac{\partial Ox}{\partial z}\right)}^{\text{lateral advection}} + \overbrace{\frac{\partial}{\partial x}\left(K_H\frac{\partial Ox}{\partial x}\right) + \frac{\partial}{\partial y}\left(K_H\frac{\partial Ox}{\partial y}\right)}^{\text{horizontal diffusion}} + \overbrace{\frac{\partial}{\partial z}\left(K_V\frac{\partial Ox}{\partial z}\right)}^{\text{vertical diffusion}}$$
$$+ \underbrace{\frac{K_O}{\Delta z_S}\left(O_{sat} - Ox\right)}_{\text{air-sea exchange}} + \underbrace{\frac{PhP}{Z_{euphotic}}}_{\text{phytoplankton production}} + \underbrace{WCR}_{\text{water column respiration}} + \underbrace{\frac{SOD}{\Delta z_b}}_{\text{sediment oxygen demand}} \quad (1)$$

where x-, y- and z- stands for the along-channel, cross-channel and vertical directions, Ox is the dissolved oxygen concentration ($\mathrm{mmol\,m^{-3}}$), O_{sat} is the saturation concentration of oxygen ($\mathrm{mmol\,m^{-3}}$), K_H and K_V are the horizontal and vertical diffusivities ($\mathrm{m^2\,s^{-1}}$), K_O is the air-sea exchange coefficient for oxygen ($\mathrm{m\,s^{-1}}$), and Δz_S , Δz_b and $Z_{euphotic}$ are the thicknesses of model surface layer, model bottom layer and euphotic layer (m), respectively. On the right-hand side of Eq. (1), the first four terms are dissolved oxygen fluxes due to physical advective and diffusive processes, the fifth term is the air-sea gas exchange, while terms 6-8 represent oxygen production and consumption due to biogeochemical processes. Term PhP is the total phytoplankton production in the euphotic layer ($\mathrm{mmolO_2\,m^{-2}\,day^{-1}}$), WCR is the water column respiration ($\mathrm{mmolO_2 m^{-3}\,day^{-1}}$), and SOD is the sediment oxygen demand ($\mathrm{mmolO_2\,m^{-2}\,day^{-1}}$).

For the air-sea exchange term, the exchange coefficient K_O is prescribed via the widely used *Wanninkhof* relationship [1992], which applies a quadratic dependency of gas exchange on the wind speed,

$$K_O = 0.31 u_{10}^2 \sqrt{\frac{660.0}{Sc_{Ox}}} \tag{2}$$

and the saturation concentration O_{sat} is calculated using *Garcia and Gordon* equation [1992],

$$Ox_{sat} = \frac{1mol}{22.9316 \times 10^{-3} m^3} C_* \tag{3}$$

where u_{10} is wind speed at 10-m height ($\mathrm{m\,s^{-1}}$), Sc_{Ox} the temperature-dependent Schmidt number of oxygen, and C^* the solubility of oxygen at the temperature of equilibrium with the atmospheric pressure at 1 atm [$\mathrm{mL\,L^{-1}}$].

For the phytoplankton production in the Bay, *Smith and Kemp* [1995] measured the net rates at three stations between 1989 and 1991 and showed that *PhP* is related to daily solar radiation and *in-situ* temperature. They further developed three empirical equations of *PhP* for each station. To quantify the overall phytoplankton

production rate, we lump the data from all stations into one set and fit in a multi-linear regression relation,

$$PhP = 31.25 \times (1.0101 + 0.0314PAR + 0.1966T) \quad (4)$$

where PAR is photosynthetically available radiation (Ein m^{-2} d^{-1}), and T is the water column temperature (^{o}C). The predicted *PhP* values are in good agreement with the observational data with R^2 = 0.54 and the regression slope close to the 1:1 ratio line (Fig. 3a).

Observations in the Bay suggest that *WCR* is characterized by strong seasonality, with peak rates coinciding with summer temperature maximum [*Kemp et al.*, 1992]. Water temperature is suggested as an important controlling factor [*Sampou and Kemp*, 1994]. *Smith and Kemp* [1995] also measured planktonic respiration rates at three stations and provided temperature-dependent formula for each. To parameterize the bay-wide *WCR* for our model, we combine their measurements and fit in a similar exponential function

$$WCR = 3.3 \times \exp^{0.0715T} \quad (5)$$

where T is the ambient water column temperature (^{o}C). The comparison between the predicted and observed values is shown in Figure. 3b with the regression coefficient R^2 = 0.42.

SOD in the Bay is found to be strongly dependent on temperature, with the Q_{10} factor (defined as a unitless factor by which a rate increases by the same multiple for every 10°C rise in temperature) in the range of 1.5 to 3.5 [*Cowan and Boynton*, 1996; *Boynton and Bailey*, 2008]. In addition, when the dissolved oxygen concentration is low, *SOD* becomes depressed due to lack of sources to support aerobic reparation [*Cowan and Boynton*, 1996; *Boynton and Bailey*, 2008]. By analyzing the sediment flux data from GONZO dataset over the same period (Walter Boynton, personal communication), we construct an empirical function via Q_{10}-law to describe the temperature dependence and Michaelis–Menten kinetics for DO limitation,

$$SOD = 9.90 \times 1.7845^{T/10^{o}\mathrm{C}} \times \left(\frac{Ox}{Ox + 1.89\mathrm{mg\,L^{-1}}} \right) \tag{6}$$

where T is the ambient water column temperature (^{o}C). The comparison between predicted and observed values shows the data linearly fall into the region of best fit with $R^2 = 0.55$ (Fig. 3c). This parameterization is similar to the empirical formula of *SOD* obtained by *Hetland and DiMarco* [2009] for the Gulf of Mexico.

Since most of the observational data used for constructing the empirical functions of *PhP*, *WCR* and *SOC* were obtained during 1989-1991, we have selected year 1989 as the first test for the model simulation. To run the coupled hydrodynamic-dissolved-oxygen model, we need to prescribe the boundary and initial conditions. Figures 2a shows the time series of annual river flow from two major tributaries. The annual

mean discharge is about 1800 m^3s^{-1} and approaches the long-term average, but the seasonal variation is distinct. The freshwater discharge from Susquehanna River is abnormally weak during winter-spring period but has three late peaks from March to June. Figure 2b shows weekly mean wind vectors in 1989 at the NARR node near Patuxent River Navy Station. The prevailing winds were southwestward during spring and winter, whereas northward and northeastward winds were dominant during summer. The boundary conditions for the dissolved oxygen are the saturation level at river ends and the seasonal climatological means at the open ocean boundary. *PAR* is obtained from daily observations at Horn Point Laboratory (Fig. 2c) [*Fisher et al.*, 2003] and $Z_{euphotic}$ is estimated using the secchi-depth measurements from the CBP (Chesapeake Bay Program) cruises. For the initial condition, we prescribe sea level, velocity, temperature, salinity and oxygen fields at the beginning of 1989. The water surface is set to the mean sea level and the velocity is assumed to be zero. The initial temperature and salinity fields are acquired from the end of a hydrodynamic run for year 1988. The initial oxygen distribution is statistical interpolated from the CBP cruise data.

3. Oxygen seasonal cycle and budget analysis

The coupled hydrodynamic-dissolved oxygen model captures well the seasonal cycle of dissolved oxygen and spatial distributions of hypoxic water in Chesapeake Bay, as shown in Figs. 4 and 5. To plot the annual time series of bottom DO, we have selected four monitoring stations along the main stem of the Bay: CB3.3C, CB4.4,

CB5.3 and CB6.2. The bottom DO at all the four stations follow a well-defined seasonal cycle with the annual minimum reached during the summer. Hypoxia develops at CB3.3C, CB4.4 and CB5.3 and lasts for 2-3 months whereas DO mostly stays above the hypoxic level at the lower-bay station CB 6.2. The predicted DO time series is in good agreement with the observations: the model skill is 0.92, 0.98, 0.98, 0.96 (see *Li et al.*, 2005, a score of 1.0 means a perfect agreement between the data and model predictions), and the root-mean-square error is 2.2, 1.1, 1.1, 1.3 mg L^{-1} for the 4 stations.

Figure 5 shows the snapshots of dissolved oxygen in the along-channel section (see Fig 1c for location). Low DO water mainly occupies the deep channel. A steep oxycline separates oxygen-rich upper layer from oxygen-poor lower layer at about 10 m depth. The low-oxygen water expands seaward from June to July and retreats landward after August. In July when the hypoxic zone (DO<2.0 mg L^{-1}) reached the annual peak, it encompassed the entire mid-bay region and a portion of the lower Bay, expanding from 37.2^{o}N near the mouth of York River, VA to 39.7^{o}N near Annapolis, MD. Particularly of note is the presence of large anoxic volume (DO<0.2 mg L^{-1}). It initially occupies a small area at the landward limit of the mid-bay to the north of 38.5^{o}N in June, and then extends vertically closer to oxycline and spreads seaward to approximately 38^{o}N near the mouth of Potomac River in July. It greatly diminishes by mid-August and is confined to the north end of the deep channel. We have compared the model predictions against the along-channel DO distributions obtained from ship surveys. Each observational snapshot is produced by the interpolation of

the CBP monitoring data and corresponds to a cruise that sampled sufficient (about 28) main-channel stations within approximately 5-day period, and the model DO is averaged over the same period. In the model results, the low-oxygen region initially appears at upper bay and extends downstream. The extent of low-oxygen water is largest in late July and covers similar region as observed. During the period of oxygen depletion, a similar vertical oxycline as well as a horizontal gradient is reproduced.

DO concentrations below approximately 2 mg L^{-1} are low enough to adversely affect marine life. Using this criterion, we calculate the volume that is affected by hypoxia in the main stem of the Bay (Fig. 6). The hypoxic condition appears in mid-June and surges in July, with the dimension of affected area reaching its annual maximum of 12.3 km^3, covering 21.8% of the total volume of the main channel. The situation is somehow reversed after August. The hypoxia is gradually destroyed and completely disappears by October. The hypoxic volume calculated by model shows a reasonable agreement with statistical estimations from the CBP data in terms of duration and magnitude, and the model skill is 0.92 and root-mean-square error is 2 km^3. It is noted that the hypoxic volume shows variability at weekly or monthly time scales, indicating that physical processes are important.

In order to understand seasonal cycle of oxygen content in the lower layer, it is convenient to define a fixed volume that represents the region most susceptible to hypoxic conditions in the bay. The selected volume encompasses all the waters below

10 m depth to north of York River mouth in the main stem (see Fig. 1c for location). Over the course of the year, the oxygen content undergoes a large seasonal cycle with summer minima and winter maxima (Fig. 6b). In the cooler months from January to March, the bottom water temperature is as low as 5 ^{o}C (Fig. 2d), and the overall DO content maintains its annual maximum of 10.1×10^{7} kg. From mid March to late July as water temperature rises, DO content declines until reaching the annual minimum of 1.1×10^{7} kg. After August, the oxygen content gradually recovers as the water temperature drops. The water temperature tends to have dual effects on oxygen removal. On the one hand, increasing temperature diminishes oxygen solubility. On the other hand; rising temperature stimulates planktonic and benthic respiratory processes. To determine which effect is more important, solubility-induced oxygen content is calculated for the control volume. The overall DO follows the solubility curve in cooler months, but shows large drawdown in warmer months. It should be noted that the drawdown by mere solubility is not strong enough to generate hypoxia. Thus, it is the combined effects of respiration and solubility that lead to summer depletion of oxygen in the lower layer.

In order to understand the imbalance between biogeochemical utilization and physical supply that cause the drawdown of oxygen in the lower layer, we calculate the monthly DO budget by integrating Eq. (1) over the control volume.

$$\frac{\partial M_{Ox}}{\partial t} = \overbrace{\underset{\text{lower-bay section}}{\iint}(uOx)dydz}^{\text{longitudinal advection}} + \overbrace{\underset{\text{10m interface}}{\iint}(-wOx)dxdy}^{\text{lateral advection}} + \overbrace{\underset{\text{10m interface}}{\iint}\left(K_V\frac{\partial Ox}{\partial z}\right)dxdy}^{\text{vertical diffusion}} + \underbrace{\underset{\text{control volume}}{\iiint}(WCR)dxdydz}_{\text{water column respiration}} + \underbrace{\underset{\text{control volume}}{\iiint}(\frac{SOD}{\Delta z_b})dxdydz}_{\text{sediment oxygen demand}} \quad (7)$$

where M_{Ox} is the DO content in the control volume (kg). It reveals that the total change of oxygen in the bottom layer can be described by 5 terms on the right-hand side of Eq. (7). The first three terms represent physical supply via longitudinal advection through the lower bay section, lateral advection and vertical diffusion across the 10-m depth. The last two terms represent biogeochemical consumptions via *WCR* and *SOD*. As expected, the air-sea exchange and phytoplankton production are not important in the lower layer of the water column. Horizontal diffusion is small enough to be neglected.

Figure 7a shows the two components of advective flux into the lower layer of the water column. Because net estuarine bottom flow is directed landward, the monthly along-channel flux is positive all year round, ranging from 21.0 kg s^{-1} to 61.1 kg s^{-1}, indicating a net source of oxygen into the control volume. The longitudinal oxygen flux is high in spring and winter but low in summer, exhibiting a factor of 2~3 change in the strength. The lateral advection across the 10 m isosurface ranges from -40.2 kg s^{-1} to 28.8 kg s^{-1}, and the net flux is bidirectional. Influx (positive) occurs from June to November while outflux (negative) occurs during spring-winter time. In a recent

study, *Scully* [2010] pointed out the importance of lateral processes in supplying oxygen to bottom water in the Bay, our results are consistent with his and show the lateral advection provides a net oxygen supply during hypoxic period. The calculated vertical diffusion is positive over the year and thus supplies oxygen into the lower layer (Fig. 7b). The seasonal cycle shows a minimum of 10.1 kg s^{-1} in March and a maximum of 31.1 kg s^{-1} in September. Interestingly, the total advective flux is nearly twice as large as the vertical diffusion. The traditional view of oxygen balance is between the diapycnal exchange and the biological consumption; however, our results suggest that this underestimates the role of advective processes in supplying oxygen into the lower layer.

The monthly oxygen consumptions are calculated for *WCR* and *SOD*, respectively (Fig. 7c). A strong seasonal cycle exists with high respiration rates found in warmer months, except that *SOD* is slightly reduced between July and August due to the inhibition by low DO. However, most seasonal variations are contributed by *WCR* rather than *SOD*. Over the course of the year, *WCR* dominates over *SOD* in oxygen utilization, comprising 74.2% ~ 85.8% of the total consumptions from June to September.

4. Processes affecting diffusive and advective oxygen fluxes

Even though the vertical diffusion contributes to replenishing the bottom dissolved oxygen during the summer, the mechanism to maintain the down-gradient

transport of oxygen has not been adequately addressed. Figure 8 shows the time series of model vertical salinity gradient, eddy diffusivity and vertical diffusion at 10 m depth from June to September. The vertical diffusion of oxygen is marked by flood-ebb fluctuation and modulation by spring-neap cycles, with higher value during spring tides (~40 kg s^{-1}) and lower during neaps (~10 kg s^{-1}) (Fig. 8e). The difference is mainly induced by the vertical diffusivity (Fig. 8d), which shows one-order of magnitude change over spring-neap cycle [cf. *Li and Zhong*, 2009]. In addition to the tidal forcing, winds generate strong mixing and thus drive episodic strong DO flux to bottom water. Several distinct spikes are shown in the vertical diffusion (Fig. 8e, i.e. July 28, August 7 and 19, September 5). Those episodic spikes lead to about 2-fold increase of the vertical oxygen flux from its background value. However, the relationship between the wind speed and vertical mixing appears to be highly nonlinear. The vertical diffusion is less spiky in the presence of strong stratification. It suggests that effective wind-mixing occurs if the wind-induced instability overcomes the buoyancy force.

With the coupled hydrodynamic-oxygen model, we can also explore the possible mechanisms responsible for the advective oxygen fluxes from June to September. First, we investigate the longitudinal advection (Fig. 9c). After averaging over the whole period, the longitudinal advection is positive (22.32 kg s^{-1}), indicating the import of oxygen due to the landward gravitational circulation in the lower layer. As tidal pumping is insignificant at the lower bay cross-section, tidal fluctuations are removed using a 34-hr low-pass filter. The subtidal longitudinal advection exhibits

large fluctuations at synoptic time scales. They are driven by the bottom volume transport generated by along-channel wind events. Winds from north (down-estuary) drive exchange flow that reinforces the gravitational circulation, whereas winds from south shut down or slightly reverse the gravitational flow [see Chapter 2, *Li and Li*, 2012]. For example, we show the times series of N-S wind and the subtidal bottom volume transport. On July 20, the winds from south shut down the gravitational transport at the lower bay (Fig. 9a and 9b), and the longitudinal advection of oxygen vanishes accordingly (Fig. 9c). In contrast, on July 29, a northerly wind blows over the Bay, and the volume transport at lower bay increases to 8.2×10^{-3} m^3 s^{-1}, twice as large as the 3-month average of 3.4×10^{-3} m^3 s^{-1}. Consequently, the longitudinal advection doubles (47.44 kg s^{-1}) and imports more dissolved oxygen into the study area. Over the whole period, we show three examples of winds from north, which lead to stronger inflow and longitudinal advection through lower Bay. We also show seven examples of winds from south, which weaken or reverse bottom inflow and longitudinal advection. The correlation coefficient between the N-S wind speed and the bottom volume transport is 0.51.

Next we examine the subtidal lateral advection of oxygen. Over the 3-month period, lateral advection is positive at most times and thus supplies oxygen into the lower layer. The time series reveals significant weather band fluctuations (Fig. 9d), but it shows a pattern opposite to that of the longitudinal advection, where winds from south are more effective at driving lateral advection than winds from north. For example, when the winds blow from the south on July 20, the lateral advection is as

large as 42.93 kg s^{-1}. In contrast, the lateral circulation reduces to 1.34 kg s^{-1} on July 29 during the winds from north. The asymmetric responses between south and north wind events may be due to the fact that winds from south usually drive stronger lateral circulation than winds from north [see Chapter 2, *Li and Li*, 2012]. Besides, the bathymetric effect in the Bay is also important, since more broad shoals locate on the western side of the channel [*Scully*, 2010b].

To better understand the longitudinal and lateral advections, we plot the current and oxygen fields under different wind conditions in Figure 10. On July 20, when the winds blow from south, they tend to drive a landward flow in the upper layer and a compensatory seaward flow in the lower layer, putting a brake on the two-layer gravitational circulation. The bottom inflows become less than 0.1 m s^{-1} in most areas of the deep channel (Fig 10a and 10b). In the meantime, a clockwise lateral circulation develops in the cross-channel section, with speeds comparable to the along-channel currents (Fig. 10c). The lateral circulation spreads oxygen-poor water onto the western flank and receives the oxygen-rich water from the eastern flank (Fig. 10d). The replacement of low DO by high DO results in a net gain of oxygen in the lower layer. On July 29, the northerly winds amplify the gravitational circulation in the along-channel section, with bottom inflows larger than 0.3 m s^{-1} (Fig. 10e and 10f). A counterclockwise lateral circulation causes upwelling on the eastern side of the channel and downwelling on the western side (Fig. 10g). Once again, it replaces the low-oxygen water with high-oxygen water and imports oxygen into the bottom

layer. Therefore, the net effect of wind-induced lateral circulation is to supply oxygen into the hypoxic zone.

5. Sensitivity analysis

The results presented in the last two Sections based on a hindcast run with configuration and physical forcings prescribed from observations. In this section, we examine the coupled hydrodynamic-oxygen model in terms of its sensitivity to external forcings and biogeochemical processes. In general, we adjust climatic conditions such as river flow and wind speed to understand the response of hypoxia volume to specific forcings. Moreover, we change the oxygen respiration rates to assess the relative importance of biogeochemical processes (*WCR* and *SOD*) in causing the summer hypoxia in the Bay.

a. Sensitivity to changes in river runoff

The first group of the experiments is to understand how the magnitude of river discharge affects the annual hypoxic volume in the Bay. The simple oxygen model does not consider the riverine nutrient inputs and thus can provide a clean test case to evaluate the river's physical controls on hypoxia. Over the past century, annual mean discharge varies between 1000 to 3500 m^3s^{-1}, while mean discharge in this year is about 1800 m^3s^{-1}. Thus, we halve (Run RH) and double (Run RD) the observed river flow to represent extremely dry and wet conditions.

Surprisingly, the maximum hypoxia volume shows a weak 4% increase in Run RH and no more than 10% decrease in Run RD (Fig. 11a), with the timing of annual hypoxia almost same as the base run. To understand why the response to river flow is so weak, we examine the estuarine transport, stratification and the oxygen fluxes during the development of hypoxia. As shown in Fig. 11c and 11d, as river flow increases, there is a clear increase in longitudinal volume transport and salinity stratification. The change is similar to the trend predicted by the steady-state theory with a slightly weaker dependence than their respective power-law dependence. The eddy diffusivity decreases from low to high river discharges in response to the river-induced stratification (Fig. 11e). Those estuarine adjustments consequently drive the changes in the advective and diffusive oxygen fluxes into the lower layer (Fig. 11b). In Run RH, high runoff strengthens estuarine the longitudinal transport and longitudinal advection, but stronger stratification suppresses the lateral advection and vertical diffusion. The opposite is true for Run RD with low runoff. Because the changes of three terms buffer each other to maintain a relatively stable total oxygen supply, the hypoxic volume shows little variations in response to changes in the river flow.

b. Sensitivity to changes in wind speed

In the second group of experiments, we examine how the changes of wind speed affect annual hypoxia in the Bay. The results in Section 4 show that wind influences

all physical supply terms of DO by altering vertical mixing and three-dimensional circulation. In addition, wind speed is also shown to influence the air-sea exchange rate [Eq. (2)]. The sensitivity to those processes is unclear since the responses are nonlinear. Using lengthy wind observations from 1985 to 2010 from meteorological stations, we compare the annual mean wind speed to this year. The wind speed varies from 75% to 135%, and this translates to 56% to 182% of wind stress. Thus, we halve and double the wind stress in Run WH and Run WD as a first step to evaluate the wind influences.

Both Run WD and WH show hypoxia volume less than the base run (Fig. 12a). In Run WD, the hypoxia volume is reduced by 6% ~ 29% between June and September. Owing to the increase in wind magnitude, the lateral advection is stronger, and so is the vertical diffusion that benefits from stronger wind mixing (Fig. 12b and 12e). However, the longitudinal advection is weaker because oxygen in the lower Bay is lower. Overall they provide a stronger supply in comparison to the base run. Because the physical supplies exceed biogeochemical consumptions to cause gradual reduction of hypoxia volume in fall, it is noted that the doubling of wind stress can accelerate the termination of annual hypoxia.

In Run WH, the hypoxia is delayed for about 0.5 month and the maximum volume is 9.7 km^3 which is 20% less than the base case. Even though weaker wind stress lessens the vertical diffusion and lateral advection, the hypoxia is less severe in July due to the stronger longitudinal advection that replenishes bottom water with

oxygen-rich water from the lower Bay region (Fig. 12b). The high DO (> 10 mg L^{-1}) found in the lower bay are oversaturated for that season (Fig. 12d). As wind stress becomes half of the base run, it slows down the air-sea exchange, so there seems to be an accumulation of excess oxygen either from high DO carried over from spring time or by phytoplankton production.

c. Sensitivity to changes in biogeochemistry

In the third group of experiments, we conduct two numerical runs to examine how the hypoxic volume changes with different prescriptions of the respiration rates. We keep hydrodynamic model unchanged but attribute the oxygen consumption to either only *SOD* or only *WCR* in the oxygen model (Run OS and Run OW). In doing so, the estuarine circulation and stratification are identical to the base run.

As shown in Figure 13a, Run OS does not produce summer hypoxia, and it confirms that total consumption in the lower layer is more associated with *WCR* rather than *SOD*, and this is consistent with our oxygen budget analysis (Fig. 7c and Section 3). In Run OW, the hypoxic volume is underestimated by 50%, and the onset of annual hypoxia is delayed to July with one-month lag. It suggests that two respiration processes play different roles on the development of seasonal hypoxia. *SOD* is important in controlling the onset while *WCR* is crucial to spatial extension, but maximum hypoxia volume in summer should be determined by both. Physical supply terms respond to oxygen field in two different ways. In comparison to the base

run, the longitudinal advection increases because the oxygen concentrations are found much higher at lower bay section (Fig. 13c and 13b). In contrast, the vertical diffusion and lateral advection decrease because the vertical oxygen gradient is weaker (Fig. 13c and 13d).

6. Conclusions

We have coupled an oxygen model to the three-dimensional hydrodynamic model (ROMS) to simulate seasonal oxygen cycle in Chesapeake Bay. The model reasonably reproduces the observed spatial-temporal characteristics of oxygen in the main stem of the Bay as well as the seasonal change of hypoxia volume. We conduct budget analysis of DO for the lower layer of the water column. It is found that the season cycle of oxygen depletion in the bottom water is driven by the imbalance between physical supply and biogeochemical utilization. For the physical supply, the results show that in summer time the longitudinal and lateral advections of oxygen are as important as vertical diffusion, and the total strength of advection is twice as large as the vertical diffusion. It suggests the traditional view of summer oxygen balance between diapycnal exchange and the biogeochemical utilization may underestimate the role of advective processes in supplying oxygen into the lower layer.

Our results also show that the advective oxygen fluxes are mainly driven by longitudinal and lateral circulation generated by N-S wind events. The advective

supply of oxygen depends on wind direction. Winds from south are more effective to supply oxygen via lateral advection but less effective via longitudinal advection. Given the importance of the wind-driven lateral circulations on the dissolve oxygen, especially for long estuary with wide channels and weak tides, future observational study of the wind effects on lateral circulation and oxygen exchange is warranted.

The sensitivity analyses based on variable wind stress and river flow provide insights into the key climatic factors that may affect the interannual variability of hypoxia volume. The maximum hypoxia volume decreases 6 ~ 20% when the wind stress doubles or halves, but it changes less than 10% over a wide range of river conditions, because river-induced adjustments in oxygen supply compensate for one another and leave total supply largely conserved. Since the oxygen model isolates physical controls from nutrient dynamics, it suggests that net effect of river flow on the large variation in observed hypoxia volume may be explained by nutrient dynamics. The result has important implication for nutrient management, and thus is worthy of further investigation using a biogeochemical model that considers nutrient loading and production of organic carbon.

Acknowledgements: We thank Younjoo Lee for providing the statistical interpolation of Chesapeake Bay Program monitoring data, and Jeremy Testa for useful discussion on the data regression. We are grateful to NSF (OCE-082543 and OCE-0961880) and NOAA (CHRP-NA07N054780191) for the financial support. This is UMCES contribution number xxxx and CHRP contribution number xxx.

References

Boicourt, W. C. (1992), Influences of circulation processes on dissolved oxygen in the Chesapeake Bay.

Boynton, W. R., and E. M. Bailey (2008), Sediment oxygen and nutrient exchange measurements from Chesapeake Bay: development of a comprehensive database and analysis of factors controlling patterns and magnitude of sediment-water exchanges. *TS-542-08*, University of Maryland Center for Environmental Science.

Boynton, W., W. Kemp, and C. Keefe (1982), A comparative analysis of nutrients and other factors influencing estuarine phytoplankton production, *Estuarine Comparisons. Academic Press, New York*, 69-90.

Cerco, C. (1995), Response of Chesapeake Bay to nutrient load reductions, *J. Environ. Eng.*, *121*, 549, doi: 10.1061/(ASCE)0733-9372(1995)121:8(549).

Cerco, C. F., and T. M. Cole (1994), Three-dimensional eutrophication model of Chesapeake Bay. Volume 1: Main report, DTIC Document.

Cowan, J. L. W., and W. R. Boynton (1996), Sediment-water oxygen and nutrient exchanges along the longitudinal axis of Chesapeake Bay: Seasonal patterns, controlling factors and ecological significance, *Estuaries*, *19*(3), 562-580, doi: 10.2307/1352518.

Diaz, R. J. (2001), Overview of hypoxia around the world, *J. Environ. Qual.*, *30*(2), 275-281, doi: 10.2134/jeq2001.302275x.

Diaz, R. J., and R. Rosenberg (1995), Marine benthic hypoxia: a review of its ecological effects and the behavioural responses of benthic macrofauna, *Oceanogr. Mar. Biol., Annu. Rev.*, *33*, 245-303.

Egbert, G. D., and S. Y. Erofeeva (2002), Efficient inverse modeling of barotropic ocean tides, *J. Atmos. Oceanic Technol.*, *19*(2), 183-204, doi: 10.1175/1520-0426(2002)019<0183:EIMOBO>2.0.CO;2

Egbert, G. D., A. F. Bennett, and M. G. G. Foreman (1994), TOPEX/POSEIDON tides estimated using a global inverse model, *J. Geophys. Res.*, *99*(C12), 24821-24824,24852, doi: 10.1029/94JC01894.

Fairall, C., E. Bradley, J. Hare, A. Grachev, and J. Edson (2003), Bulk parameterization of air-sea fluxes: Updates and verification for the COARE algorithm, *J. Climate*, *16*(4), 571-591, doi: 10.1175/1520-0442(2003)016<0571:BPOASF>2.0.CO;2.

Fisher, T., A. Gustafson, G. Radcliffe, K. Sundberg, and J. Stevenson (2003), A long-term record of photosynthetically available radiation (PAR) and total solar energy at 38.6N, 78.2W, *Estuaries Coasts*, *26*(6), 1450-1460, doi: 10.1007/BF02803653.

Garcia, H. E., and L. I. Gordon (1993), Oxygen solubility in seawater - Better fitting equations (Vol 37, Pg 1308, 1992), *Limnol. Oceanogr.*, *38*(3), 656-656, doi: 10.4319/lo.1992.37.6.1307.

Hagy, J. D., W. R. Boynton, C. W. Keefe, and K. V. Wood (2004), Hypoxia in Chesapeake Bay, 1950-2001: Long-term change in relation to nutrient loading and river flow, *Estuaries*, *27*(4), 634-658, doi: 10.1007/BF02907650.

Haidvogel, D. B., H. G. Arango, K. Hedstrom, A. Beckmann, P. Malanotte-Rizzoli, and A. F. Shchepetkin (2000), Model evaluation experiments in the North Atlantic Basin: simulations in nonlinear terrain-following coordinates, *Dynam. Atmos. Oceans*, *32*(3), 239-281, doi: 10.1016/S0377-0265(00)00049-X.

Hetland, R. D., and S. F. DiMarco (2008), How does the character of oxygen demand control the structure of hypoxia on the Texas-Louisiana continental shelf?, *J. Marine Syst.*, *70*(1-2), 49-62, doi: 10.1016/j.jmarsys.2007.03.002.

Kemp, W. M., P. A. Sampou, J. Garber, J. Tuttle, and W. R. Boynton (1992), Seasonal depletion of oxygen from bottom waters of Chesapeake Bay - Roles of benthic and planktonic respiration and physical exchange processes, *Mar. Ecol. Prog. Ser.*, *85*(1-2), 137-152.

Kemp, W. M., J. M. Testa, D. J. Conley, D. Gilbert, and J. D. Hagy (2009), Temporal responses of coastal hypoxia to nutrient loading and physical controls, *Biogeosciences*, *6*(12), 2985-3008, doi: 10.5194/bg-6-2985-2009.

Kuo, A. Y., and B. J. Neilson (1987), Hypoxia and salinity in Virginia Estuaries, *Estuaries*, *10*(4), 277-283, doi: 10.2307/1351884.

Levitus, S. (1983), Climatological Atlas of the World Ocean, *Eos, Trans. Amer. Geophys. Union*, *64*(49), 962-963, doi: 10.1029/EO064i049p00962-02.

Li, M., and L. J. Zhong (2009), Flood-ebb and spring-neap variations of mixing, stratification and circulation in Chesapeake Bay, *Cont. Shelf Res.*, *29*(1), 4-14, doi: 10.1016/j.csr.2007.06.012.

Li, M., L. J. Zhong, and W. C. Boicourt (2005), Simulations of Chesapeake Bay estuary: Sensitivity to turbulence mixing parameterizations and comparison with observations, *J. Geophys. Res.*, *110*(C12), -, doi 10.1029/2004jc002585.

Li, M., L. Zhong, and L. W. Harding (2009), Sensitivity of plankton biomass and productivity to variations in physical forcing and biological parameters in Chesapeake Bay, *J. Mar. Res.*, *67*(5), 667-700, doi: 10.1357/002224009791218878.

Li, M., L. Zhong, W. C. Boicourt, S. L. Zhang, and D. L. Zhang (2007), Hurricane-induced destratification and restratification in a partially-mixed estuary, *J. Mar. Res.*, *65*(2), 169-192.

Li, Y., and M. Li (2012), Wind-driven lateral circulation in a stratified estuary and its effects on the along-channel flow, *J. Geophys. Res.* doi:10.1029/2011JC007829

Malone, T. C., W. M. Kemp, H. W. Ducklow, W. R. Boynton, J. H. Tuttle, and R. B. Jonas (1986), Lateral variation in the production and fate of phytoplankton in a partially stratified estuary, *Mar. Ecol. Prog. Ser.*, *32*(2-3), 149-160, doi: 10.3354/meps032149.

Marchesiello, P., J. McWilliams, and A. Shchepetkin (2001), Open boundary conditions for long-term integration of regional oceanic models, *Ocean Modell.*, *3*(1), 20, doi: 10.1016/S1463-5003(00)00013-5.

Mesinger, F., G. DiMego, E. Kalnay, K. Mitchell, P. C. Shafran, W. Ebisuzaki, D. Jovic, J. Woollen, E. Rogers, and E. H. Berbery (2006), North American regional reanalysis, *Bull. Am. Meteorol. Soc.*, *87*(3), 343-360, doi: 10.1175/BAMS-87-3-343.

Murphy, R. R., W. M. Kemp, and W. P. Ball (2011), Long-term trends in Chesapeake Bay seasonal hypoxia, stratification, and nutrient loading, *Estuaries Coasts*, 1-17, doi: 10.1007/s12237-011-9413-7.

Officer, C., R. Biggs, J. Taft, L. Cronin, M. Tyler, and W. Boynton (1984), Chesapeake Bay anoxia: origin, development, and significance, *Science*, *223*(4631), 22, doi: 10.1126/science.223.4631.22.

Sampou, P., and W. M. Kemp (1994), Factors regulating plankton community respiration in Chesapeake Bay, *Mar. Ecol. Prog. Ser.*, *110*(2-3), 249-258.

Sanford, L. P., and W. C. Boicourt (1990), Wind-forced salt intrusion into a tributary estuary, *J. Geophys. Res.*, *95*(C8), 13357-13371, doi: 10.1029/JC095iC08p13357.

Scully, M. E. (2010a), The importance of climate variability to wind-driven modulation of hypoxia in Chesapeake Bay, *J. Phys. Oceanogr.*, *40*(6), 1435-1440, doi: 10.1175/2010JPO4321.1.

Scully, M. E. (2010b), Wind modulation of dissolved oxygen in Chesapeake Bay, *Estuaries Coasts*, *33*(5), 1164-1175, doi: 10.1007/s12237-010-9319-9.

Shchepetkin, A. F., and J. C. McWilliams (2005), The regional oceanic modeling system (ROMS): a split-explicit, free-surface, topography-following-coordinate oceanic model, *Ocean Modell.*, *9*(4), 347-404, doi: 10.1016/j.ocemod.2004.08.002.

Smith, E., and W. Kemp (1995), Seasonal and regional variations in plankton community production and respiration for Chesapeake Bay, *Mar. Ecol. Prog. Ser.*, *116*(1), 217-231.

Taft, J. L., W. R. Taylor, E. O. Hartwig, and R. Loftus (1980), Seasonal oxygen depletion in Chesapeake Bay, *Estuaries Coasts*, *3*(4), 242-247, doi: 10.2307/1352079.

Turner, R. (1978), Community plankton respiration in a salt marsh estuary and the importance of macrophytic leachates, *Limnol. Oceanogr.*, *23*(3), 442-451.

Wanninkhof, R. (1992), Relationship between Wind-Speed and Gas-Exchange over the Ocean, *J. Geophys. Res.*, *97*(C5), 7373-7382, doi: 10.1029/92JC00188.

Warner, J. C., W. R. Geyer, and J. A. Lerczak (2005), Numerical modeling of an estuary: A comprehensive skill assessment, *J. Geophys. Res.*, *110*, C05001, doi: 10.1029/2004JC002691.

Xu, J. T., S. Y. Chao, R. R. Hood, H. V. Wang, and W. C. Boicourt (2002), Assimilating high-resolution salinity data into a model of a partially mixed estuary, *J. Geophys. Res.*, *107*(C7), -, doi: 10.1029/2000jc000626.

Zhong, L., and M. Li (2006), Tidal energy fluxes and dissipation in the Chesapeake Bay, *Cont. Shelf Res.*, *26*(6), 752-770, doi: 10.1016/j.csr.2006.02.006.

Figures

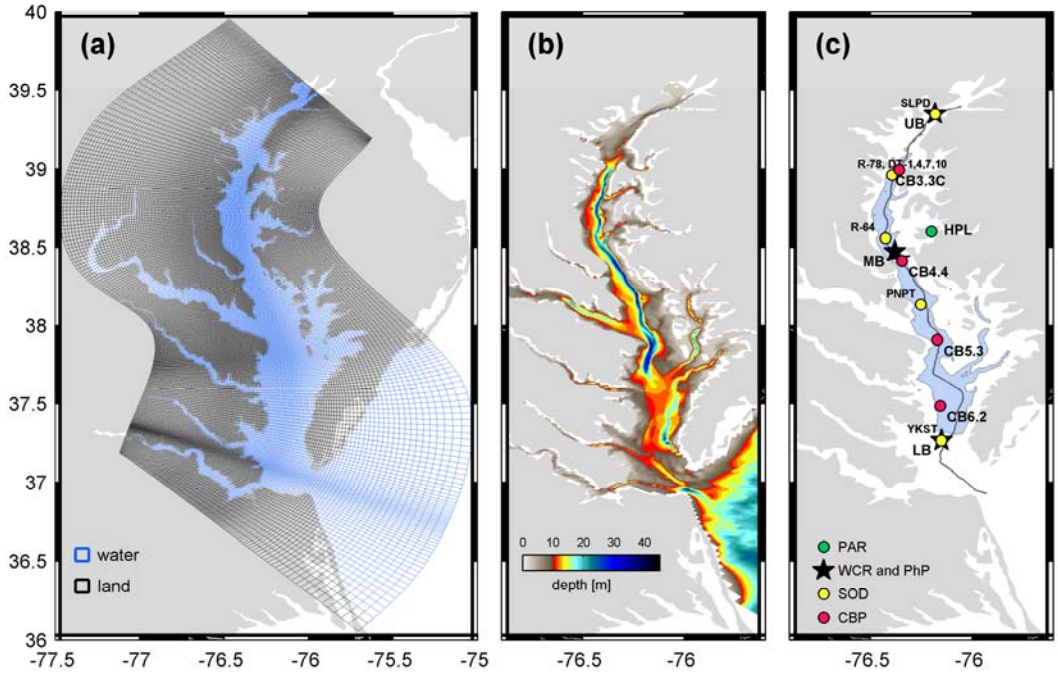

Figure 4-1. Model grid and bathymetry in Chesapeake Bay and the adjacent shelf, and locations of the longitudinal and mid-bay transect along with previous observation stations. The green circles represent the observation station at Horn Point Lab, Cambridge MD for Photosynthetically Available Radiation (PAR). The black stars represent Water Column Respiration (WCR) and Phytoplankton Production stations from *Smith and Kemp* [1995]. The yellow circles represent the Sediment Oxygen Demand (SOD) documented in GONZO dataset, and the red circles represent four mid-bay stations along EPA cruise route.

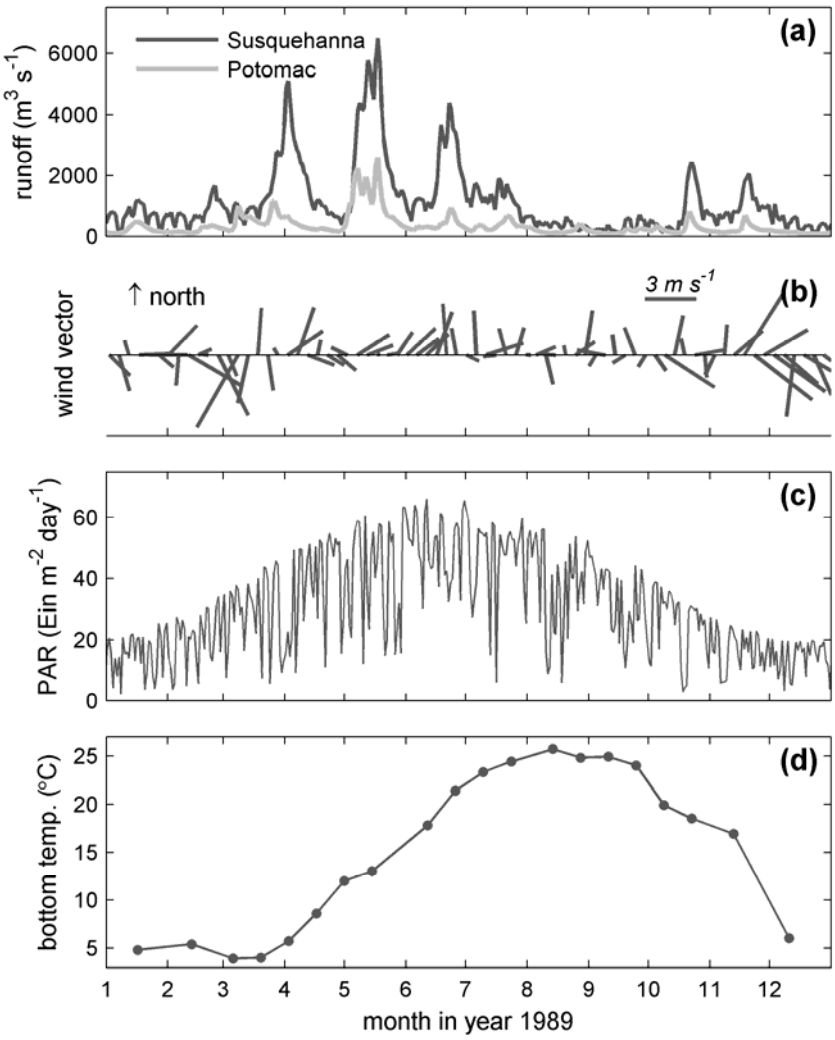

Figure 4-2. Time series of (a) 5-day mean wind vector near Patuxent River Navy Station, (b) river runoff from Susquehanna (black) and Potomac River (gray), (c) surface value of Photosynthetically Available Radiation (PAR) measured at Horn Point Lab, MD, and (d) the bottom water temperature at CB4.4 station.

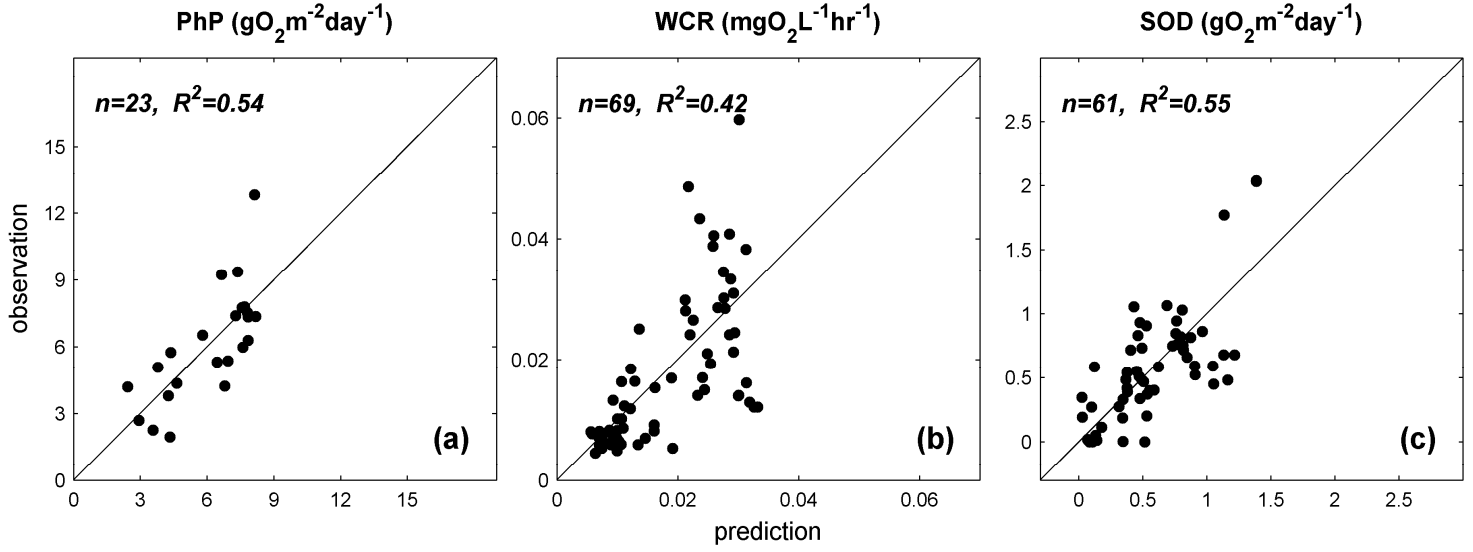

Figure 4-3. Predictions of oxygen source and sink terms versus the observations. For convenience, model units are transferred to the observation units in the plot. The diagonal 1:1 line represents a perfect fit of observation via their individual formula described in Section 2

.

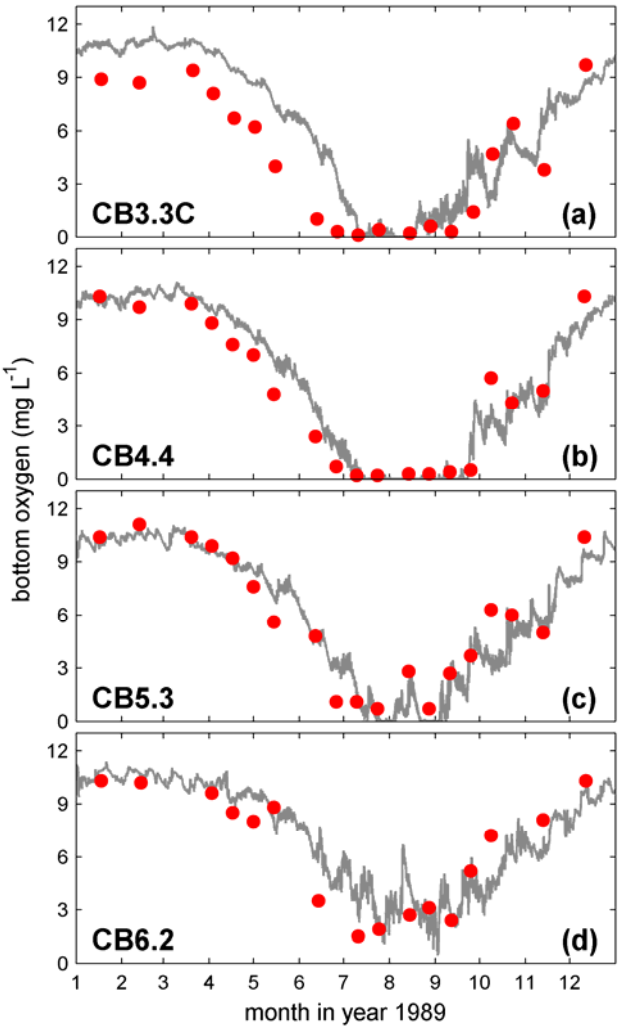

Figure 4-4. Annual time series of bottom oxygen concentrations at four along-channel CBP monitoring stations CB3.3C, CB4.4, CB5.3 and CB6.2. The model predictions are depicted in gray curve while the observations are shown in red dots.

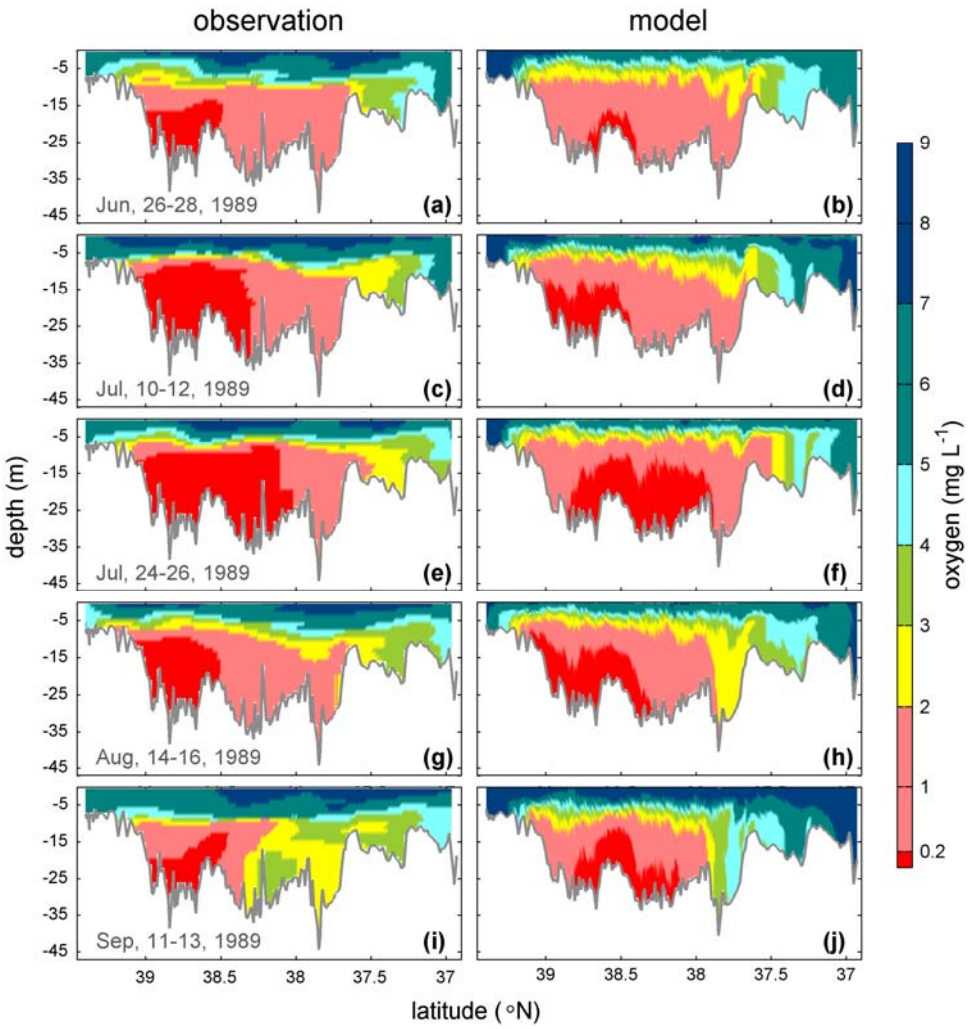

Figure 4-5. the spatial pattern of dissolved oxygen along the deep channel of Chesapeake Bay during hypoxia season. The observations are shown in the left column, and model results are in the right column.

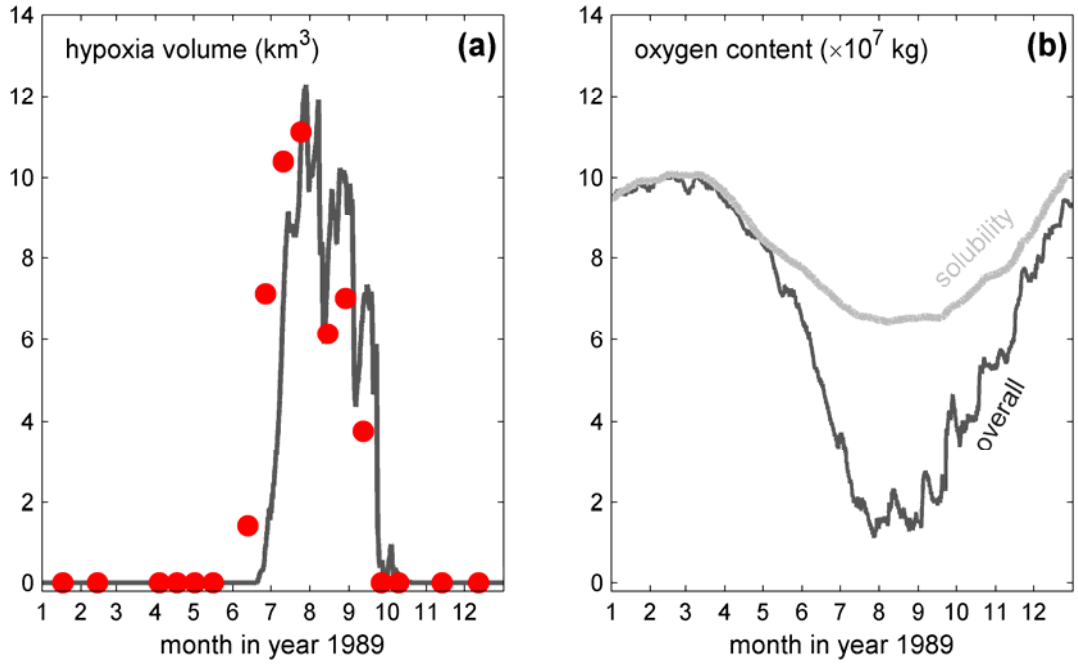

Figure 4-6. Annual time series of (a) observed (red dot) and model (black line) hypoxia volume (DO<2 mg L^{-1}) in the main stem of Chesapeake bay and (b) oxygen content in the lower layer of the water column below 10 m depth. The black line denotes the overall content of dissolved oxygen, while the gray line denotes the solubility-predicted oxygen content via *Garcia and Gordon* formula [1992]. The estimated hypoxia volume is calculated using statistical interpolation of CBP cruise data (personal contact with Younjoo Lee).

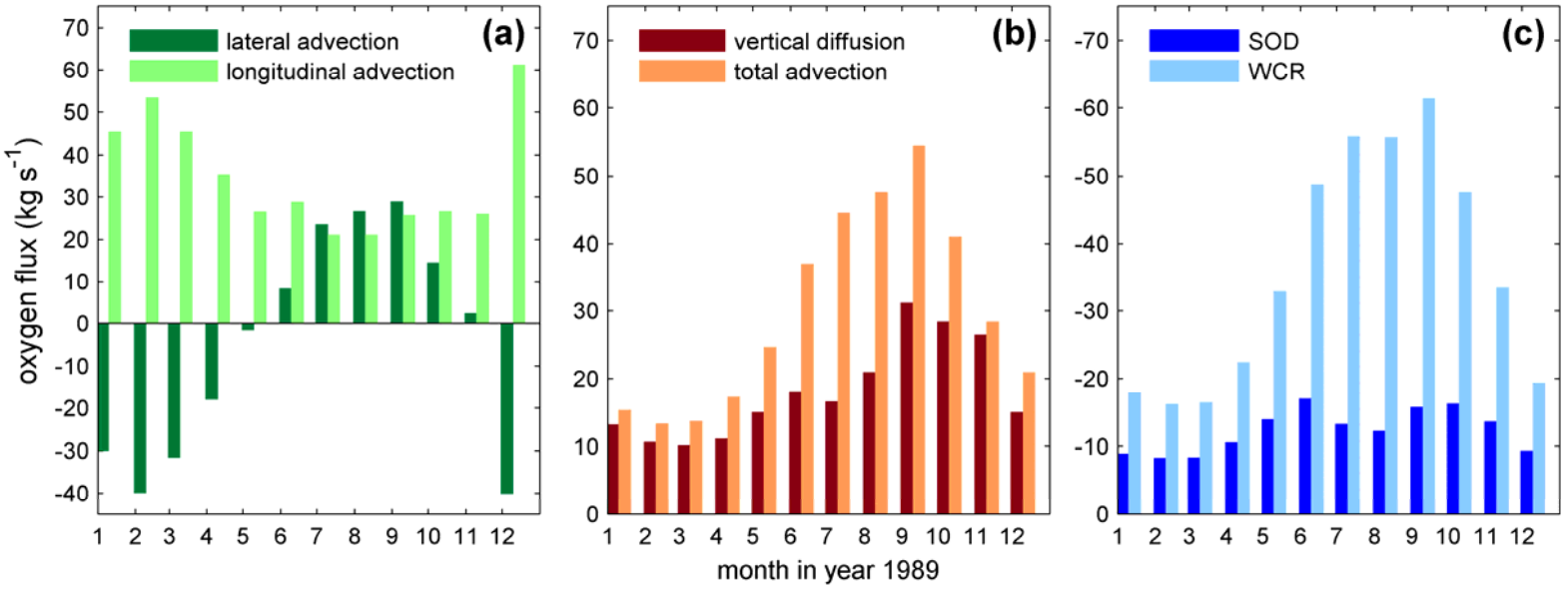

Figure 4-7. Monthly averaged oxygen source and sink terms into the lower water column below 10 m depth: (a) vertical and horizontal advective oxygen flux, (b) vertical diffusive and total advective flux, and (c) the oxygen consumption due to sediment oxygen demand (SOD) and water column respiration (WCR). The vertical axis of (c) is reversed.

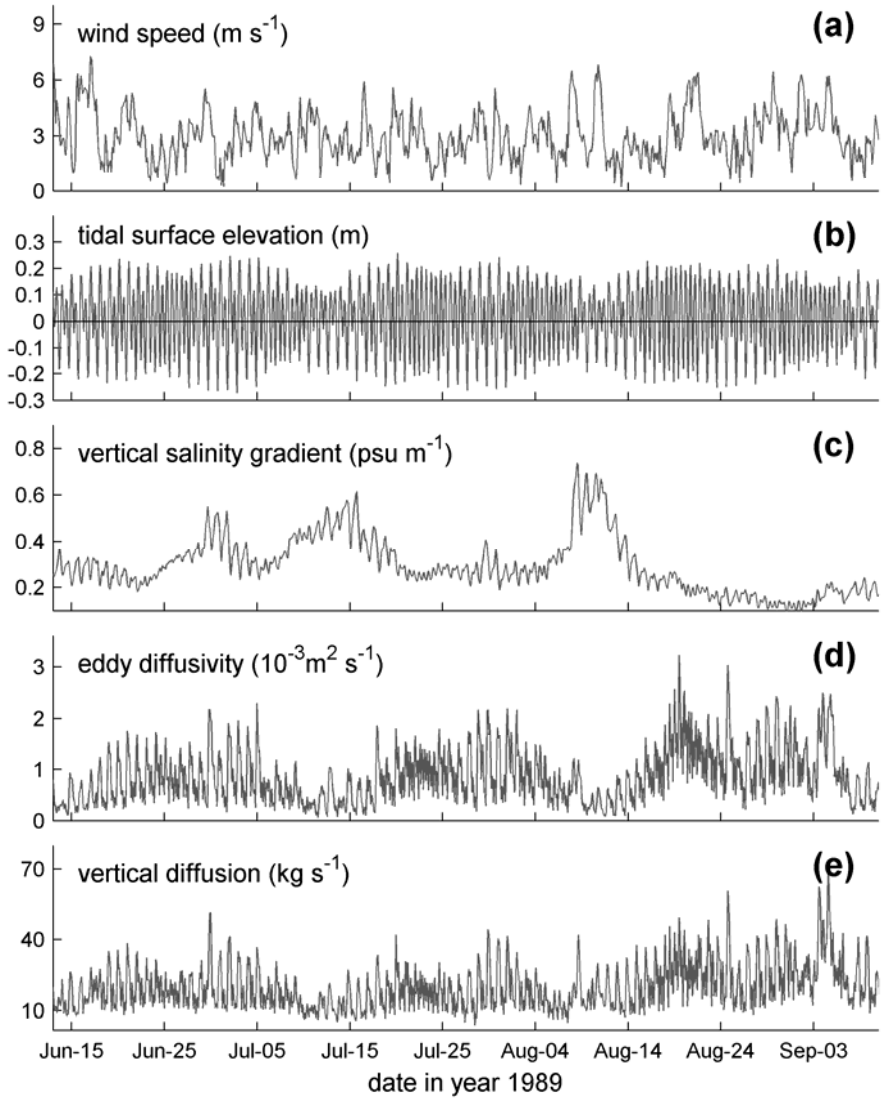

Figure 4-8. The time series of (a) NARR wind speed near Patuxent River Navy Station (b) model surface tidal elevation at mid-bay near station CB5.3, and the physical variables at 10 m depth, including (c) vertical salinity gradient, (d) eddy diffusivity and (e) vertical diffusion of oxygen. Positive fluxes indicate a net gain of oxygen for the select control volume.

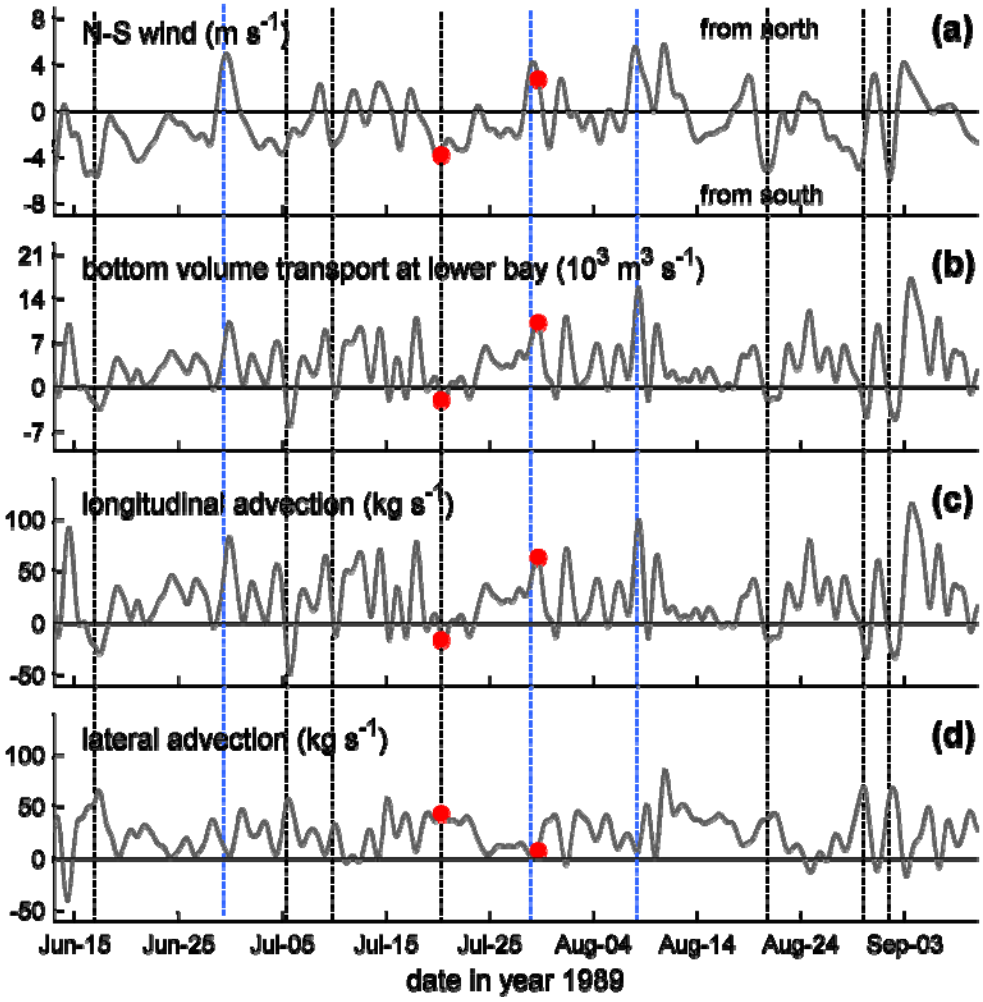

Figure 4-9. Time series of 34-hr low-passed (a) wind speed in the north-south direction near Patuxent River Navy Station, (b) along-channel volume transport at lower-bay below 10 m depth, and (c) horizontal and (d) vertical advective oxygen flux into the control volume. For the oxygen flux, positive values indicate a tendency to increase oxygen content in the control volume. The two red dots denote an example of two along-channel wind events, and the dashed lines show more examples of north (blue) and south (black) wind events.

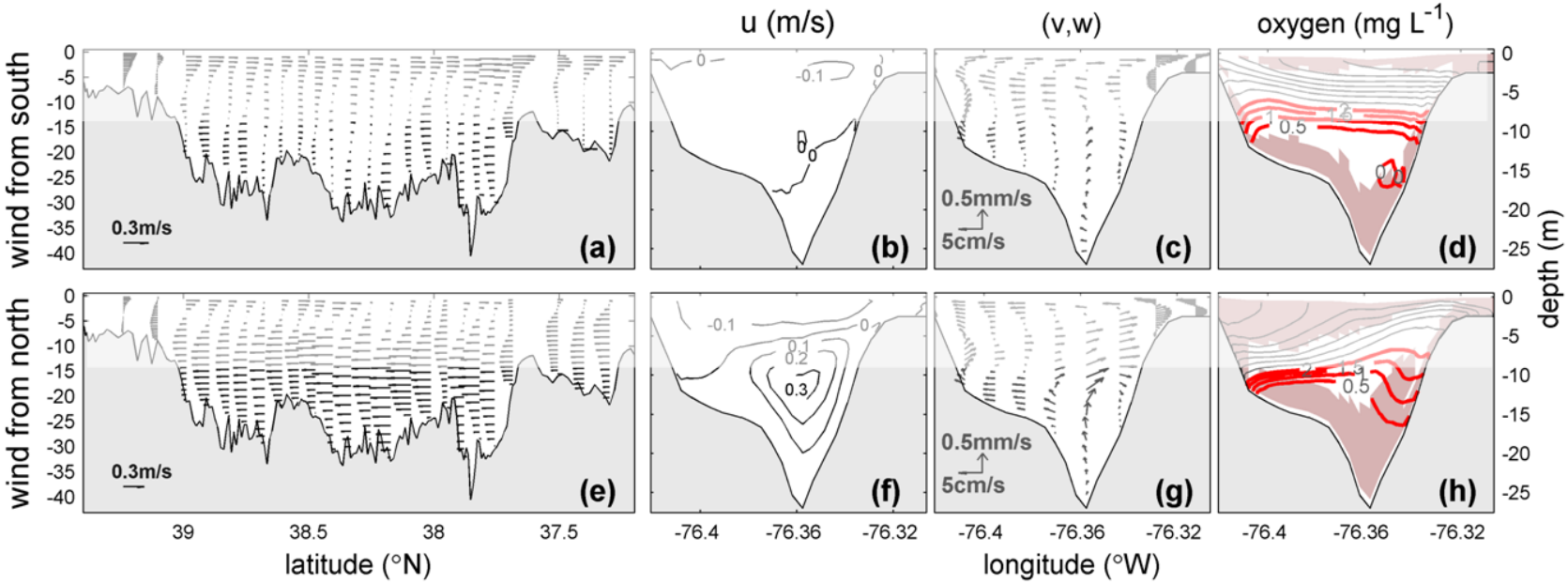

Figure 4-10. The distributions of 34-hr low-passed (a/b/e/f) along-channel currents, (c/g) lateral circulation and (d/h) oxygen contours at a mid-bay section under different wind conditions. The top row is taken on July 20, 1989 when the wind came from south, and the bottom row is selected on July 29, 1989 during wind from north. The regions with high eddy diffusivity ($> 10^{-3}$ m^2 s^{-1}) are shaded in red purple. The two wind events are marked in Fig. 11 in red dots

.

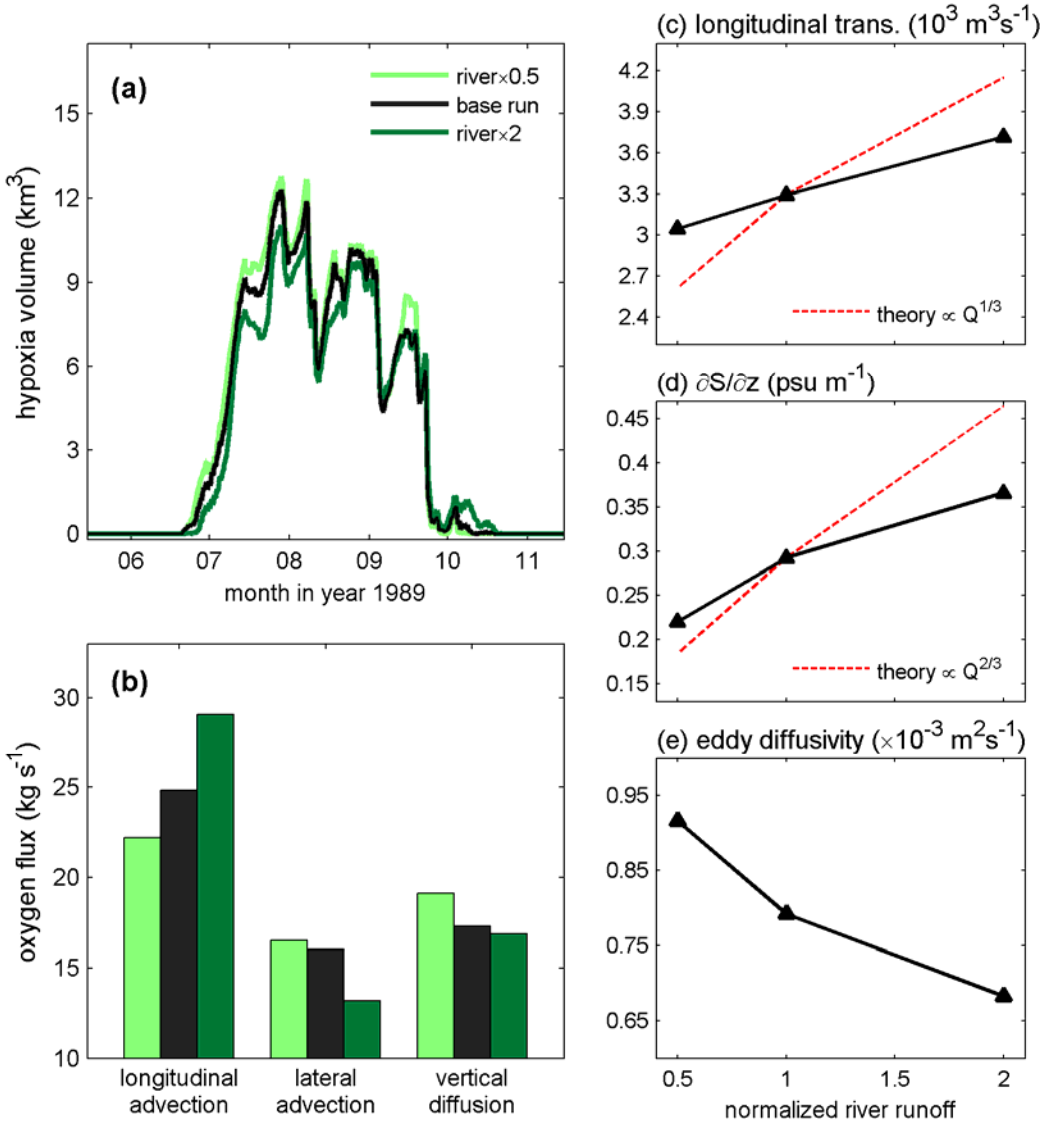

Figure 4-11. For the sensitivity Runs RH and RD. (a) the time series of annual hypoxia volume (DO< 2 mg L^{-1}), (b) the June-July oxygen supply terms, and (c-e) the June-July averaged longitudinal transport at lower bay, vertical salinity gradient at 10m and eddy diffusivity at 10 m against normalized river runoff.

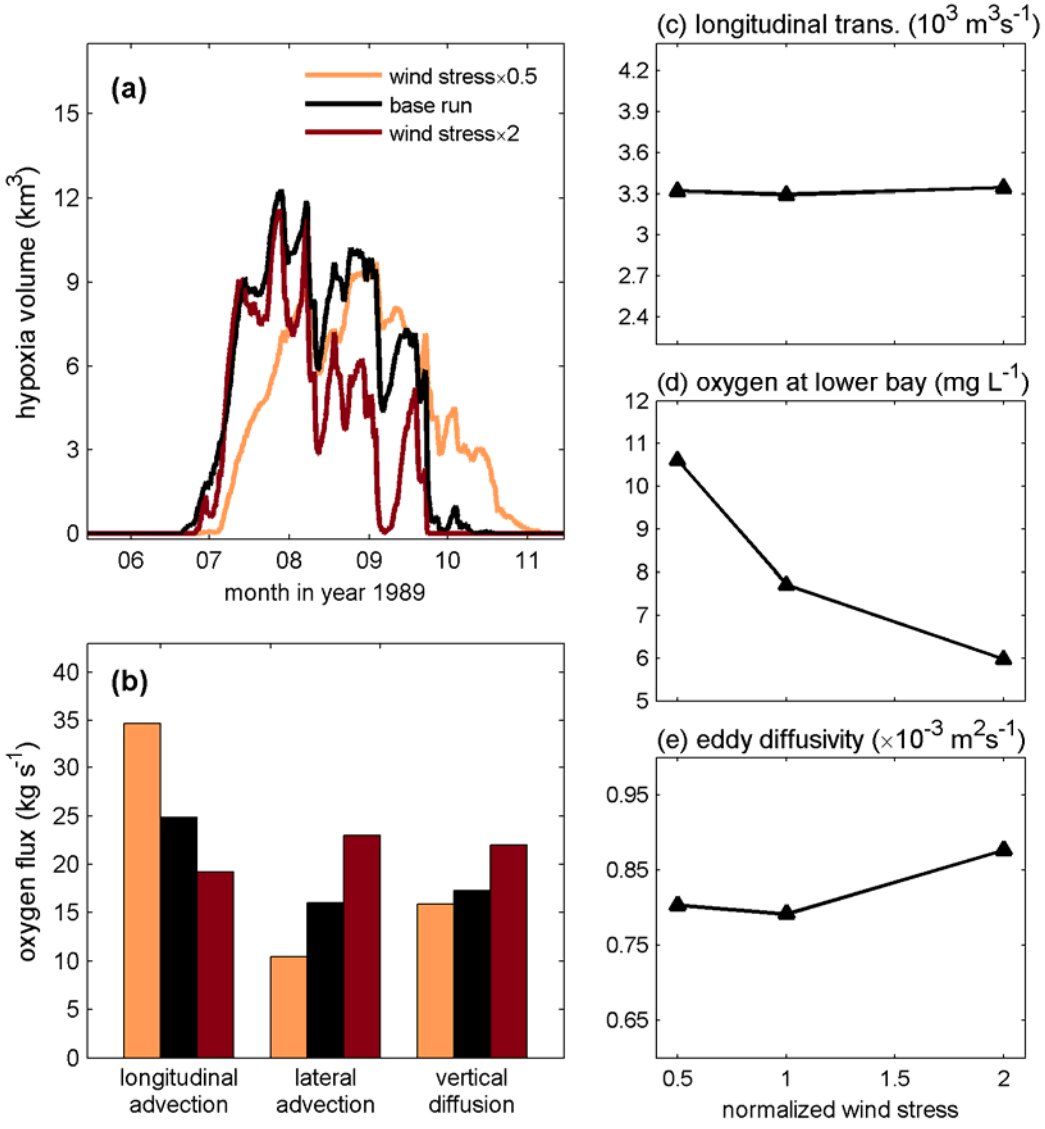

Figure 4-12. For the sensitivity Runs WH and WD, (a) the time series of annual hypoxia volume (DO< 2 mg L^{-1}), (b) the June-July oxygen supply terms, and (c-e) the June-July averaged longitudinal transport at lower bay, oxygen concentration at lower bay and eddy diffusivity at 10 m depth against normalized wind stress.

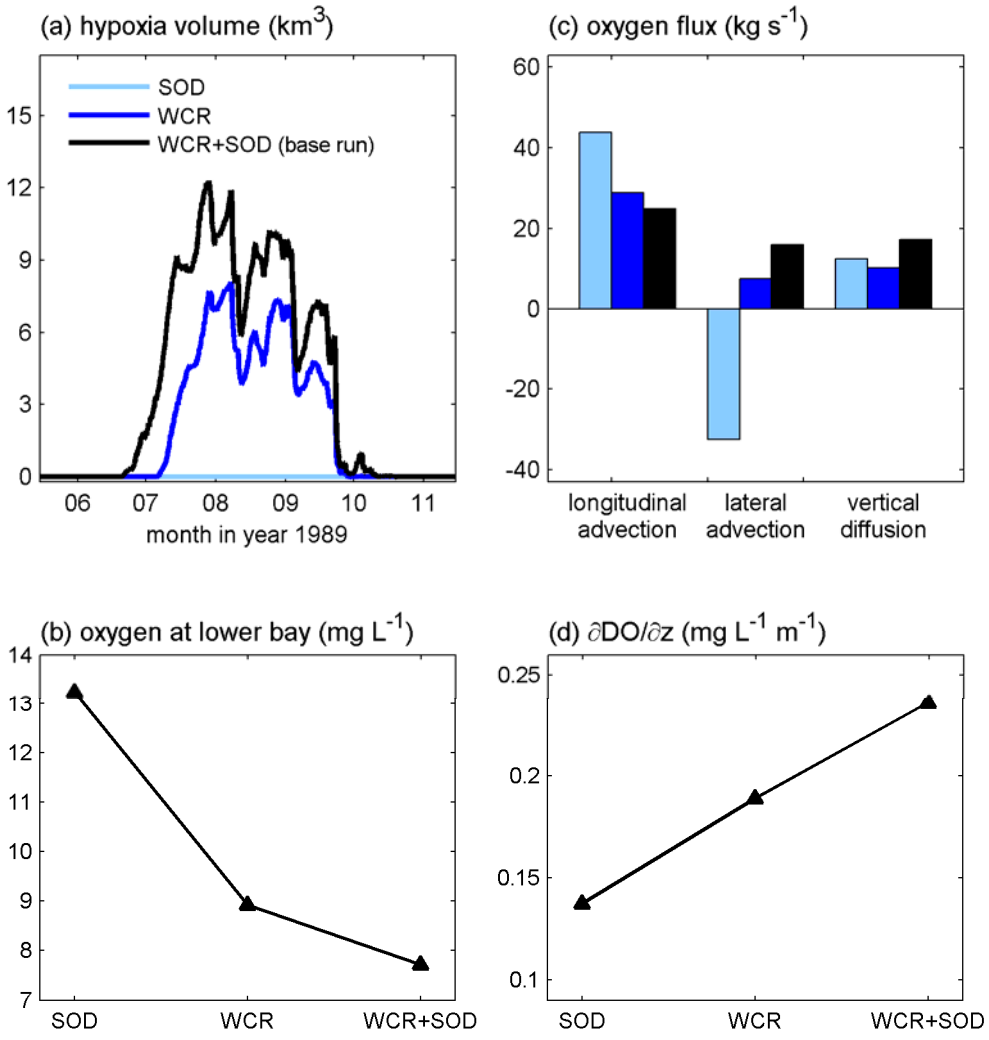

Figure 4-13. For the sensitivity runs OS and OW. (a) the time series of annual hypoxia volume (DO< 2 mg L^{-1}), (b-d) the June-July averaged oxygen concentration at lower bay, oxygen supply terms below 10 m depth and vertical gradient of DO at 10m depth.

Chapter 5: Conclusions

1. Summary of thesis contributions

Using a three-dimensional numerical model (ROMS) of Chesapeake Bay, we have investigated the dynamics of wind-driven lateral circulation in a stratified rotating estuary. The Ekman transport associated with the along-channel winds generates a counterclockwise lateral circulation under the down-estuary winds and a clockwise lateral circulation under the up-estuary winds (looking into estuary). However, the strength of the lateral circulation is about 2~3 times stronger during the up-estuary winds than during the down-estuary winds. Previous investigations of lateral circulations in estuaries have mainly focused on the analysis of the cross-channel momentum equation [e.g. *Lerczak and Geyer*, 2004; *Scully et al.*, 2009]. Here, in order to understand the asymmetric response, we adopt a new approach by analyzing the equation of the streamwise (along-channel) vorticity. Analysis of the streamwise vorticity equation reveals a balance among three terms: the conversion of the planetary vorticity by vertical shear in the along-channel current, baroclinic forcing due to sloping isopycnals at cross-channel sections, and turbulent diffusion. The first two terms can generate the streamwise vorticity whereas the turbulent diffusion acts to reduce it. In stratified estuary, the baroclinic forcing is highly asymmetric between the down- and up-estuary winds. The counterclockwise lateral circulation generated by the down-estuary winds tilts the isopycnals towards the vertical directions and creates adverse lateral barolinic pressure gradient to hamper the lateral Ekman

transport. In contrast, the clockwise lateral circulation generated by the up-estuary winds initially flattens the isopycnals and the baroclinic forcing reinforces the lateral Ekman transport.

The lateral flow has important implications to along-channel momentum balance. The traditional view of wind-driven circulation focused on the competition between the stress divergence and pressure gradient due to sea-level setup [e.g. *Wang, 1979a*; *Garvine*, 1985; *Janzen and Wong*, 2002]. When the lateral flows are driven, however, either the Coriolis acceleration or nonlinear advection can play important roles in the along-channel momentum balance. In the mainstem of Chesapeake Bay, the Coriolis acceleration associated with the lateral flows is of the first-order importance in the along-channel momentum balance. It has a sign opposite to the stress divergence in the surface layer and the pressure gradient in the bottom layer, thereby reducing the shear in the along-channel current. Compared with the non-rotating system but same geometry, the shear reduction is about 30-40%.

Further, the effects of lateral circulation on estuarine stratification are explored. In the absence of rotational effects, stratification in the estuary decreases following both down- and up-estuary winds, but stratification experiences larger reduction and takes longer to recover under up-estuary winds. In the presence of rotational effects, wind-driven lateral circulations cause the lateral straining of density field and weaken the shear in the along-channel flows. Under the down-estuary winds, even though the along-channel shear strains the along-channel salinity gradient to increase

stratification, a counterclockwise lateral circulation steepens isopycnals in the cross-channel sections. Under the up-estuary winds, while along-channel straining tends to decrease stratification, a clockwise lateral circulation initially flattens isopycnals in the cross-channel sections. Hence, in the presence of rotational effects, the lateral straining offsets the effects of longitudinal straining such that the asymmetry in stratification reduction is significantly reduced between the down- and up-estuary winds.

In an effort to generalize the model results specific to Chesapeake Bay, two nondimensional parameters are introduced to assess the overall effect of winds on along-channel, cross-channel shear and estuarine stratification: the Wedderburn number (W) which compares the wind forcing with the horizontal baroclinic pressure gradient and the Kelvin number (Ke) which is the ratio of the estuary width to the internal Rossby radius of deformation. Generally speaking, as $|W|$ increases, the along-channel and lateral shear are stronger and the stratification is weaker. Yet, there is asymmetry between down-estuary ($W<0$) and up-estuary ($W>0$) winds. Increasing Ke (e.g. higher latitude or wider estuaries) leads to weaker asymmetry for along-channel shear and stratification, but larger asymmetry for lateral shear.

The three-dimensional hydrodynamic model is coupled with an oxygen model to investigate the seasonal cycle of oxygen in Chesapeake Bay. Diagnostic analysis of the oxygen budget for the bottom water reveals a balance between three physical transport and two biological consumption terms. The traditional view only considers

the vertical diffusive flux; however, it is found that the along-channel and cross-channel advective fluxes are also important contributors in supplying oxygen to the bottom water. While the vertical diffusive oxygen flux varies over the spring-neap tidal cycle and is enhanced during wind events, the advective oxygen fluxes show long-term averages due to the gravitational estuarine circulation but display strong oscillations due to wind-driven circulations. The effectiveness of advective fluxes depends on wind directions. Winds from north weaken the along-channel oxygen supply but generate a clockwise lateral circulation to eject hypoxic water onto the shallow western shoal. In contrast, southward winds amplify the along-channel flux but reduce the cross-channel flux. For the biogeochemical consumptions, it is found that water column respiration contributes to about 74% of the total biological consumption and sediment oxygen demand contributes 26%.

Sensitivity-analysis model runs are conducted to further quantify the effects of river flow, winds, water column respiration and sediment oxygen demand on the hypoxic volume in the estuary. Increases in river discharge result in strong stratification and thus suppresses vertical diffusion and lateral advection of oxygen, but it enhances estuarine gravitational circulation and longitudinal oxygen transport. The two effects buffer each other and largely maintain a relatively stable total oxygen supply so that the summer hypoxic volume is relatively insensitive to large variations in river flow. For the wind forcing, the hypoxia is sensitive to the changes in wind-induced mixing and air-sea exchange, and both doubling or halving wind speed tends to generate less hypoxia in the Bay.

2. Implications for the future work

This dissertation identifies two important forces in driving lateral circulation. One is the conversion of planetary vorticity by along-channel shear, and baroclinic forcing due to sloping isopycnals at cross-channel sections. The analysis based on the streamwise vorticity could be extended to study lateral circulations in tidally forced estuaries. In the streamwise vorticity equation, the two-cell lateral circulation generated by differential advection can be described by the baroclinic forcing term $-g\beta\frac{\partial S}{\partial y}$ due to the lateral density gradient while the one-cell lateral circulation generated by the tidal rectification of lateral Ekman flow can be described by the conversion of the planetary vorticity by the shear in the tidal current $f\frac{\partial u}{\partial z}$. An outstanding question is how the two mechanisms contribute to the generation of the lateral circulations in estuaries of different widths and under different river discharge and tidal forcing conditions.

While the mechanism that drives lateral circulation is evident in the numerical model, there has been little observational documentation with adequate temporal and spatial resolution to resolve the full three-dimensional structure of flow and density fields. Given the importance of the lateral circulations on estuarine dynamics and seasonal hypoxia, especially for long estuary with wide channels, future observational study of the wind effects on lateral circulations is warranted. Cross-channel arrays of

moored current and temperature-conductivity-oxygen profilers and/or high resolution, cross-channel shipboard surveys are in need to resolve these mechanisms.

As for the oxygen dynamics, while our goal is to assess the key processes that regulate summer hypoxia in the Bay, as a first step, the major source (phytoplankton production) and sink (*WCR* and *SOD*) terms in the oxygen equation are parameterized from the regression analysis of observational data. In doing so, the biogeochemical cycle is apparently simplified. Processes such as phytoplankton bloom, nitrification-denitrification and sediment diagensis are neglected, but can influence the timing and magnitude of hypoxia. For example, once new nutrients are delivered to the estuary with the spring freshet, the transport and dispersion of these nutrients, their uptake in the spring bloom and recycling after remineralization, and the sinking and redistribution of organic matter are biogeochemical processes mediated by the physical processes in the Bay [*Boicourt*, 1992, *Li et al.*, 2009]. Therefore, a complete understanding of the oxygen dynamics requires further investigations using a water quality model that includes full biogeochemistry (i.e. Row Column Aesop Model, which includes compartments such as phytoplankton, N, P, Si, organic C and DO and a sediment diagenesis model to simulate biogeochemical cycling in the sediments).

3. Special notes

It should be noted that several clarifications have been made to Chapters 2 and 3 that are published prior to this dissertation defense. In Chapter 2, the $f\partial u/\partial z$ term in

the streamwise vorticity equation was originally named as “tilting of the planetary vorticity *f*” by *Li and Li* [2012]. However, by definition, *f* is contributed by the earth's rotation and always points normal to the earth surface. In order to avoid confusion, we reworded the name as “the conversion of the planetary vorticity *f*” in this dissertation. In Chapter 3, after cross-section average, the salt transport F_E due to shear-induced differential advection is expressed as a process creating longitudinal spreading, therefore we adopt the name “shear dispersion” which was previously used by *Lerczak and Geye*r [2004] for F_E.

References

Boicourt, W. C. (1992), Influences of circulation processes on dissolved oxygen in the Chesapeake Bay.

Garvine, R. W. (1985), A simple-model of estuarine subtidal fluctuations forced by local and remote wind stress, *J. Geophys. Res.*, *90*(C6), 1945-1948, doi: 10.1029/JC090iC06p11945.

Janzen, C. D., and K. C. Wong (2002), Wind-forced dynamics at the estuary-shelf interface of a large coastal plain estuary, *J Geophys Res-Oceans*, *107*(C10), -, doi: Artn 3138, Doi 10.1029/2001jc000959.

Lerczak, J. A., and W. R. Geyer (2004), Modeling the lateral circulation in straight, stratified estuaries, *J. Phys. Oceanogr.*, *34*(6), 1410-1428, doi: 10.1175/1520-0485(2004)034<1410:MTLCIS>2.0.CO;2.

Li, M., and L. J. Zhong (2009), Flood-ebb and spring-neap variations of mixing, stratification and circulation in Chesapeake Bay, *Cont. Shelf Res.*, *29*(1), 4-14, doi: 10.1016/j.csr.2007.06.012.

Li, Y., and M. Li (2012), Wind-driven lateral circulation in a stratified estuary and its effects on the along-channel flow, *J Geophys Res-Oceans.* doi:10.1029/2011JC007829

Scully, M. E., W. R. Geyer, and J. A. Lerczak (2009), The influence of lateral advection on the residual estuarine circulation: A numerical modeling study of the Hudson River Estuary, *J. Phys. Oceanogr.*, *39*(1), 107-124, doi: 10.1175/2008jpo3952.1.

Wang, D. P. (1979a), Subtidal sea-level variations in the Chesapeake Bay and relations to atmospheric forcing, *J. Phys. Oceanogr.*, *9*(2), 413-421, doi: 10.1175/1520-0485(1979)009<0413:SSLVIT>2.0.CO;2.

References

Andersson, L., and L. Rydberg (1988), Trends in nutrient and oxygen conditions within the Kattegat - Effects of local nutrient supply, *Estuarine Coastal Shelf Sci.*, *26*(5), 559-579, doi: 10.1016/0272-7714(88)90006-6.

Boicourt, W. C. (1992), Influences of circulation processes on dissolved oxygen in the Chesapeake Bay.

Borsuk, M. E., C. A. Stow, and K. H. Reckhow (2004), Confounding effect of flow on estuarine response to nitrogen loading, *J. Environ. Eng.*, *130*, 605, doi: 10.1061/(ASCE)0733-9372(2004)130:6(605).

Bowden, K. F. (1953), Note on wind drift in a channel in the presence of tidal currents, *Proc. R. Soc. London, A*, *219*(1139), 426-446, doi: 10.1098/rspa.1953.0158.

Boynton, W. R., and E. M. Bailey (2008), Sediment oxygen and nutrient exchange measurements from Chesapeake Bay: development of a comprehensive database and analysis of factors controlling patterns and magnitude of sediment-water exchanges. *TS-542-08*, University of Maryland Center for Environmental Science.

Boynton, W., W. Kemp, and C. Keefe (1982), A comparative analysis of nutrients and other factors influencing estuarine phytoplankton production, *Estuarine Comparisons. Academic Press, New York*, 69-90.

Burchard, H., R. D. Hetland, E. Schulz, and H. M. Schuttelaars (2011), Drivers of Residual Estuarine Circulation in Tidally Energetic Estuaries: Straight and Irrotational Channels with Parabolic Cross Section, *J. Phys. Oceanogr.*, *41*(3), 548-570， doi: 10.1175/2010JPO4453.1

Burchard, H., and H. M. Schuttelaars (2012), Analysis of tidal straining as driver for

estuarine circulation in well mixed estuaries, *J. Phys. Oceanogr.*, *42*, 261-271, doi: 10.1175/JPO-D-11-0110.1.

Cerco, C. (1995), Response of Chesapeake Bay to nutrient load reductions, *J. Environ. Eng.*, *121*, 549, doi: 10.1061/(ASCE)0733-9372(1995)121:8(549).

Cerco, C. F., and T. M. Cole (1994), Three-dimensional eutrophication model of Chesapeake Bay. Volume 1: Main report, DTIC Document.

Chan, F., J. Barth, J. Lubchenco, A. Kirincich, H. Weeks, W. Peterson, and B. Menge (2008), Emergence of anoxia in the California Current large marine ecosystem, *Science*, *319*(5865), 920-920, doi: 10.1126/science.1149016.

Chant, R. J. (2002), Secondary circulation in a region of flow curvature: Relationship with tidal forcing and river discharge, *J. Geophys. Res.*, *107*(3131), 207-223, doi: 10.1029/2001JC001082.

Chatwin, P. (1976), Some remarks on the maintenance of the salinity distribution in estuaries, *Estuarine Coastal Mar. Sci.*, *4*(5), 555-566, doi: 10.1016/0302-3524(76)90030-X.

Chen, S.-N., and L. P. Sanford (2009a), Axial wind effects on stratification and longitudinal salt transport in an idealized, partially mixed estuary, *J. Phys. Oceanogr.*, *39*(8), 1905-1920, doi: 10.1175/2009JPO4016.1.

Chen, S.-N., L. P. Sanford, and D. K. Ralston (2009b), Lateral circulation and sediment transport driven by axial winds in an idealized, partially mixed estuary, *J. Geophys. Res.*, *114*, C12006, doi: 10.1029/2008JC005014.

Cheng, P., R. E. Wilson, R. J. Chant, D. C. Fugate, and R. D. Flood (2009), Modeling influence of stratification on lateral circulation in a stratified estuary, *J. Phys. Oceanogr.*, *39*(9), 2324-2337, doi: 10.1175/2009JPO4157.1.

Chuang, W. S., and W. C. Boicourt (1989), Resonant seiche motion in the Chesapeake Bay, *J. Geophys. Res.*, *94*(C2), 2105-2110, doi: 10.1029/JC094iC02p02105.

Cloern, J. E., A. E. Alpine, B. E. Cole, R. L. J. Wong, J. F. Arthur, and M. D. Ball (1983), River discharge controls phytoplankton dynamics in the northern San Francisco Bay estuary, *Estuar. Coast. Shelf Sci*, *16*(4), 415-426, doi: 10.1016/0272-7714(83)90103-8.

Conley, D. J., J. Carstensen, R. Vaquer-Sunyer, and C. M. Duarte (2009), Ecosystem thresholds with hypoxia, *Hydrobiologia*, *629*(1), 21-29, doi: 10.1007/s10750-009-9764-2.

Conley, D. J., J. Carstensen, G. Aertebjerg, P. B. Christensen, T. Dalsgaard, J. L. S. Hansen, and A. B. Josefson (2007), Long-term changes and impacts of hypoxia in Danish coastal waters, *Ecol. Appl.*, *17*(5), S165-S184, doi: 10.1890/05-0766.1.

Cowan, J. L. W., and W. R. Boynton (1996), Sediment-water oxygen and nutrient exchanges along the longitudinal axis of Chesapeake Bay: Seasonal patterns, controlling factors and ecological significance, *Estuaries*, *19*(3), 562-580, doi: 10.2307/1352518.

Csanady, G. T. (1973), Wind-induced barotropic motions in long lakes, *J. Phys. Oceanogr.*, *3*(4), 429-438, doi: 10.1175/1520-0485(1973)003<0429:WIBMIL>2.0.CO;2.

de Boer, G. J., J. D. Pietrzak, and J. C. Winterwerp (2008), Using the potential energy anomaly equation to investigate tidal straining and advection of stratification in a region of freshwater influence, *Ocean Modell.*, *22*(1-2), 1-11, doi: 10.1016/j.ocemod.2007.12.003.

Diaz, R. J. (2001), Overview of hypoxia around the world, *J. Environ. Qual.*, *30*(2), 275-281, doi: 10.2134/jeq2001.302275x.

Diaz, R. J., and R. Rosenberg (1995), Marine benthic hypoxia: a review of its ecological effects and the behavioural responses of benthic macrofauna, *Oceanogr. Mar. Biol., Annu. Rev.*, *33*, 245-303.

Diaz, R. J., and R. Rosenberg (2008), Spreading dead zones and consequences for marine ecosystems, *Science*, *321*(5891), 926-929, doi: DOI: 10.1126/science.1156401.

Egbert, G. D., and S. Y. Erofeeva (2002), Efficient inverse modeling of barotropic ocean tides, *J. Atmos. Oceanic Technol.*, *19*(2), 183-204, doi: 10.1175/1520-0426(2002)019<0183:EIMOBO>2.0.CO;2

Egbert, G. D., A. F. Bennett, and M. G. G. Foreman (1994), TOPEX/POSEIDON tides estimated using a global inverse model, *J. Geophys. Res.*, *99*(C12), 24821-24824,24852, doi: 10.1029/94JC01894.

Fairall, C., E. Bradley, J. Hare, A. Grachev, and J. Edson (2003), Bulk parameterization of air-sea fluxes: Updates and verification for the COARE algorithm, *J. Climate*, *16*(4), 571-591, doi: 10.1175/1520-0442(2003)016<0571:BPOASF>2.0.CO;2.

Fisher, T., A. Gustafson, G. Radcliffe, K. Sundberg, and J. Stevenson (2003), A long-term record of photosynthetically available radiation (PAR) and total solar energy at 38.6N, 78.2W, *Estuaries Coasts*, *26*(6), 1450-1460, doi: 10.1007/BF02803653.

Friedrichs, C. T., and J. M. Hamrick (1996), Effects of channel geometry on cross sectional variations in along channel velocity in partially stratified estuaries, *Buoyancy Effects on Coastal and Estuarine Dynamics*, *53*, 283–300.

Garcia, H. E., and L. I. Gordon (1993), Oxygen solubility in seawater - Better fitting equations (Vol 37, Pg 1308, 1992), *Limnol. Oceanogr.*, *38*(3), 656-656, doi: 10.4319/lo.1992.37.6.1307.

Garvine, R. W. (1985), A simple-model of estuarine subtidal fluctuations forced by local and remote wind stress, *J. Geophys. Res.*, *90*(C6), 1945-1948, doi: 10.1029/JC090iC06p11945.

Garvine, R. W. (1995), A dynamical system for classifying buoyant coastal discharges, *Cont. Shelf Res.*, *15*(13), 1585-1596, doi: 10.1016/0278-4343(94)00065-U.

Geyer, W. R. (1997), Influence of wind on dynamics and flushing of shallow estuaries, *Estuarine Coastal Shelf Sci.*, *44*(6), 713-722, doi: doi:10.1006/ecss.1996.0140.

Geyer, W. R., J. H. Trowbridge, and M. M. Bowen (2000), The dynamics of a partially mixed estuary, *J. Phys. Oceanogr.*, *30*(8), 2035-2048, doi: 10.1175/1520-0485(2000)030<2035:TDOAPM>2.0.CO;2.

Geyer, W. R., J. D. Woodruff, and P. Traykovski (2001), Sediment transport and trapping in the Hudson River estuary, *Estuaries Coasts*, *24*(5), 670-679, doi: 10.2307/1352875.

Giddings, S. N., D. A. Fong, and S. G. Monismith (2011), Role of straining and advection in the intratidal evolution of stratification, vertical mixing, and longitudinal

dispersion of a shallow, macrotidal, salt wedge estuary, *J. Geophys. Res.*, *116*(C3), C03003, doi: 10.1029/2010JC006482.

Goodrich, D. M., W. C. Boicourt, P. Hamilton, and D. W. Pritchard (1987), Wind-induced destratification in Chesapeake Bay, *J. Phys. Oceanogr.*, *17*(12), 2232-2240, doi: 10.1175/1520-0485(1987)017<2232:WIDICB>2.0.CO;2.

Guo, X. Y., and A. Valle-Levinson (2008), Wind effects on the lateral structure of density-driven circulation in Chesapeake Bay, *Cont. Shelf Res.*, *28*(17), 2450-2471, doi: 10.1016/j.csr.2008.06.008.

Hagy, J. D., W. R. Boynton, C. W. Keefe, and K. V. Wood (2004), Hypoxia in Chesapeake Bay, 1950-2001: Long-term change in relation to nutrient loading and river flow, *Estuaries*, *27*(4), 634-658, doi: 10.1007/BF02907650.

Haidvogel, D. B., H. G. Arango, K. Hedstrom, A. Beckmann, P. Malanotte-Rizzoli, and A. F. Shchepetkin (2000), Model evaluation experiments in the North Atlantic Basin: simulations in nonlinear terrain-following coordinates, *Dynam. Atmos. Oceans*, *32*(3), 239-281, doi: 10.1016/S0377-0265(00)00049-X.

Hansen, D. V., and J. M. Rattray (1965), Gravitational circulation in straits and estuaries, *J. Mar. Res.*, *23*(2), 104-122.

Harding, L. W., B. W. Meeson, and T. R. Fisher (1986), Phytoplankton production in two east coast estuaries: photosynthesis-light functions and patterns of carbon assimilation in Chesapeake and Delaware Bays, *Estuar. Coast. Shelf Sci*, *23*(6), 773-806, doi: 10.1016/0272-7714(86)90074-0.

Hetland, R. D., and W. R. Geyer (2004), An idealized study of the structure of long, partially mixed estuaries, *J. Phys. Oceanogr.*, *34*(12), 2677-2691, doi: 10.1175/JPO2646.1.

Hetland, R. D., and S. F. DiMarco (2008), How does the character of oxygen demand control the structure of hypoxia on the Texas-Louisiana continental shelf?, *J. Marine Syst.*, *70*(1-2), 49-62, doi: 10.1016/j.jmarsys.2007.03.002.

Howarth, R. W., D. P. Swaney, T. J. Butler, and R. Marino (2000), Rapid communication: Climatic control on eutrophication of the Hudson River Estuary, *Ecosystems*, *3*(2), 210-215, doi: 10.1007/s100210000020.

Huijts, K., H. Schuttelaars, H. De Swart, and C. Friedrichs (2009), Analytical study of the transverse distribution of along-channel and transverse residual flows in tidal estuaries, *Cont. Shelf Res.*, *29*(1), 89-100, doi: 10.1016/j.csr.2007.09.007.

Janzen, C. D., and K. C. Wong (2002), Wind-forced dynamics at the estuary-shelf interface of a large coastal plain estuary, *J. Geophys. Res.*, *107*(C10), 3138, doi: 10.1029/2001jc000959.

Johannessen, T., and E. Dahl (1996), Declines in oxygen concentrations along the Norwegian Skagerrak coast, 1927-1993: A signal of ecosystem changes due to eutrophication?, *Limnol. Oceanogr.*, 766-778.

Justić, D., R. E. Turner, and N. N. Rabalais (2003), Climatic influences on riverine nitrate flux: Implications for coastal marine eutrophication and hypoxia, *Estuaries*, *26*(1), 1-11, doi: 10.1007/BF02691688.

Justić, D., N. N. Rabalais, and R. E. Turner (2002), Modeling the impacts of decadal changes in riverine nutrient fluxes on coastal eutrophication near the Mississippi River Delta, *Ecol. Model.*, *152*(1), 33-46, doi: 10.1016/S0304-3800(01)00472-0.

Keller, A. A., C. A. Oviatt, H. A. Walker, and J. D. Hawk (1999), Predicted impacts of elevated temperature on the magnitude of the winter-spring phytoplankton bloom

in temperate coastal waters: A mescosm study, *Limnol. Oceanogr.*, 344-356, doi: 10.4319/lo.1999.44.2.0344.

Kemp, W. M., P. A. Sampou, J. Garber, J. Tuttle, and W. R. Boynton (1992), Seasonal depletion of oxygen from bottom waters of Chesapeake Bay - Roles of benthic and planktonic respiration and physical exchange processes, *Mar. Ecol. Prog. Ser.*, *85*(1-2), 137-152.

Kemp, W. M., J. M. Testa, D. J. Conley, D. Gilbert, and J. D. Hagy (2009), Temporal responses of coastal hypoxia to nutrient loading and physical controls, *Biogeosciences*, *6*(12), 2985-3008, doi: 10.5194/bg-6-2985-2009.

Kemp, W. M., et al. (2005), Eutrophication of Chesapeake Bay: historical trends and ecological interactions, *Mar. Ecol. Prog. Ser.*, *303*, 1-29, doi: 10.3354/meps303001.

Kundu, P. K., and I. M. Cohen (2004), *Fluid mechanics, 3rd edition*, 759 pp., Elsevier Academic Press, San Diego, Calif.

Kuo, A. Y., and B. J. Neilson (1987), Hypoxia and salinity in Virginia Estuaries, *Estuaries*, *10*(4), 277-283, doi: 10.2307/1351884.

Lacy, J. R., M. T. Stacey, J. R. Burau, and S. G. Monismith (2003), Interaction of lateral baroclinic forcing and turbulence in an estuary, *J. Geophys. Res.*, *108*(C3), 3089, doi: 10.1029/2002JC001392.

Lee, Y. J., B. R. Walter, M. Li and Y. Li (submitted), The role of winter-spring wind and other factors controlling summer hypoxia in Chesapeake Bay, *Estuaries Coasts*.

Lehman, P. W. (1992), Environmental factors associated with long-term changes in chlorophyll concentration in the Sacramento-San Joaquin Delta and Suisun Bay, California, *Estuaries Coasts*, *15*(3), 335-348, doi: 10.2307/135278.

Lerczak, J. A., and W. R. Geyer (2004), Modeling the lateral circulation in straight, stratified estuaries, *J. Phys. Oceanogr.*, *34*(6), 1410-1428, doi: 10.1175/1520-0485(2004)034<1410:MTLCIS>2.0.CO;2.

Lerczak, J. A., W. R. Geyer, and R. J. Chant (2006), Mechanisms driving the time-dependent salt flux in a partially stratified estuary, *J. Phys. Oceanogr.*, *36*(12), 2296-2311, doi: 10.1175/JPO2959.1.

Lerczak, J. A., W. R. Geyer, and D. K. Ralston (2009), The temporal response of the length of a partially stratified estuary to changes in river flow and tidal amplitude, *J. Phys. Oceanogr.*, *39*(4), 915-933, doi: 10.1175/2008JPO3933.1.

Levitus, S. (1983), Climatological Atlas of the World Ocean, *Eos, Trans. Amer. Geophys. Union*, *64*(49), 962-963, doi: 10.1029/EO064i049p00962-02.

Li, M., and L. J. Zhong (2009), Flood-ebb and spring-neap variations of mixing, stratification and circulation in Chesapeake Bay, *Cont. Shelf Res.*, *29*(1), 4-14, doi: 10.1016/j.csr.2007.06.012.

Li, M., L. Sanford, and S. Y. Chao (2005), Effects of time dependence in unstratified tidal boundary layers: Results from large eddy simulations, *Estuarine Coastal Shelf Sci.*, *62*(1-2), 193-204, doi: 10.1016/j.ecss.2004.08.017.

Li, M., L. J. Zhong, and W. C. Boicourt (2005), Simulations of Chesapeake Bay estuary: Sensitivity to turbulence mixing parameterizations and comparison with observations, *J. Geophys. Res.*, *110*(C12), -, doi 10.1029/2004jc002585.

Li, M., L. Zhong, and L. W. Harding (2009), Sensitivity of plankton biomass and productivity to variations in physical forcing and biological parameters in Chesapeake Bay, *J. Mar. Res.*, *67*(5), 667-700, doi: 10.1357/002224009791218878.

Li, M., L. Zhong, W. C. Boicourt, S. L. Zhang, and D. L. Zhang (2007), Hurricane-induced destratification and restratification in a partially-mixed estuary, *J. Mar. Res.*, *65*(2), 169-192.

Li, Y., and M. Li (2011), Effects of winds on stratification and circulation in a partially mixed estuary, *J. Geophys. Res.*, *116*, C12012, doi: 10.1029/2010JC006893.

Li, Y., and M. Li (2012), Wind-driven lateral circulation in a stratified estuary and its effects on the along-channel flow, *J. Geophys. Res*. doi:10.1029/2011JC007829

MacCready, P. (1999), Estuarine adjustment to changes in river flow and tidal mixing, *J. Phys. Oceanogr.*, *29*(4), 708-726, doi: 10.1175/1520-0485(1999)029<0708:EATCIR>2.0.CO;2

MacCready, P. (2007), Estuarine adjustment, *J. Phys. Oceanogr.*, *37*(8), 2133-2145, doi: Doi 10.1175/Jpo3082.1.

MacCready, P., and W. R. Geyer (2010), Advances in estuarine physics, *Ann. Rev. Mar. Sci.*, *2*, 35-58, doi: 10.1146/annurev-marine-120308-081015.

Malone, T. C. (1991), River flow, phytoplankton production and oxygen depletion in Chesapeake Bay, *Geological Society, London, Special Publications*, *58*(1), 83-93, doi: 10.1144/GSL.SP.1991.058.01.06.

Malone, T. C., W. M. Kemp, H. W. Ducklow, W. R. Boynton, J. H. Tuttle, and R. B. Jonas (1986), Lateral variation in the production and fate of phytoplankton in a partially stratified estuary, *Mar. Ecol. Prog. Ser.*, *32*(2-3), 149-160, doi: 10.3354/meps032149.

Marchesiello, P., J. McWilliams, and A. Shchepetkin (2001), Open boundary conditions for long-term integration of regional oceanic models, *Ocean Modell.*, *3*(1), 20, doi: 10.1016/S1463-5003(00)00013-5.

Mesinger, F., G. DiMego, E. Kalnay, K. Mitchell, P. C. Shafran, W. Ebisuzaki, D. Jovic, J. Woollen, E. Rogers, and E. H. Berbery (2006), North American regional reanalysis, *Bull. Am. Meteorol. Soc.*, *87*(3), 343-360, doi: 10.1175/BAMS-87-3-343.

Miller, W. D., and L. Harding (2007), Climate forcing of the spring bloom in Chesapeake Bay, *Mar. Ecol. Prog. Ser.*, *331*, 11-22, doi: 10.3354/meps331011.

Miller, W. D., L. W. Harding, and J. E. Adolf (2006), Hurricane Isabel generated an unusual fall bloom in Chesapeake Bay, *Geophys. Res. Lett.*, *33*(6), doi: 10.1029/2005GL025658.

Monismith, S. (1986), An experimental-study of the upwelling response of stratified reservoirs to surface shear-stress, *J. Fluid Mech.*, *171*, 407-439, doi: 10.1017/S0022112086001507.

Murphy, R. R., W. M. Kemp, and W. P. Ball (2011), Long-term trends in Chesapeake Bay seasonal hypoxia, stratification, and nutrient loading, *Estuaries Coasts*, 1-17, doi: 10.1007/s12237-011-9413-7.

North, E. W., S. Y. Chao, L. P. Sanford, and R. R. Hood (2004), The influence of wind and river pulses on an estuarine turbidity maximum: Numerical studies and field observations in Chesapeake Bay, *Estuaries*, *27*(1), 132-146, doi: 10.1007/BF02803567.

Nunes, R., and J. Simpson (1985), Axial convergence in a well-mixed estuary, *Estuarine Coastal Shelf Sci.*, *20*(5), 637-649, doi: 10.1016/0272-7714(85)90112-X.

O'Donnell, J., H. G. Dam, W. F. Bohlen, W. Fitzgerald, P. S. Gay, A. E. Houk, D. C. Cohen, and M. M. Howard-Strobel (2008), Intermittent ventilation in the hypoxic zone of western Long Island Sound during the summer of 2004, *J. Geophys. Res.*, *113*, C09025, doi: 10.1029/2007JC004716.

Officer, C., R. Biggs, J. Taft, L. Cronin, M. Tyler, and W. Boynton (1984), Chesapeake Bay anoxia: origin, development, and significance, *Science*, *223*(4631), 22, doi: 10.1126/science.223.4631.22.

Parker, C. A., and J. E. O'Reilly (1991), Oxygen depletion in Long Island Sound: a historical perspective, *Estuaries Coasts*, *14*(3), 248-264, doi: 10.2307/1351660.

Peierls, B. L., R. R. Christian, and H. W. Paerl (2003), Water quality and phytoplankton as indicators of hurricane impacts on a large estuarine ecosystem, *Estuaries*, *26*(5), 1329-1343, doi: 10.1007/BF02803635.

Pritchard, D. W. (1954), A study of the salt balance in a coastal plain estuary, *J. Mar. Res.*, *13*(1), 133-144.

Ralston, D. K., W. R. Geyer, and J. A. Lerczak (2008), Subtidal salinity and velocity in the Hudson River estuary: Observations and modeling, *J. Phys. Oceanogr.*, *38*(4), 753-770, doi: 10.1175/2007JPO3808.1.

Rattray, M., and D. V. Hansen (1962), A similarity solution for circulation in an estuary, *J. Mar. Res.*, *20*(2), 121-133.

Reyes-Hernández, C., and A. Valle-Levinson (2010), Wind modifications to density-driven flows in semienclosed, rotating basins, *J. Phys. Oceanogr.*, *40*, 1473-1487, doi: 10.1175/2010JPO4230.1

Reynolds-Fleming, J. V., and R. A. Luettich (2004), Wind-driven lateral variability in a partially mixed estuary, *Estuarine Coastal Shelf Sci.*, *60*(3), 395-407, doi: 10.1016/j.ecss.2004.02.003.

Rosenberg, R. (1990), Negative oxygen trends in Swedish coastal bottom waters, *Marine Pollution Bulletin*, *21*(7), 335-339, doi: 10.1016/0025-326X(90)90794-9.

Sampou, P., and W. M. Kemp (1994), Factors regulating plankton community respiration in Chesapeake Bay, *Mar. Ecol. Prog. Ser.*, *110*(2-3), 249-258.

Sanford, L. P., and W. C. Boicourt (1990), Wind-forced salt intrusion into a tributary estuary, *J. Geophys. Res.*, *95*(C8), 13357-13371, doi: 10.1029/JC095iC08p13357.

Sanford, L. P., K. G. Sellner, and D. L. Breitburg (1990), Covariability of dissolved-oxygen with physical processes in the summertime Chesapeake Bay, *J. Mar. Res.*, *48*(3), 567-590.

Scully, M. E. (2010a), The importance of climate variability to wind-driven modulation of hypoxia in Chesapeake Bay, *J. Phys. Oceanogr.*, *40*(6), 1435-1440, doi: 10.1175/2010JPO4321.1.

Scully, M. E. (2010b), Wind modulation of dissolved oxygen in Chesapeake Bay, *Estuaries Coasts*, *33*(5), 1164-1175, doi: 10.1007/s12237-010-9319-9.

Scully, M. E., C. Friedrichs, and J. Brubaker (2005), Control of estuarine stratification and mixing by wind-induced straining of the estuarine density field, *Estuaries*, *28*(3), 321-326, doi: 10.1007/BF02693915.

Scully, M. E., W. R. Geyer, and J. A. Lerczak (2009), The influence of lateral advection on the residual estuarine circulation: A numerical modeling study of the

Hudson River Estuary, *J. Phys. Oceanogr.*, *39*(1), 107-124, doi: 10.1175/2008jpo3952.1.

Shchepetkin, A. F., and J. C. McWilliams (2005), The regional oceanic modeling system (ROMS): a split-explicit, free-surface, topography-following-coordinate oceanic model, *Ocean Modell.*, *9*(4), 347-404, doi: 10.1016/j.ocemod.2004.08.002.

Shen, J., T. Wang, J. Herman, P. Mason, and G. L. Arnold (2008), Hypoxia in a coastal embayment of the Chesapeake Bay: A model diagnostic study of oxygen dynamics, *Estuaries Coasts*, *31*(4), 652-663, doi: 10.1007/s12237-008-9066-3.

Simpson, J. H., J. Brown, J. Matthews, and G. Allen (1990), Tidal straining, density currents, and stirring in the control of estuarine stratification, *Estuaries*, *13*(2), 125-132, doi: 10.2307/1351581.

Smith, E., and W. Kemp (1995), Seasonal and regional variations in plankton community production and respiration for Chesapeake Bay, *Mar. Ecol. Prog. Ser.*, *116*(1), 217-231.

Taft, J. L., W. R. Taylor, E. O. Hartwig, and R. Loftus (1980), Seasonal oxygen depletion in Chesapeake Bay, *Estuaries Coasts*, *3*(4), 242-247, doi: 10.2307/1352079.

Townsend, D. W., and L. M. Cammen (1988), Potential importance of the timing of spring plankton blooms to benthic-pelagic coupling and recruitment of juvenile demersal fishes, *Biol. Oceanogr*, *5*(3), 215-228.

Turner, R. (1978), Community plankton respiration in a salt marsh estuary and the importance of macrophytic leachates, *Limnol. Oceanogr.*, *23*(3), 442-451.

Tyler, R. M., D. C. Brady, and T. E. Targett (2009), Temporal and spatial dynamics of diel-cycling hypoxia in estuarine tributaries, *Estuaries Coasts*, *32*(1), 123-145, doi: 10.1007/s12237-008-9108-x.

Valle-Levinson, A. (2008), Density-driven exchange flow in terms of the Kelvin and Ekman numbers, *J. Geophys. Res.*, *113*(C4), C04001, doi: 10.1029/2007jc004144.

Verity, P. G., M. Alber, and S. B. Bricker (2006), Development of hypoxia in well-mixed subtropical estuaries in the southeastern USA, *Estuaries Coasts*, *29*(4), 665-673, doi: 10.1007/BF02784291.

Wang, D. P. (1979a), Subtidal sea-level variations in the Chesapeake Bay and relations to atmospheric forcing, *J. Phys. Oceanogr.*, *9*(2), 413-421, doi: 10.1175/1520-0485(1979)009<0413:SSLVIT>2.0.CO;2.

Wang, D. P. (1979b), Wind-driven circulation in the Chesapeake Bay, winter 1975, *J. Phys. Oceanogr.*, *9*(3), 564-572, doi: 10.1175/1520-0485(1979)009<0564:WDCITC>2.0.CO;2.

Wang, D. P., and A. J. Elliott (1978), Non-tidal variability in Chesapeake Bay and Potomac River - evidence for nonlocal forcing, *J. Phys. Oceanogr.*, *8*(2), 225-232, doi: 10.1175/1520-0485(1978)008<0225:NTVITC>2.0.CO;2.

Wanninkhof, R. (1992), Relationship between Wind-Speed and Gas-Exchange over the Ocean, *J. Geophys. Res.*, *97*(C5), 7373-7382, doi: 10.1029/92JC00188.

Warner, J. C., W. R. Geyer, and J. A. Lerczak (2005), Numerical modeling of an estuary: A comprehensive skill assessment, *J. Geophys. Res.*, *110*, C05001, doi: 10.1029/2004JC002691.

Wei, H., Y. C. He, Q. J. Li, Z. Y. Liu, and H. T. Wang (2007), Summer hypoxia adjacent to the Changjiang Estuary, *J. Marine Syst.*, *67*(3-4), 292-303, doi: 10.1016/j.jmarsys.2006.04.014.

Weisberg, R. H., and W. Sturges (1976), Velocity Observations in West Passage of Narragansett Bay - Partially Mixed Estuary, *J. Phys. Oceanogr.*, *6*(3), 345-354, doi: 10.1175/1520-0485(1976)006<0345:VOITWP>2.0.CO;2.

Welsh, B. L., and F. C. Eller (1991), Mechanisms controlling summertime oxygen depletion in western Long Island Sound, *Estuaries Coasts*, *14*(3), 265-278, doi: 10.2307/1351661.

Wilson, R. E., R. L. Swanson, and H. A. Crowley (2008), Perspectives on long-term variations in hypoxic conditions in western Long Island Sound, *J. Geophys. Res.*, *113*, C12011, doi: 10.1029/2007JC004693.

Winant, C. (2004), Three-dimensional wind-driven flow in an elongated, rotating basin, *J. Phys. Oceanogr.*, *34*(2), 462-476, doi: 10.1175/1520-0485(2004)034<0462:TWFIAE>2.0.CO;2.

Wong, K. C. (1994), On the nature of transverse variability in a coastal-plain estuary, *J. Geophys. Res.*, *99*(C7), 14209-14222, doi: 10.1029/94JC00861.

Wong, K. C., and J. E. Moses-Hall (1998), On the relative importance of the remote and local wind effects to the subtidal variability in a coastal plain estuary, *J. Geophys. Res.*, *103*(C9), 18393-18404, doi: 10.1029/98JC01476.

Wong, K. C., and A. Valle-Levinson (2002), On the relative importance of the remote and local wind effects on the subtidal exchange at the entrance to the Chesapeake Bay, *J. Mar. Res.*, *60*(3), 477-498.

Xu, J. T., S. Y. Chao, R. R. Hood, H. V. Wang, and W. C. Boicourt (2002), Assimilating high-resolution salinity data into a model of a partially mixed estuary, *J. Geophys. Res.*, *107*(C7), -, doi: 10.1029/2000jc000626.

Zhong, L., and M. Li (2006), Tidal energy fluxes and dissipation in the Chesapeake Bay, *Cont. Shelf Res.*, *26*(6), 752-770, doi: 10.1016/j.csr.2006.02.006.

Zhong, L., M. Li, and M. G. G. Foreman (2008), Resonance and sea level variability in Chesapeake Bay, *Cont. Shelf Res.*, *28*(18), 2565-2573, doi: 10.1016/j.csr.2008.07.007.